The Dynamics of Plasma Surface Interaction

Proefschrift

ter verkrijging van
de graad van Doctor aan de Universiteit Leiden,
op gezag van de Rector Magnificus Dr. P.F. van der Heijden,
hoogleraar in de faculteit der Wiskunde en
Natuurwetenschappen en die der Geneeskunde,
volgens besluit van het College voor Promoties
te verdedigen op woensdag 28 Februari 2007
klokke 16.15 uur

door

F. Gou

geboren te Sichuan, China
in 1969

Promotiecommissie

Promotoren:	Prof. Dr. A. W. Kleyn
Co-promotor	Dr. M. Gleeson
Referent:	Prof. Dr. W. Goedheer
Overige leden:	Prof. Dr. Prof. M.T.M. Koper Prof. Dr. Prof. M. van Hemert Prof. Dr. Prof. J. Brouwer Dr. Roar A. Olsen

CONTENTS

2 A new time-of-flight instrument capable of in-situ and real time studies of plasma-treated surfaces

3 3keV Ar$^+$ scattering from unreconstructed Si(100) at grazing incidence: molecular dynamics simulation

4 MD simulation of Ar scattering from defected Si (100) at grazing incidence

5 Theoretical modeling of energy redistribution and stereodynamics in CF scattering from Si(100) under grazing incidence

6 CF interaction with Si (100)-(2x1): Molecular Dynamics Simulation

7 Molecular dynamics simulation of CH_3 interaction with Si (100) surface

8 General discussion

Chapter 1

Introduction

Over the past decades, plasma etching has been widely used in the fabrication of silicon-based integrated circuits. However, due to complex physical and chemical effects during etching, issues of reproducibility and control of the interaction processes ultimately limit its widespread application and further progress. In plasma etching, reactive neutral and ionic species strike the surfaces that are in contact with plasma and form products as illustrated in figure 1. An electron-free space-charge region designated as a "sheath" forms between a plasma and a contacting solid surface. Sheaths are of critical importance for plasma etching, since positive ions are accelerated toward the surface when entering a sheath. The accelerated ions bombard the surface with energies that are much greater than thermal energies. This results in non-thermal interactions that are in many instances dominant in controlling the outcome of a plasma-surface process. The consequences of plasma-surface interactions are to a significant extent controlled by the incident ion fluxes and their energies. A number of theoretical studies have indicated that nearly all incident ions will be neutralized within a few angstroms of the surface, as a result of Auger or resonant processes. Thus, the majority of the particles actually striking surface atoms are not positive ions, but neutral species.

In order to fully understand etching processes, a fundamental knowledge of plasma-surface interactions is needed. Establishing and quantitatively describing a plasma-induced surface reaction mechanism in the plasma environment requires, (a) characterization of the incident species fluxes, e.g., as a function of composition, energy, angle, and so forth; (b) determination of the surface processes, e.g., adsorption, reflection, direct reaction behavior of the incident species, the surface coverage, composition of the reaction layer, and so forth; (c) determination of the reaction products ejected from the surface (their chemical identity, energy content, desorption mechanism, angular distribution etc.). Ideally we would like to characterize and quantify the importance of each of the elementary surface processes for important plasma and surface species, and relate these to measured etching or deposition rates, film properties, etc.

For analysis of the incident flux and the ejected reaction products, many techniques are applicable for in-situ analysis. Laser-induced fluorescence, line-of-sight plasma sampling by mass spectrometry, Fourier transform infrared (IR) spectroscopy or IR diode laser absorption spectroscopy and UV absorption spectroscopy. Using these techniques, the incident flux can be relatively precisely characterized. Many powerful surface science tools are used to for post-exposure characterization of surfaces, such as X-ray photoelectron spectroscopy (XPS), Auger electron spectroscopy (AES) and scanning electron microscopy (SEM). However, the measurements of these tools are performed under ultra-high vacuum (UHV).conditions Therefore, the treated sample must be transferred to a UHV chamber and an assumption of stability of the plasma-modified surface must be made.

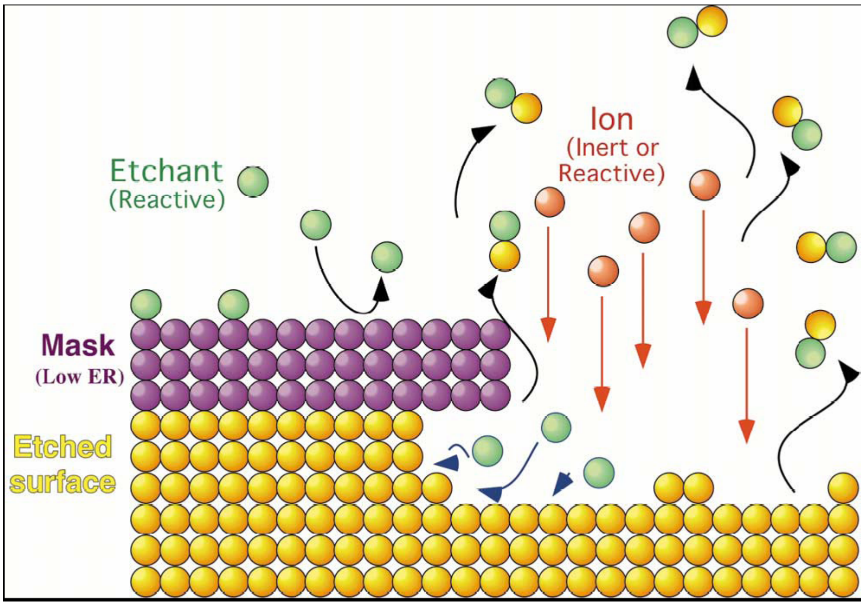

Figure 1: Schematic picture of plasma-surface interaction

In order to overcome deficiencies of conventional surface analytical tools, in our laboratory a new low energy, grazing-incidence ion scattering apparatus was introduced to investigate plasma surface interactions. This technique can monitor real-time and in-situ surface reactions occurring during plasma processing. It has the following advantages: (1) monolayer or subsurface sensitivity by adjusting the primary ion and angles involved. (2) element-specific and sensitive to all elements, including hydrogen, in the outermost layers. (3) surface structure analysis. In addition, in order to avoid strong coupling between plasma and surface, a cascaded arc source introduces plasma to the UHV chamber through three differentially pumped stages. Combining these two sources in one chamber, plasma strikes the surface at normal incidence. At the same time, a low ion energy beam scatters from the surface at grazing incidence to monitor reactions occurring.

Typically experimental results from plasma/ion surface interaction are complex because of the wide range of processes occurring. Identifying the relative importance of individual events from the measured ensemble can be very important. In order to better interpret the experimental data and to get insight into the interactions of low energy ions with surfaces, we adopted molecular dynamics (MD) simulations to model the processes. In terms of the functions of the new setup, our simulations are divided into two parts. One part is the simulation of grazing scattering of projectiles (Ar and CF) from the surface. The other part deals with plasma surface interactions. This thesis details the functions of the experiment apparatus and the results from the complementary MD simulations.

MD is an atomic simulation method for studying equilibrium and transport properties of classical many-body systems. The basic idea in an MD simulation is simply to set up the system and to solve Newton's equations of motion for the collection of mutually interacting particles. Newton's equations are used to derive the dynamics of the system; we obtain the following set of 6*N* equations:

$$\begin{cases} \dot{r}_i = p_i / m_i \\ \dot{p}_i = F_i \end{cases}$$

where $\mathbf{p}_i$ is the momentum of the particle, r_i and m_i are the position and mass of the particle i, F_i is the total force exerting on it derived from the interatomic potential. These two equations can be solved by finite difference methods using a time interval d*t* which must be made sufficiently small for accurate results. In MD simulations, the dynamics of the system are obtained by following trajectories of the individual atoms. The course of a trajectory is dictated by the interatomic potential. This means that we are able to address time-dependent properties of the system, such as ion scattering from a surface, ion implantation, sputtering of surface atoms and thin film growth.

It is important to note that the purpose of an MD simulation is not to predict precisely what will happen to a system that is initially in a well-defined state. In fact, for almost all systems, the trajectory of the system through phase space is sensitively dependent on the initial conditions. This means that the trajectories of two systems which were initially very close to one another may diverge exponentially as time progresses. Therefore, the aim of the simulation is to predict the average behavior of the system in a statistical sense.

By using MD simulations, much work has been performed on particle interaction with surfaces (at normal and grazing incidence), cluster beam deposition, annealing processes and structure of thin films and the mechanical properties of multilayer films. In this thesis, we examine grazing scattering geometry relevant to the new setup. In addition, deposition and etching modeling, related to plasma-surface interactions, are done using MD methods. Therefore, this thesis can be clearly divided into two main parts, based on the incidence geometry.

(1) Grazing scattering

In this part, we simulated projectiles (Ar, CF) scattering from un-reconstructed Si and defected Si (100) surfaces at grazing incidence. The incidence energy is more than 1 keV. The normal incidence energy is related to the total energy, according to the equation: $E_n = E_T * \sin(\theta)^2$, where E_n is the normal incident energy, E_T is the total energy and θ is the incidence angle with respect to the surface plane. At grazing incidence, the normal incidence energy is only several eV while the parallel energy is much larger than the normal incidence. This means that the incidence particles cannot penetrate the surface into the bulk. Therefore, scattering under this geometry is very sensitive to the surface structure and is suitable as a surface probe. Given the small normal incidence energy, in this section a Molière potential is used to describe the interaction between projectiles and Si atoms. A spring potential is used for Si-Si interactions. For the C-F interaction, the Morse potential is adopted.

(2) Interaction with surface at normal incidence (deposition and etching)

In the second part, plasma-surface interactions are simulated. As mentioned before, ion interactions play an important role in plasma-surface interaction. When reactive ions from plasmas interact with surface atoms many chemical reactions (bond breaking and formation) occur. In order to relatively precisely describe this behavior under classic MD, reactive empirical bond order (REBO) potential is adopted. This type of potential allows for covalent bond breaking and formation with associated changes in atomic hybridization within a classical potential, producing a powerful method for modeling complex chemistry in large many-body systems. The incidence energy ranges from 2-200 eV, comparable to ion energies in plasma processes.

This thesis

This thesis consists of several chapters representing the particle-surface modeling that was done by MD simulations. Each chapter can be read separately and since they are interrelated some overlap of content is inevitable. Together they describe physical and chemical processes that may occur in our new instrumentation.

Chapter 2 describes the new time-of-flight (TOF) instrument for studying the dynamics of plasma-surface interactions. Some experimental results for Ar^+ scattering from Si (100) surfaces subject to different pre-treatments are shown.

In **chapters 3-5**, modeling of grazing scattering in the new setup is shown. In **chapter 3**, grazing scattering of 3 keV Ar along the [100] direction of an ideal (unreconstructed) Si (100) surface is simulated. A detailed analysis of the scattering trajectories is performed. The dependence of the energy loss, scattering angle on the surface structure is shown. In **chapter 4**, the MD simulations of Ar scattering from perfect and point-defected Si(100) surfaces at grazing incidence are shown. The simulated results demonstrate that the angular and energy distributions of the scattered particles are extremely sensitive to small adatom coverages. An electron-stopping model is included in the simulations to model the available experimental data in which the energy loss is mainly contributed by inelastic loss processes. The results produce simulated energy losses that are in good agreement with experimental measurements. In **chapter 5**, we have simulated CF scattering from Si (100) using the molecular dynamics method. Translational energy loss spectra are presented and the stereodynamics of CF scattering is discussed.

Chapters 6-8 show modeling of plasma-surface interactions. In **chapter 6**, the interaction of CF with the clean Si(100)-(2x1) surface at normal incidence and room temperature was investigated using molecular dynamics simulation. Some simulated results are in good agreement with available experimental data. The level of agreement between the simulated and experimental results and the limitation of MD simulation are discussed. In **chapter 7**, molecular dynamics simulations of the CH_3 interaction with Si (100) were performed using the Brenner potential. The results show that H atoms preferentially react with Si. SiH is the dominant form of SiHx generated. The amount of hydrogen that reacts with silicon is essentially energy-independent. H atoms do not react with adsorbed carbon atoms. The presence of C-H bonds on the surface is attributed to molecular adsorption. In **chapter 8,** a general discussion is presented to show how the potential, some important parameters (heat bath, relaxation time and cell size) and the surface temperature affect etching of Si by fluorocarbon. **Chapter 8** can be regarded as a primer on some of the technical consideration involved in MD simulations.

Chapter 2

A new time-of-flight instrument capable of in-situ and real time studies of plasma-treated surfaces

Abstract: We introduce a new time-of-flight (TOF) instrument that has been constructed to study the dynamics of plasma-surface interactions. The instrument uses a well-defined ion beam at a grazing incidence as a surface probe. Real-space and real-time profiles of scattered particles are created from the output of a position-sensitive detector. The set-up permits the recording of energy and angular distributions of scattered ions and neutrals. Changes in energy and angular distribution as a function of time can be used to monitor real-time and in-situ the interaction between plasma and surfaces. The performance of the set-up is tested and illustrative spectra for Ar^+ scattering from Si (100) surfaces subject to different pre-treatments are shown.

2.1 Introduction

Plasma etching, plasma-enhanced chemical vapor deposition and plasma/wall interactions generally involve a variety of physical and chemical processes at surfaces [1-3]. The complex and highly coupled nature of plasma-surface interactions makes the study of dynamics difficult in a plasma environment and as a consequence the mechanisms of the processes are unclear. Grazing-incidence ion scattering has been used to determine surface structure and, in particular, the geometry of first layer adsorbate atoms [4]. It may prove a good technique for monitoring plasma-surface processing in real-time. To our knowledge, there are no groups employing such a combination in a single apparatus. Motivated by this demand, we have built an experimental set-up designed to investigate plasma-surface interactions in-situ and in real time. It utilizes Time-Of-Flight Low Energy Ion Scattering (TOF/LEIS) and Direct Recoil Spectroscopy (DRS) to characterize adsorbed species and to monitor the electronic structure and topography of the sample surface [5]. These techniques are emerging as viable surface analysis tools with particular strength for in-situ monitoring during low-pressure thin film processing [6]. TOF/LEIS can be very useful for determining electronic structure and surface composition through charge-exchange analysis, and long-range crystalline order through scattering profile analysis. Detection of recoiled atoms provides a means of monitoring low concentration of adsorbed species on the surface.

2.2 The In-Situ Spectrometer System

The new system is constructed from a combination of custom-made and commercially available components. It is shown schematically in figure 1 and consists of several distinct elements: (a) main chamber; (b) preparation chamber; (c) pulsed ion beam source; (d) cascaded arc plasma source; (e) the position-sensitive detector (PSD) for scattered particles.

(a) Main Chamber: In the main chamber, where the base pressure is in the 10^{-10} mbar range with the plasma off [7], the sample is mounted on a three-axis manipulator in the centre of the chamber [8]. The position of the sample is controlled by computer. The sample manipulator can be rotated through 360° around the vertical axis of the chamber (polar rotation). In addition, 360° spin rotation of the sample around the surface normal axis can be obtained (azimuthal rotation). X- and Y- translations of the sample holder with respect to the centre of the chamber have a travel of ±15mm with an accuracy of 0.1 mm. The manipulator has a Z-translation of 200 mm. The sample can be tilted 90° backward (sample facing up) and 20° forward (sample facing down).

The bulk of the tools available in the main chamber are on a single horizontal measurement plane. This plane contains the plasma and ion sources, the multi-channel plate (MCP) based detection system, the exchange point for the preparation chamber, a sputter gun, and a quadrupole mass spectrometer (QMS). The QMS is supplied by ABB-Extrel (type MEX060 2.9C3/P8: ¾ inch (19.05 mm) rods, 2.9 MHz 300W Q-head, off-axial cross-beam ionizer in pulse counting mode). It is mounted on the lid of the vacuum system with the ion extraction region centered in the measurement plane. The lid has a differentially-pumped system that allows it to be rotated while maintaining UHV. Consequently, the ion extraction region of the QMS can be rotated around the measurement plane. The QMS can be used to characterize the plasma source (species and energy distribution) directly and to detect plasma particles scattered from the surface.

(b) Preparation Chamber*:* In the preparation chamber (base pressure 5×10^{-11} mbar), samples can be cleaned by ion sputtering and/or annealing to more than 1000K. The cleanliness of the surface can be characterized by X-ray photoelectron spectroscopy (XPS). The surface order can be monitored by low energy electron diffraction (LEED). This chamber can hold multiple samples at one time. The samples can be transferred by a linear translator, under vacuum, to the three-axis manipulator in the main chamber.

(c) Ion Source: An ion source, oriented at a low incident angle with respect to the plasma- facing surface, is used for LEIS and DRS studies [9]. The ion beam is produced in a Colutron ion source with a low energy spread (<0.2 eV) [10]. Ions can be created with energies up to 4keV. A Wien filter (Colutron model 600-B) allows the removal of undesired ions from the beam. A 10° bend in the ion beamline eliminates neutrals and light originating from the source. The selected ions are focused using a series of einzel lenses and accelerated or decelerated to achieve the required energy.

TOF measurement can be performed by pulsing the ion beam with a high-resolution electrostatic chopper. This chopper consists of two plates pulsed symmetrically by a low voltage pulse generator, producing pulse widths down to ~25ns. In this way, the beam is rapidly swept in front of the injection aperture at the end of the beam line. The pulse generator can be operated a pre-determined frequency (10kHz-10MHz), or through an external trigger source. Thus, the START time (t0) is well defined and an associated trigger time is sent to the acquisition chain.

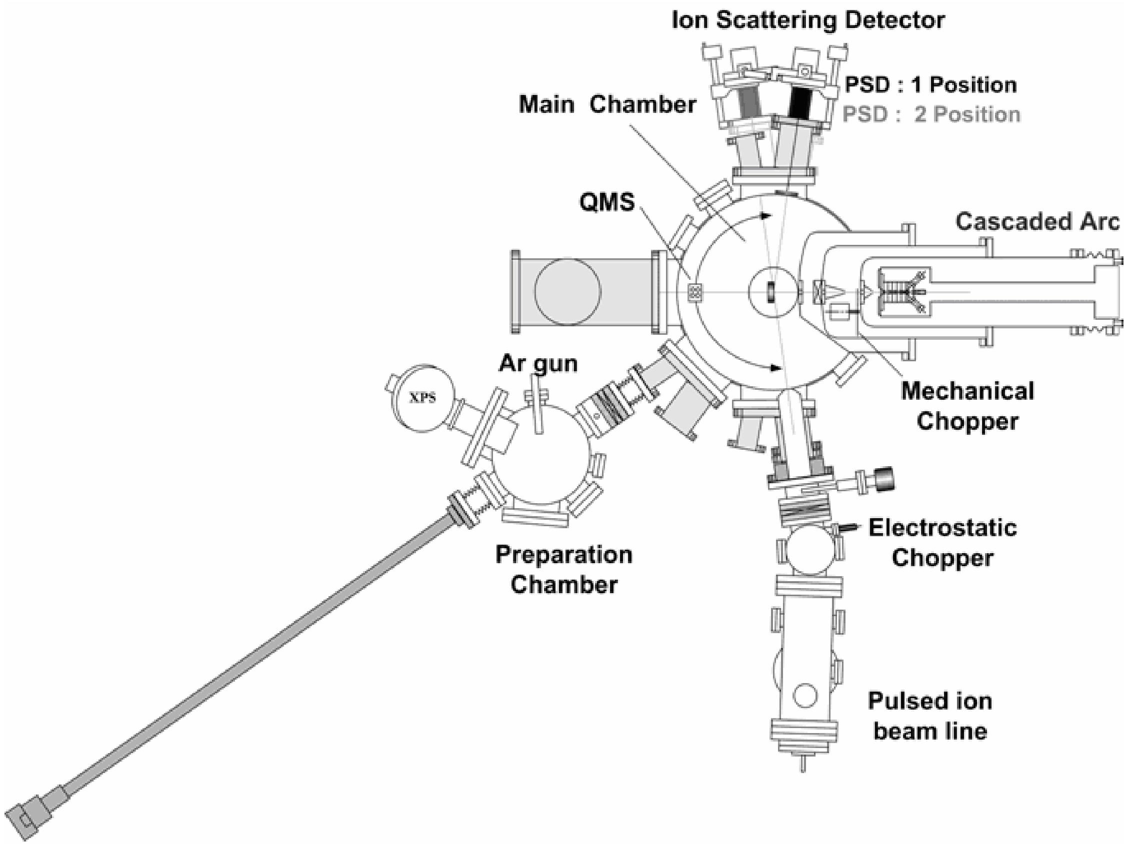

Figure 1: Layout of the set-up, see the text for details.

(d) Plasma Source: As shown in figure 1, the plasma beam is created in a differentially pumped beam line. The plasma source is a cascaded arc [11]. A current is drawn from three cathodes to the anode nozzle through a channel with diameter of typically few mm and a length of several cm. The channel consists of a stack of isolated water-cooled copper plates. The plasma beam can be modulated by means of a mechanical chopper. The ion beam pulse can be synchronized to this chopping frequency. Hence, if the presence of the plasma is cumbersome for the ion scattering, the scattering can be performed when the plasma is not exposed to the surface. Additionally, TOF studies of the energy distribution of the arc output and scattering plasma particles can be performed using the rotatable QMS.

(e) Position-sensitive Detector: In the previous sections, we outlined the main vacuum system in detail. In this apparatus the central measurements are based on position-sensitive detection of ions and neutrals. The detector is capable of real-time and in-situ two-dimensional imaging.

The configuration of the ion scattering/detection system can be seen in figure 1. On the lower side, the incident beam is injected at grazing incidence through a small aperture. On the opposite side, the scattered projectiles are collected by a position sensitive detector (PSD). The center of the PSD is positioned in the measurement plane. The detector is mounted on an XYZ translator, allowing for fine-tuning of its position. The whole system is built on a CF250 flange. The detector can be mounted in one of two fixed geometries, corresponding to

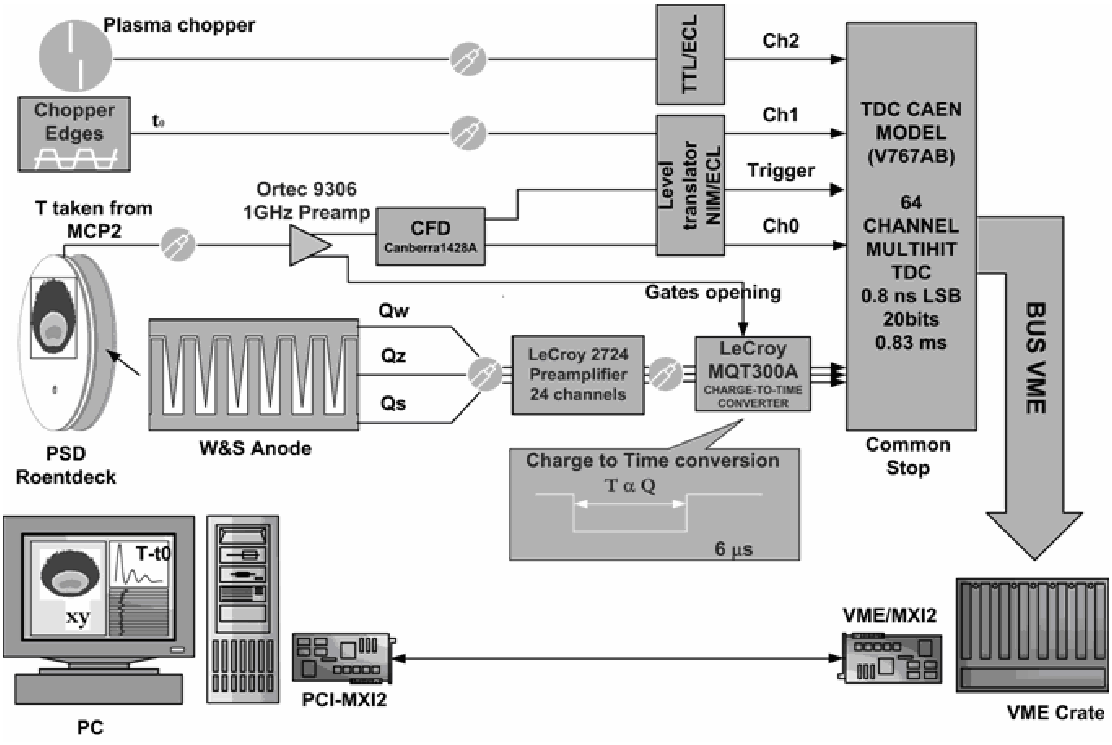

Figure 2: Schematic representation of the data acquisition system. The outputs of the two choppers are converted to ECL. The three charge outputs of the detector are amplified by a charge preamplifier and sent to a charge-to-time converter (QTC). The STOP time signal (T) is extracted from the second micro-channel-plate (MCP), amplified by a preamplifier, and sent to a fast discriminator. This signal is converted to ECL and used to trigger the multi-hit time-to-digital converter (TDC). This also provides the COMMON STOP (channel 0) for the acquisition. T is also used to trigger the integrating gate for the QTC. All of the MQT300A outputs are sent to TDC to be

maximum scattering angles of 8° and 16°. Deflecting plates with a 2 mm wide slit can be moved in front of the detector to allow determination of the charge fraction of scattered and recoiled particles.

Several types of position sensitive detector are available that use different methods of position determination. We utilize a wedge-and-strip based detection system supplied by Roentdek [12]. The computer-based data acquisition system was developed in this laboratory and is schematically outlined in figure 2.

To get sufficient amplification, a stack of two MCPs is employed. They have an active diameter of 40 mm and a thickness of 1 mm. They are mounted in front of a ceramic disk with a germanium layer on the side facing the MCP and with wedge, strip and meander anodes on the opposite side. The input of the first MCP is biased at a voltage of –1500 V. A grid biased at a small positive potential is placed in front of the PSD. Its main function is to repel low energy positive particles originating from the plasma source when the plasma is injected into the main chamber. The impact of a single particle on the front MCP results in a charge pulse at the output of the back MCP. This is collected by the germanium layer, which is biased at a small positive potential with respect to the back of the MCP stack. This charge pulse induces a current in the electrically isolated anodes on the opposite side of the ceramic disk.

Three charge signals are collected from the wedge (Qw), strip (Qs), and the meander (Qm) anode contacts, amplified and sent to a wide range, high precision charge-to-time converter (LeCroy MQT300A). The position of a particle arriving at the first MCP is determined by comparing the relative amounts of charge collected from wedge, strip and meander. The impact time signal (STOP time, T) is derived from the charge pulse on the second MCP via a built-in UHV compatible isolation transformer and is then amplified by a charge sensitive amplifier (ORTEC 9306 1 GHz Preamplifier).

The STOP time signal and the three charge signals are sent through a 16-twisted pair flat cable to a multi-channel time-to-digital converter (TDC 767 by CAEN) located in a Versa Module Europa (VME) crate. The TDC records the arrival time of the 64 channels with a 0.8 ns resolution during a set time window. The digitized signals (Q_w, Q_m, Qs, t_0 and T) are transferred to a first-in-first-out (FIFO) buffer memory in the TDC board, allowing a maximum accumulation of 32 Kwords. The data in the buffer memory can be read out to a host computer via VME (as single data, block transfer and chained block transfer) in a completely independent way from the acquisition itself.

The position of the detected particles is encoded by the three charge signals and can be easily transformed from the digitized signals into Cartesian coordinates (x, y) by the following algorithm:

$$x = Q_s/(Q_s+Q_w+Q_m), \qquad y = Q_w/(Q_s+Q_w+Q_m)$$

2.3 Experimental Results

A number of measurements involving interactions of low energy ions with surfaces were performed to test the new system. Here we present data obtained for scattering of Ar^+ at grazing incidence from Si (100) surfaces to illustrate the performance that can be obtained.

2.3.1 Ar^+ Scattering at Grazing Incidence

The sample is placed such that it partially intersects the ion beam. The spot at the bottom of the image arises from the part of the direct beam that misses the sample. The spread image is caused by the scattered particles. In the profile, the horizontal direction represents the azimuthal distribution of scattered particles. The vertical direction represents the polar distribution of scattered particles. Consequently, impacts on the MCP appearing directly above the direct-beam spot represent atoms scattered in-plane (no azimuthal scattering). Impacts to the left and right of this vertical line are due to atoms which are scattered out-of-plane (i.e. experience both polar and azimuthal deflection). Since the MCP plates are circular, the PSD represents the base of a scattering cone. All particles that are scattered within this cone will be detected by the PSD provided the impact initiates an electron cascade. The combination of the MCP active radius and the sample detector separation give a cone half-angle of ~3° (i.e. the PSD can detect a 6° spread of scattered particles, excluding edge effects).

During a typical scattering experiment, the acquisition system stores the time and magnitude of several key parameters. The main quantifies acquired are the chopper trigger (START time), the charge pulse on the second MCP (STOP time) and the magnitude of the three charges collected on the wedge-and-strip anode. By correlating the data, a flight-time can be assigned to each individual impact registered on the wedge-and-strip anode. Hence, TOF distributions of the scattered particles can be derived from the xy distributions. For example, post-acquisition analysis allows a TOF distribution to be constructed for particles impacting on strips associated with the different polar scattering angles shown in figure 3. The resulting TOF spectra are converted to energy loss spectra as shown in figure 4.

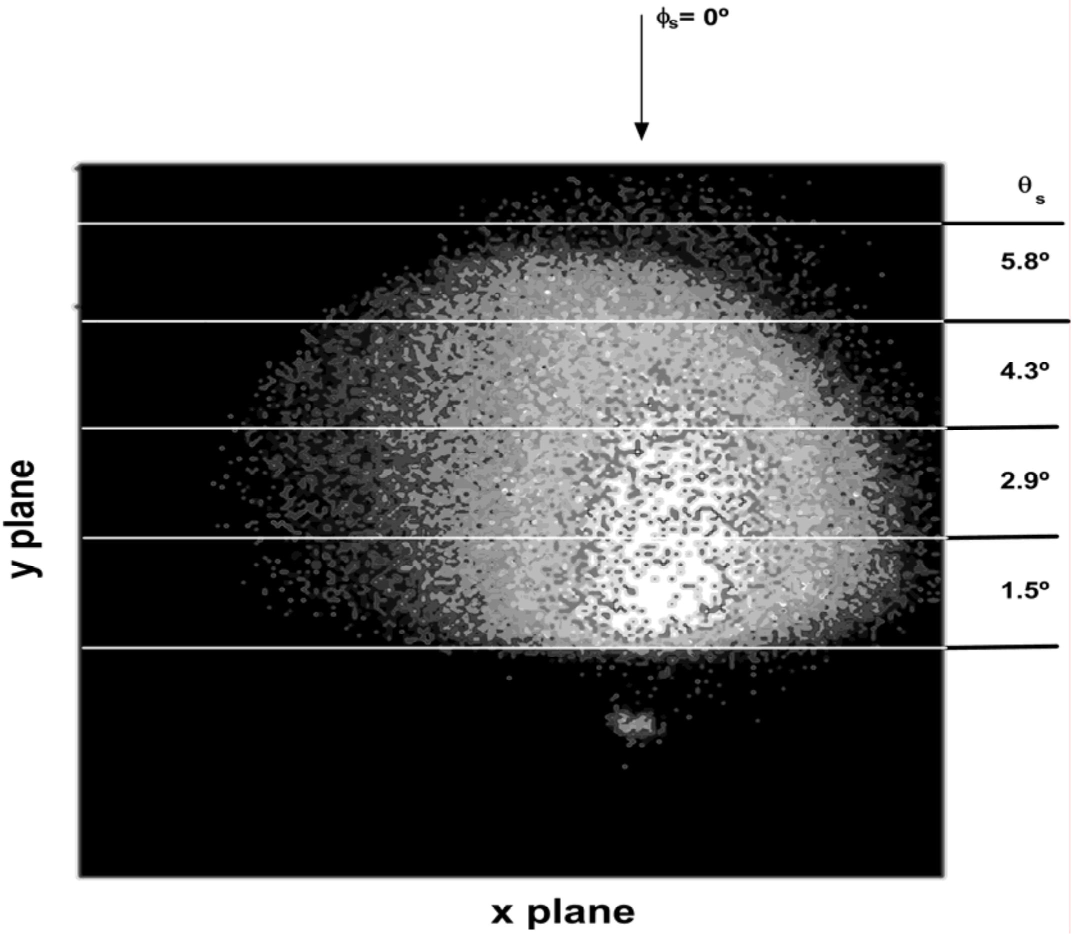

Figure 3: Example of the measured xy distribution for 2 keV Ar+ scattering from Si (100) at an incidence angle of 1.75° with respect to the surface plane. The lighter regions represent higher intensity. The distribution in x plane corresponds to the azimuthal distribution. The distribution in y plane corresponds to the polar distribution. The polar angles given are only accurate for $\phi_S = 0^{\circ}$. The angles indicated on the figure refer to the midpoint in the y-plane of the corresponding strip.

Unsurprisingly, particles scattered through the largest angles have undergone the largest energy loss. In addition, the width of the energy loss distribution and the length of the low energy tail increases for larger scattering angles.

The energy loss as a function of the scattering angle is plotted in figure 5. The anticipated loss based on a single binary collision model is also shown in the figure. The data points for the energy loss are based on the peak values of the energy loss distributions shown in figure 4. The energy loss observed is far greater than can be accounted for on the basis of simple elastic collision losses. The discrepancy can be attributed to additional inelastic energy loss processes and defects in the surface during the close interaction of the projectile with the surface atoms. Careful measurement of the energy loss distributions combined with theoretical modeling should provide a means of tracking electronic structure changes during plasma processing of surfaces.

2.3.2 Ar^+ Scattering and Recoiling From contaminated Si (100)

A TOF spectrum obtained from a partially cleaned Si (100) surface is shown in figure 6.From the figure, similar flight times are observed for Ar and recoiled particles, indicating that all final velocities are very similar. Scattered Ar and recoiled Si peaks are observed. The

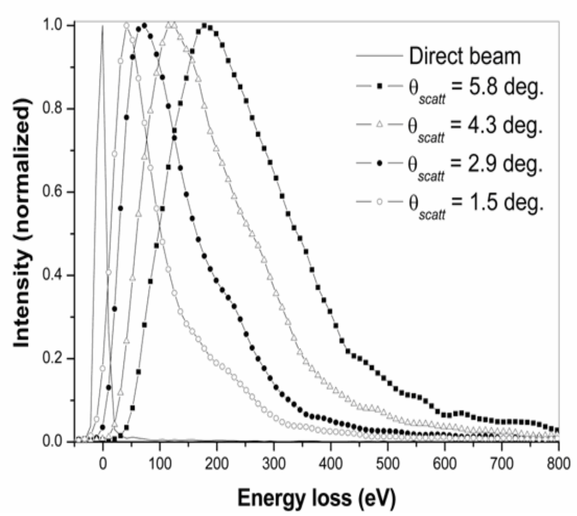

Figure 4: Energy loss spectra extracted from figure 3 for 2 keV Ar^+ scattering from Si(100) surface at an incidence angle of 0.75° with respect to the surface plane.

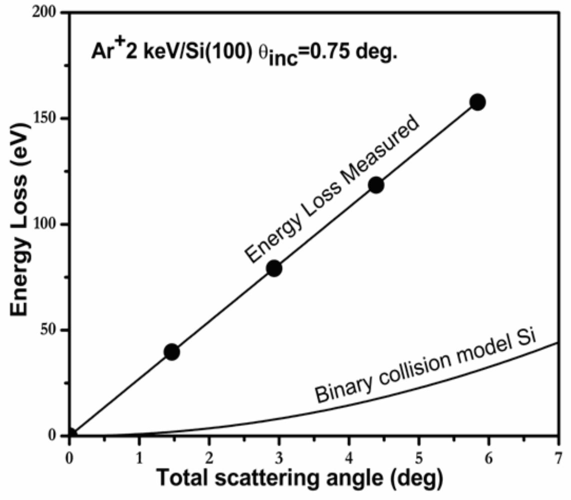

Figure 5: Energy loss spectra based on the peak values of the energy loss distributions shown in figure 4.

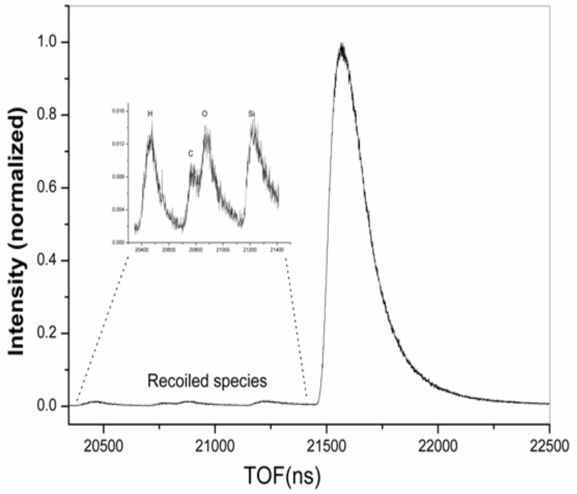

Figure 6: TOF spectra obtained by scattering 3 keV Ar^+ from a contaminated Si (100) surface at an incidence angle of 8° with respect to surface plane. (Inset: details of the contaminants).

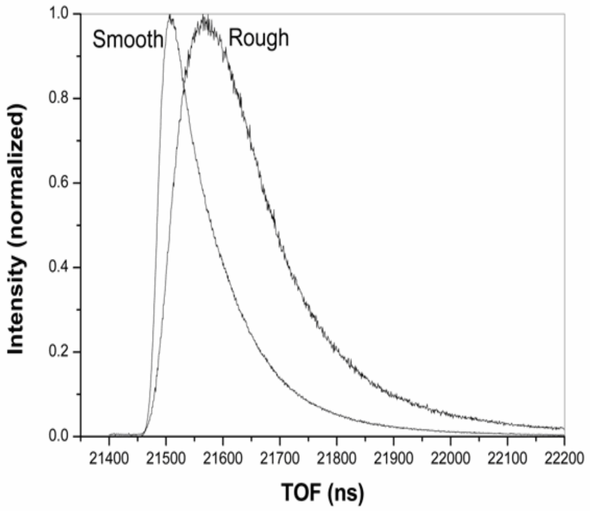

Figure 7: TOF spectra obtained by scattering 3 keV Ar^+ from an annealed (smooth) and a sputtered (rough) Si (100) surface at an incidence angle of 8° with respect to surface plane.

emergence of recoiling peaks from carbon, oxygen and hydrogen are due to contamination of the surface. At grazing angles, the incident projectile spends a relatively long time close to the surface. Consequently, ion scattering is very sensitive to contaminants on the surface. The ability to detect hydrogen atoms illustrates that the new system may provide a means to characterize the concentration and adsorption sites of hydrogen atoms on surfaces. Hydrogen deposited by a Ar/H plasma from the cascaded arc could be detected in this way.

2.3.3 Ar$^+$ Scattering from rough Si (100) surface

The width of the distribution on the PSD and the energy loss profile can be used to monitor the surface smoothness. For example, the width of the TOF distribution shown in figure 7 increases after sputtering by 600eV Ar+ at normal incidence angle. The smooth curve is the total TOF curve (based on T taken from the second MCP) for Ar scattered from a recently annealed Si (100) surface. After sputtering, the observed TOF distribution is significantly broader. In addition, both the leading edge and the peak maximum have shifted corresponding to an increase in the energy lost during the collision.

The above results indicate that the new system should be capable of monitoring structural changes on surface during plasma processing. For example, monitoring the rate of change of the disorder parameter and the degree of reconstruction on the surface.

2.4 Conclusion

A new TOF instrument based on the low energy ion scattering has been designed and constructed. The system allows grazing scattering of atomic or molecular ions from surfaces and the monitoring, real-time and in-situ, of the reaction dynamics of plasma with surface. The preliminary experiments show that this instrument allows surface composition analysis, studies of electronic interaction between projectiles and surface atoms and surface topography.

References

[1] J. W. Coburn, J Vac Sci Technol A 12 (1994) 1417.
[2] K. Yanai, K. Karahashi, K. Ishikawa, M. Nakamura, J Appl Phys 97 (2005) 053302.
[3] C. F. Abrams, D. B. Graves, J Vac Sci Technol A 19 (2001) 175.
[4] H. Winter, Phys Rep 367 (2002) 387.
[5] A. Kutana, T. Ito, I. L. Bolotin, B. Makarenko, J. W. Rabalais, Vacuum 73 (2004) 73.
[6] Y. Lin, A. R. Krauss, R. P. H. Chang, O. H. Auciello, D. M. Gruen, J. A. Schultz, Thin Solid Films 253 (1994) 247.
[7] M. E. M. Spruit, E. W. Kuipers, M. G. Tenner, J. Kimman, A. W. Kleyn, J Vac Sci Technol A 5 (1987) 496.
[8] A. Raukema, A. P. deJongh, H. P. Alberda, R. Boddenberg, F. G. Giskes, E. deHaas, A. W. Kleyn, H. Neerings, R. Schaafsma, H. Veerman, Meas Sci Technol 8 (1997) 253.
[9] W. R. Koppers, M. A. Gleeson, J. Lourenco, T. L. Weeding, J. Los, A. W. Kleyn, J Chem Phys 110 (1999) 2588.
[10] http://www.colutron.com, Colutron Research Corporation.
[11] M. C. M. v. d. Sanden, G. M. Janssen, J. M. d. Regt, D. C. Schram, J. A. M. v. d. Mullen, B. v. d. Sijde, Rev Sci Instrum 63 (1992) 3369.
[12] http://www.roentdek.de, RoentDek Handels GmbH.

Chapter 3

3 keV Ar scattering from unreconstructed Si (100) at grazing incidence: Molecular dynamics simulation

Abstract: In this paper, grazing scattering of 3 keV Ar along the [100] direction of an ideal (unreconstructed) Si (100) surface is simulated using the molecular dynamics (MD) method. A detailed analysis of the scattering trajectories is performed. The scattering process in many cases involves a sequence of simultaneous collisions between projectile and target atoms. The scattered intensity is presented as a function of the polar scattering angle, the azimuthal scattering angle and the energy loss. Various prominent features of the spectra are assigned to specific scattering trajectories.

3.1 Introduction

The interaction of low energy ions with surfaces has long been a topic of both theoretical and experimental interest [1-3]. Neutralization, charge exchange and energy loss between ions and metals surfaces are already well described [4-6]. In contrast, relatively few studies have been done on the interaction with semiconductor surfaces under grazing incidence [7]. A thorough investigation of particle interaction dynamics at semiconductor surfaces will be timely and important because such interactions play an important role in etching, film growth and surface analysis. With decreasing device sizes the dynamics at the surface become increasingly relevant to semiconductor manufacturing and plasma processing [8]. To date, some groups have investigated the scattering of simple ions (Ne^+, Ar^+ etc.) [9-11] from silicon surfaces. There are also some groups working on the interaction of plasma (such as CF_x, SiF_x, CH_x (x=1-4)) [12,13] with silicon. To our knowledge, no group has combined these two fields together to investigate the dynamics of plasma processing and how plasma-modified surfaces influence scattering.

In the last decades, grazing-incidence scattering has been intensively investigated and has been used successfully to monitor the growth of ultrathin films [14,15]. Winter's recent review [16] of the interaction of atoms and ions with surfaces under grazing incidence provides a detailed discussion of the field and extensive references to the literature. Grazing incidence scattering may prove a good technique for real-time and in-situ monitoring of plasma processing of surfaces. Although the topic is quite old, many aspects of it are still being unraveled [17-19]. Scattering at grazing incidence involves a projectile-surface interaction over a relatively long range (up to tens of nanometers), resulting in unique scattering phenomena such as surface channeling. In the group of Rabalais the hyper-channeling phenomenon at grazing incidence was investigated in detail, where straight trajectories or zigzag walks are confined in the potential valley of a single surface channel [19]. Winter and Schűller have recently characterized grazing incidence scattering in terms of rainbow scattering [17], which is usually studied for conditions of less grazing incidence [20]. Winter and Schűller have also pointed out that good interaction potentials are hard to obtain. They used the continuum model, introduced by Lindhard [21,22], for the interaction along the trajectory. Since the interaction time is greatly extended at the grazing geometry with respect to more normal incidence, the final state (charge, excitation, momentum) of the incident atom will be highly sensitive to the electronic and structural properties of the surface.

In our group, we have embarked upon a program of research involving the study of plasma modification of surfaces utilizing ion scattering under grazing incidence as a probe. To this end, we have designed and constructed an instrument to allow in-situ monitoring of surfaces under ultra high vacuum [23]. The instrument allows low energy ions (0.5-3 keV) to be incident at grazing angles (0-10° from the surface plane) on surfaces that can be simultaneously exposed to plasma particles produced in a differentially pumped cascaded arc system [24]. In order to support the experimental effort, we seek to develop a good method of modeling the scattering process. Analysis of the trajectories of scattered particles under grazing incidence is crucial for a detailed understanding of ion-surface interactions and to ensure that experimental measurement can be properly correlated to surface properties. Although there has been a substantial effort to model the dynamics of scattering, to our knowledge no groups have studied Ar scattering from Si (100) either by experiments or computer simulation at grazing incidence. The present paper will discuss 3 keV Ar scattering from Si (100) at 2° of incidence relative to the surface plane by molecular dynamics (MD). We present a detailed analysis of the process involved in elastic scattering at grazing incidence. Electronic effects and initial lattice vibrations are excluded in order to allow the elastic collision process to be clearly observed. The paper is intended to highlight the way in which the physical surface structure affects the scattering process.

3.2 Description of the simulation

There are several basic models used to simulate the interaction between ions and surfaces using classical mechanics. The continuum model is used to handle the surface channeling effect [21, 22]. The model of sequential, independent binary collision (BC) is used, for example in the MARLOWE code [25]. However, it has often been argued that the BC model is not suitable under channeling conditions and at low energy (below 100 eV) [20,25-28]. In order to make a computer code suitable for simulating the interaction of low energy atoms and molecules with surfaces (energies less than 10 eV), we have adopted the molecular dynamics (MD) method to simulate the process, although this method requires longer computation time than the BC and continuum models. MD method has already been used to simulate the grazing scattering from metal surfaces [29,30].

Details of the MD method used can be found elsewhere [31], but we describe the procedure briefly here. Molecular dynamics simulations calculate the time dependent positions and velocities of a system of atoms by numerically integrating Newton's equation of motion. The net force exerting on each atom is calculated from the gradient of an inter-atomic potential energy function. The Molière potential [32] is used for the Ar interaction with Si.

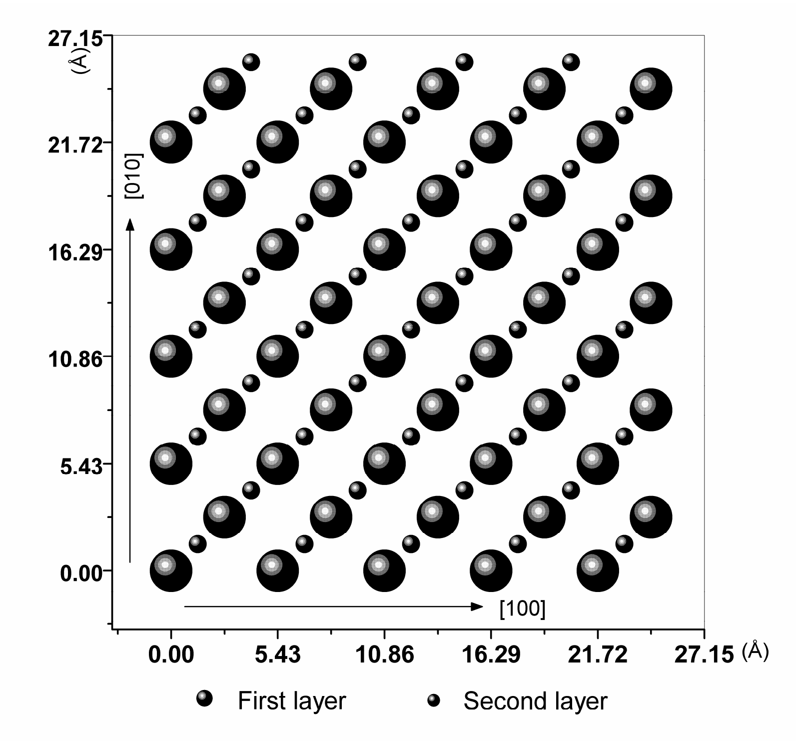

Figure 1: The top view of an unreconstructed Si(100) single crystal lattice, showing the relative positions of atoms in the first two layers.

We selected as a screening length of $0.8\alpha_F$, popularly used by other simulations [33,34]. The effect of using different potentials (e.g. ZBL, Born-Mayer or the adjusted Molière potential [36]) on the grazing scattering will be described in a later paper.

The target consists of a “box” containing three layers of atoms. Increasing either the number of layers or the number of atoms in each layer does not affect the calculated trajectories. In terms of the boundary conditions, the side of the box facing the incident atoms serves as the Si (100) surface. For the other sides, the atoms are fixed to their equilibrium positions. All other atoms inside the box and at the interacting surface are movable under force. A representation of the top view atomic structure of the simulated crystal is shown in figure 1.

The structure used is that of the ideal Si (100) surface. Calculations using the reconstructed Si (100) (2x1) surface will be shown elsewhere. For the present discussion, which is focused on the features of the dynamics, this is not a serious omission. Here, we define the x-direction along the [100] direction, the y-direction along the [010] direction, and the z-direction along the surface normal. Incident atoms approach the surface along the [100] direction (i.e. along the x-direction).

In our model, we tested two potentials for the crystal atoms interaction. One is the Tersoff potential that describes the silicon crystal well [37]. The other is the harmonic or spring potential [35]. Calculations showed that the difference between the two potentials was negligible at grazing incidence for the ideal surface. Hence, in order to speed up the calculation, we use the spring potential to describe the interactions between the crystal atoms and each crystal atom interacts only with its nearest neighbors. More details about this potential can be found in reference [38].

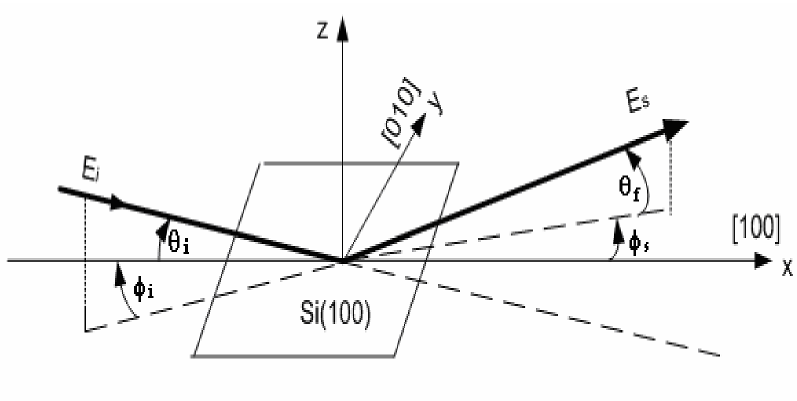

Figure 2: Illustration of the scattering geometry showing the definition of the scattering angles used in this paper.

In order to better expose the dynamics, all simulations are performed for a surface initially at rest (0 K). In this model, at the beginning, the crystal atoms are set to their equilibrium positions. The zero-point motion of the lattice atoms is neglected. However, the impact by the incident atoms still can result in recoiling of the crystal atoms due to energy transfer.

The incident Ar atoms are initially placed at 5 Å above the surface, where the potential is less than 10^{-5} eV with a random (*x*, *y*) position relative to one unit cell. We use the velocity Verlet scheme with a variable time step to numerically integrate Newton's equations of motion [39]. For each time-step in the trajectory, pair potentials are summed for atoms within a defined radius of the incident atom. Both the radius and the integration time-step are chosen to achieve an accuracy of better than 0.1% deviation from total energy.

The scattering geometry is shown in figure 2. The incoming (θ_i) and outgoing (θ_f) angles are defined with respect to the surface plane. The polar (in-plane) scattering angle (θ) is defined as the sum of θ_i and θ_f. The azimuthal (out-of-plane) scattering angle (ϕ) is measured with respect to the scattering plane, which is defined by the incident atom direction and the surface normal.

3.3 Results and Discussion

3.3.1 Trajectory analysis

In order to determine the relative importance of the various kinds of trajectories, five sample trajectories are initially calculated. In all cases, 3 keV Ar is incident at θ_i=2.0° along the [100] direction of the Si (100) surface. The starting point for each trajectory is defined with respect to a reference unit cell of the Si surface. The starting x value ([100] direction) of the five trajectories is zero. Their starting y points are evenly spaced across one half of the reference unit cell (length=1.3575 Å) along the [010] direction. The y values of the selected trajectories are given by

$$y_n = 5.43+n*0.339375$$

where n is the number of the trajectory (0-4). The approximate corresponding values are 5.43 Å, 5.77 Å, 6.11 Å, 6.45 Å and 6.79 Å.

The side- and top- views of the selected five trajectories (A-E) are shown in figure 3(a) and (b). Note the large difference in scale between the X- and Z- and the X- and Y- directions in

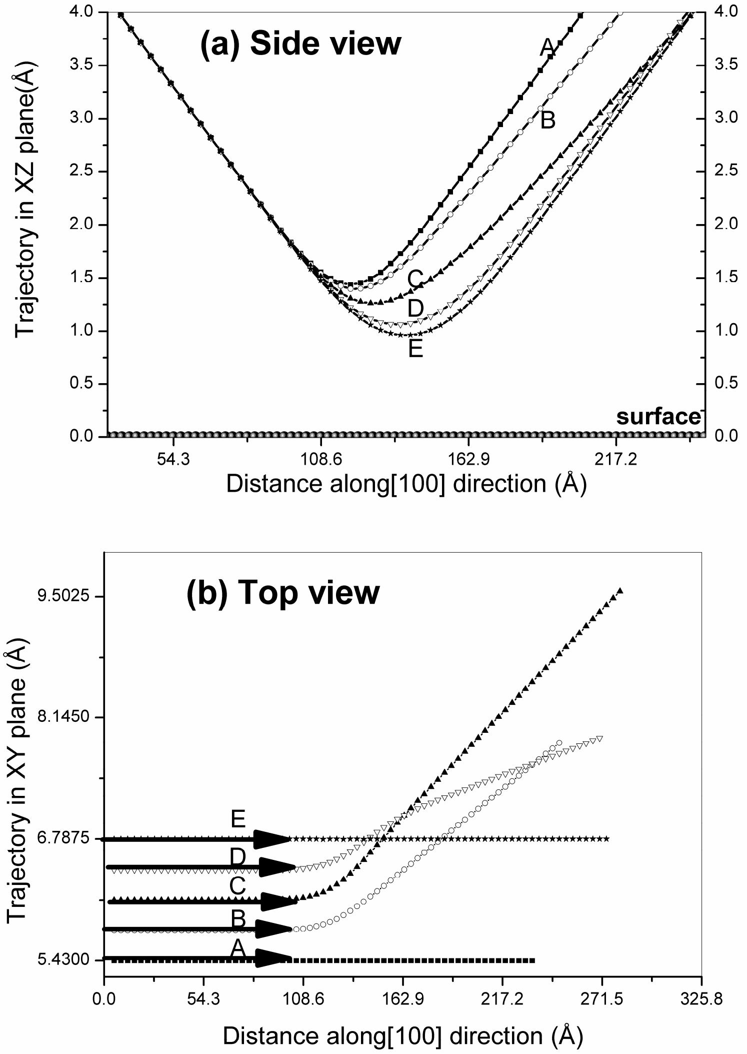

Figure 3: MD simulations of 3 keV Ar trajectories, with incidence angle of 2°, scattering from the unreconstructed Si (100) surface, (a) trajectories plotted in the XZ plane. (b) Trajectories plotted in the XY plane. The initial trajectories are illustrated on figure (b) and are selected as described in the text.

the respective plots. We define the turning point as being the point where the normal velocity is zero, corresponding to the distance of closest approach to the surface measured with respect to the first layer atoms. Considering the trajectories in figure 3 (a) (the side view), it is found that all turning points occur above the surface. No penetration below the surface layer occurs and surface channeling occurs for all trajectories (planar, axial or hyper channeling [19]). The outgoing directions of the scattered atoms correspond to polar scattering angles ranging from 3.6° to 4°. For trajectory A (y=5.43 Å) the incident atom is precisely over an atomic row of the first layer. From the side view it is clear that this trajectory has the highest turning point above the surface. As we move from trajectory B to E, we note that the projectile approaches progressively closer to the surface plane. For trajectory E (y~6.79 Å), which is precisely over the atomic row of the second layer, the turning point is the closest to the surface. Trajectories A and E have the largest polar scattering angle of the five trajectories, while trajectory C has the smallest.

In the top view (shown in figure 3 (b)) the azimuthal scattering of the trajectories is represented. We can see that trajectory A is always in-plane and no deflection is observed -

defined as string scattering in [19]. For trajectory B, which is initially just off an atomic row of the first layer as it approaches the surface, the projectile feels a repulsion from the atoms of the nearest first layer row and is deflected out-of-plane. For trajectory C, the behavior of the projectile is similar to that of trajectory B. For trajectory D (y~ 6.45 Å) the y component of its starting point is between the first and second layer rows. At first, the projectile is deflected out of plane due to repulsion by atoms in the first layer. Then it passes over the second layer rows and is reflected back in the direction of the scattering plane by the atoms in the adjacent top layer row. This is a zigzag collision. The final projectile direction still represents out-of-plane scattering, but this trajectory illustrates the beginning of a channeling effect caused by two adjacent atomic rows. Under these conditions the projectile starts to be confined to a single surface channel. Trajectory E undergoes in-plane scattering similar to trajectory A.

For the selected 5 trajectories, the evolution of their polar and azimuthal scattering angles along the [100] direction (x-axis) is shown in figure 4(a) and (b) respectively. These figures present a more detailed view of the trajectories shown in figure 3. It is seen that at grazing incidence, the scattering is caused by a series of discrete small angle collisions. Trajectories A and E exhibit specular scattering. For trajectories B, C and D sub-specular scattering occurs.

For trajectory A, we can note from figure 4(a) that the polar scattering angle does not change in a continuous fashion. Instead, the polar angle jumps periodically, each jump reflecting an individual collision with a first-layer atom, and then remains constant until the next collision. This indicates that during scattering the projectile only interacts with the first-layer atoms on an individual basis. The magnitude of each jump varies due to the change of the polar angle becomes progressively smoother and the size of the individual jumps decreases. This indicates hat the individual collisions become softer. At the same time the total number of interactions increases, most noticeably for trajectory E. In this case, the interaction can no longer be characterized as simply a series of discrete collisions, although this is still an element of the interaction.

From figure 4(b), we note that the azimuthal angle of trajectory A does not change during scattering. This projectile remains in-plane throughout the entire process. As the incident direction changes from B to E, oscillations of the azimuthal angle are exhibited by the projectiles. The cumulative effect of these oscillations is to scatter trajectories B, C and D out-of-plane. For trajectory E the atom is scattered in-plane, similar to trajectory A. However, during the scattering process the azimuthal angle does not remain constant as is the case for trajectory A. The rapid zigzag trajectories observed for B to E are a result of the projectile interacting in an alternating fashion with adjacent atomic rows of the crystal surface layer. The atoms of one row tend to push the projectile out-of-plane, while the atoms of the adjacent row tend to push it back toward the in-plane direction. The effect is most pronounced for trajectory E, where the interaction with the two adjacent rows becomes symmetric. The out-of-plane velocity reaches a maximum when the atom passes over the atoms of the second layer. It is then repelled by a crystal atom of the first layer in the adjacent row and deflected back toward the in-plane. Trajectory E represents hyperchanneling [19], where the projectile is confined by the potential provided by surface atomic rows. Also evident in figure 4 (b) is the more complex azimuthal scattering of trajectory D, where strong interaction with one atomic row leads to a large azimuthal scattering angle that is then reduced by a later increase in the level of interaction with the adjacent row. It is clear from this figure that trajectory C also exhibits this effect, albeit in a much weaker fashion than trajectory D.

Figure 5 shows the evolution of the potential between the projectile and the crystal atoms associated with the trajectories shown in figures 3 and 4. In all cases the potential exhibits a series of peaks corresponding to close interactions of the incident Ar with a Si atom. For the purposes of discussion, we define an “effective collision” as being any interaction between Ar

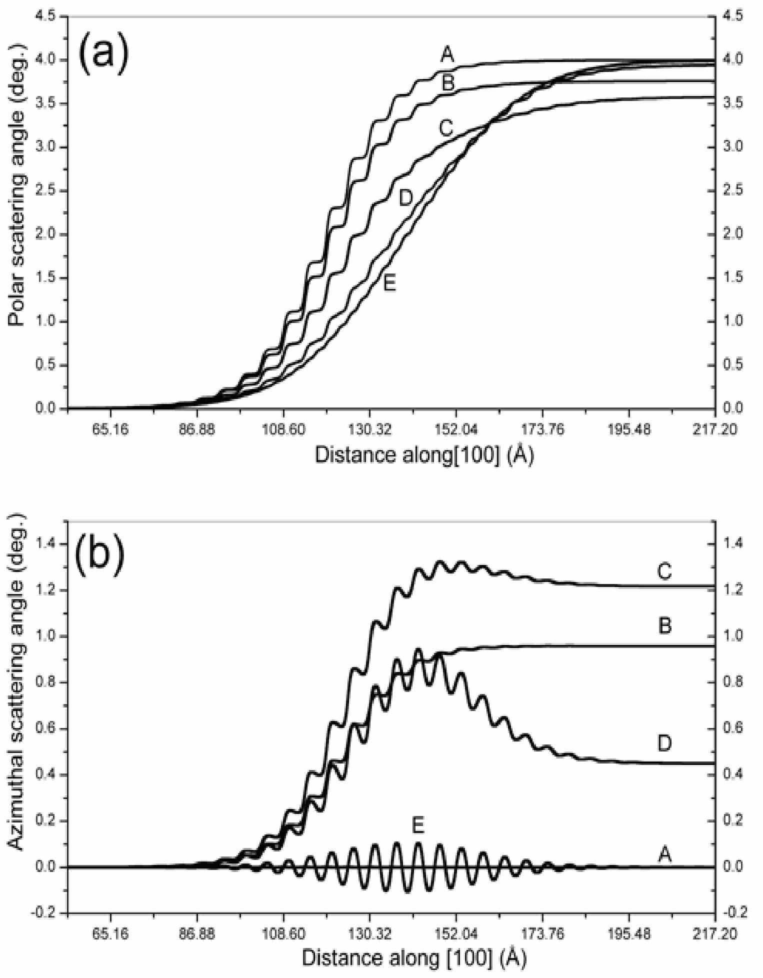

Figure 4: The polar angle (a) and azimuthal angle (b) as a function of the distance along [100] direction for 3 keV Ar scattering from unreconstructed Si (100) using the five trajectories shown in figure 3.

and Si atoms that results in a potential of more than 0.1 eV. Similarly, we define the total interaction length as being the distance between the first and last effective collision along [100] direction. From figure 5, we can see that projectile A experiences the lowest number of effective collisions and that the potential experienced by the projectile is symmetric and returns to zero after each collision. For this case, the BC model may correctly describe the dynamics. The total interaction length for trajectory A is the shortest of the five sample trajectories.

For trajectories B to D, we can see that the projectile experiences an increasing number of collisions and the total interaction length becomes longer. For trajectory B (just off an atomic row of the first layer) the main contribution to the potential experienced by the projectile is from the atoms of that row, consequently the time dependence of the potential remains largely symmetric. For the C and D trajectories, the main interaction is also predominately with the atoms of the first layer. However, in these trajectories the sequential interaction with two adjacent top-layer atomic rows becomes evident. Consequently, there is an increase in the number of potential peaks observed. Since the interaction with the two atomic rows is asymmetric, two distinct components, each associated with a single atom row can be identified in the potential plots. In addition, for trajectories B-D there is an increasing contribution from longer-range interactions with second layer atoms. This is evident from the increase in the 'background' potential experienced by the projectile. As a result the potential

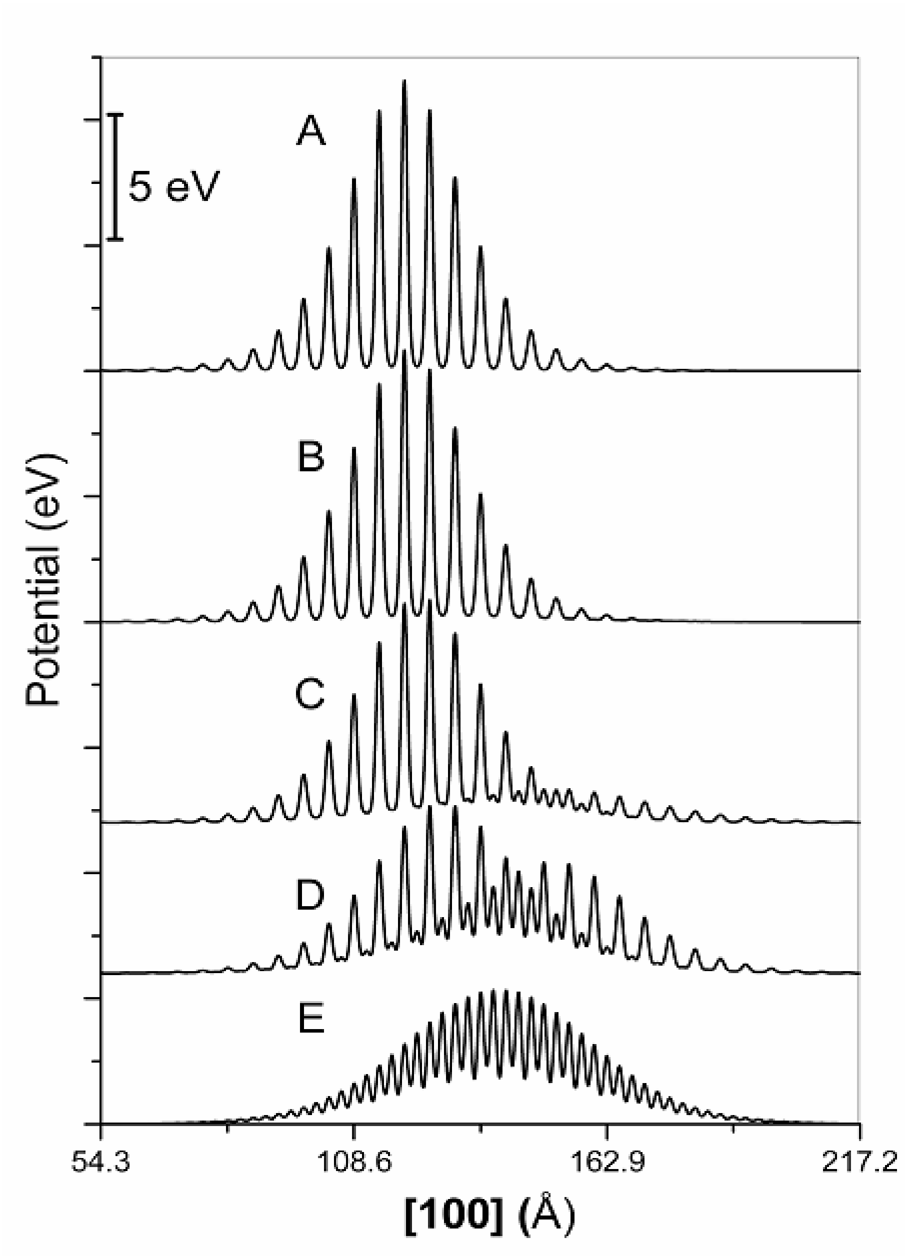

Figure 5: Plots of the potential between the projectile and the substrate atoms during scattering from the surface. The five curves correspond to the trajectories illustrated in the figures 3 and 4.

no longer returns to zero between individual collision events and the BC model cannot correctly describe the dynamics.

Considering trajectory D, during the early stages of the collision the interaction is mainly with the atoms of a single atomic row, while the interaction with the adjacent row is much weaker. Hence the atom is deflected out-of-plane in the direction of the adjacent row. Later in the collision process the interaction with the adjacent row starts to dominate and the atom is pushed back toward the in-plane direction. This leads to the two long-range changes of the azimuthal angle that are seen in figures 3(b) and 4(b).

For trajectory E, due to the interaction with two surface rows, the frequency of effective collisions is double that for trajectory A. The potential does not return to zero between collisions because of the interaction with the second layer atoms. This symmetric nature of the trajectory is reflected in the potential curve. The interaction length is the longest (127.2 Å) while the individual collisions are the softest for this trajectory.

The interaction of the incident Ar with the individual atoms of the surface depicted in figure 5 would not be evident if the continuum model was used instead of MD. For high-symmetry trajectories such as those shown in this paper the difference between the two models is relatively minor. However, if one wishes to study scattering along low symmetry orientations, modeling of individual surface atoms is necessary and the continuum model cannot be applied.

3.3.2 Angular and energy loss distributions

In this section, a total of 3000 trajectories with randomly selected initial x and y coordinates are calculated for 3 keV Ar with an incident angle of 2° along [100] direction of the Si (100) surface. The intensity distributions of the scattered Ar as a function of the polar angle θ, azimuthal angle ϕ and the energy loss *E'* are constructed. This means that we mapped the entire differential cross section $\sigma(\theta,\phi,E^{'})\sin\theta d\theta d\phi dE^{'}$ over a large range. In the histogram, the solid angle is 1.4 x10^{-2} sr. It is well known that the classical scattering cross section can become singular for certain values of θ, ϕ and *E'* [40]. This can be attributed to zeros of functions like $\frac{\partial\theta}{\partial x}$. These singularities are called rainbows [20]. Rainbows are clear signatures of the scattering dynamics and are also found for surface channeling [17, 39].

From the previous trajectory analysis, it is found that the scattering behavior is very sensitive to the y component of the starting points of the projectiles. Therefore, the distance above the surface at the classical turning point, polar angle, azimuthal angle and energy loss are plotted as a function of the y component of the starting points of the projectiles in figure 6 (a2-d2). Their corresponding scattering intensity distributions are shown in figure 6 (a1-d1).

By combining the two sets of figures, peaks in the intensity distribution can be directly correlated with specific starting trajectories above the crystal surface. We also studied if there is a similar dependence on the x component of the starting point of the projectiles. No correlation between identifiable scattering features and the x-coordinate is found. This is not surprising since at grazing incidence each projectile will traverse tens of unit cells along the trajectory path. While close to the surface, an atom with a given initial x-coordinate will, in effect, sample the full range of x-coordinates several times. In contrast, for a given initial y coordinate the range of y-coordinates sampled during close approach is limited and strictly determined by the deflections induced by the collision process.

In the turning point (T_p) versus intensity distribution (figure 6(a1)), two peaks appear at 0.96 Å and 1.44 Å. The sharp peaks look like rainbow singularities and indeed in figure 6 (a2) the partial derivatives $\frac{\partial T_p}{\partial y}$ is equal to zero for the extreme values of T_p. All trajectories have a turning point greater than 0.95 Å, indicating that surface planar channeling occurs for all trajectories and that all of the atoms are reflected from the surface. Combining with figure 6 (a2), the peak at 0.96 Å originates from atoms scattered from the atomic rows of the second layer, similar to trajectory E in the previous section. Similarly, the maximum of the turning point, corresponding to the peak in the intensity distribution at 1.44 Å, consists of the atoms scattered from the rows of the first layer corresponding to trajectory A.

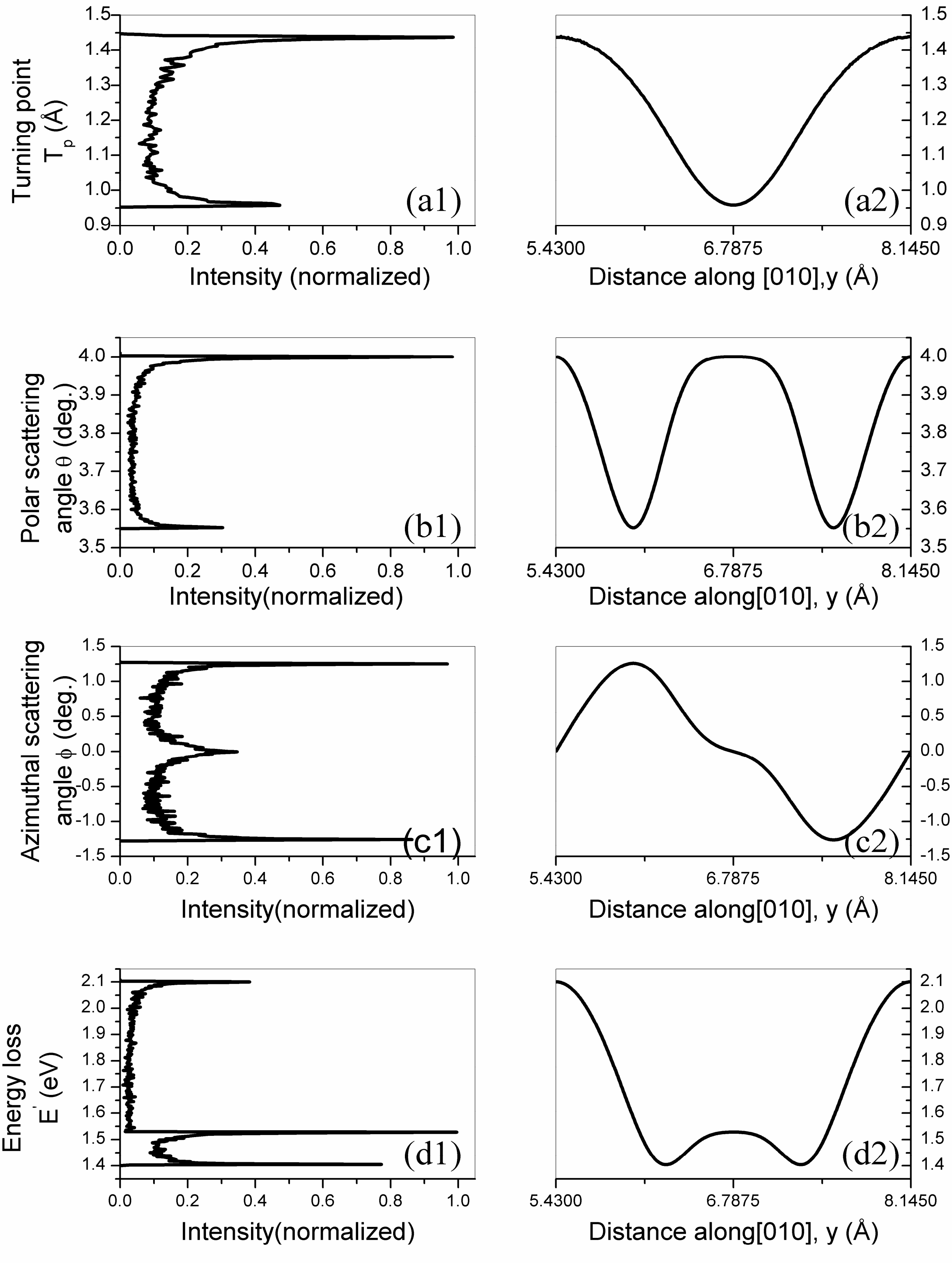

Figure 6: The turning point, polar angle, azimuthal angle and energy loss distributions for 3000 Ar atoms scattered from the unreconstructed Si (100) surface. All trajectories have an incident angle of 2° along the [100] direction. The starting positions are randomly chosen. Plots a1-d1 show the four parameters plotted with respect to the normalized intensity of the scattered particles. Plots a2-d2 show the same parameters plotted as a function of the starting y-coordinate. y=5.43 Å and y= 8.145 Å correspond to trajectories starting directly above a first layer atomic row. y=6.7875 Å corresponds to a trajectory directly above a second-layer atomic row.

also contains two rainbow-like peaks. Linking with figure 6(b2), the peak at 4° (specular scattering) comes from scattering from the atomic rows of both the first and the second layers. The other peak at 3.55° is contributed by the atoms scattered from the region between the rows of the first and second layers. For scattering from a first layer row, the potential comes predominantly from interaction with the atoms of that row. For trajectories aligned with the rows of the second layer, the atoms go closer to the surface and the potential includes contributions from the atoms of both the first and second layers. As a result, the potential along the rows of the second layer is smoother resulting in the broader plateau associated with scattering from this region (see figure 6(b2)). A large region where $\frac{\partial \theta}{\partial y} \approx 0$ leads to a sharp rainbow-like peak.

The azimuthal angle versus intensity distribution (shown in figure 6(c1 and c2)) shows three peaks. The two outermost peaks at ±1.25° correspond to maximum out-of-plane scattering The middle peak comes from in-plane scattering. The symmetry of the intensity distribution reflects the unit cell symmetry. In-plane scattering occurs when the atoms are incident along the first and second layer rows; atoms incident along other trajectories are scattered out-of-plane. It is interesting to note that for ϕ=0, $\frac{\partial \phi}{\partial y} \neq 0$. This results in the intensity enhancement produced by string scattering being significantly weaker than the rainbow features arising as a result of maximum out-of-plane scattering.

The energy loss distributions (in figure6 (d1) and (d2)) show a distinct triple-peak structure. From these two figures, the lowest energy peak at 1.4 eV is contributed by scattered atoms whose starting points are just off the median point between the atomic rows of the first and second layers. When the starting points are near the second layer atomic rows, the energy loss increases, resulting in the peak at 1.5eV. As mentioned above, in this region the potential is smoother and symmetric, causing the plateau in the figure 6(d2). Atoms aligned with the outermost atom rows experience the highest energy loss corresponding to the peak at 2.1 eV. In ll cases, the elastic energy loss is very small at grazing incidence. If inelastic loss processes were included in the simulation, they would be dominant and the energy loss due to nuclear collisions would be negligible.

Rainbow features show up nicely in the plots because the surface temperature is zero. If simulations are performed at higher temperature, thermal vibrations of the surface atoms will result in the disappearance of the rainbow features. The effect of lattice vibrations at elevated temperatures is to wash-out the fine structure that is evident at 0 K. The larger the area where $\frac{\partial P}{\partial y}$ is close to zero (where P is T_p, θ or ϕ), the higher the chance of observing such features at finite T_s.

Figure 7(a) shows the variation of the polar scattering angle as a function of the associated azimuthal angle. We note that the polar angle decreases with increasing azimuthal angle. When specular scattering ($\theta = 4°$) occurs, the azimuthal angle is minimum (0°). In the corresponding intensity distribution on the right-hand side three peaks appear. One is from in-plane scattering. The other two peaks are from maximum out-of-plane scattering and arise from projectiles scattering from the surface region between the atomic rows of the first and second layers. Indicated in figure 7(a) are the points corresponding to the five sample trajectories discussed in the previous section. Points A and E coincide, while point C is close to the maximum azimuthal angle. The variation of the polar scattering angle as a function of the azimuthal angle, when moving the incident trajectory from the point of maximum azimuthal deflection toward the top of the first layer atomic row (point A), is almost identical

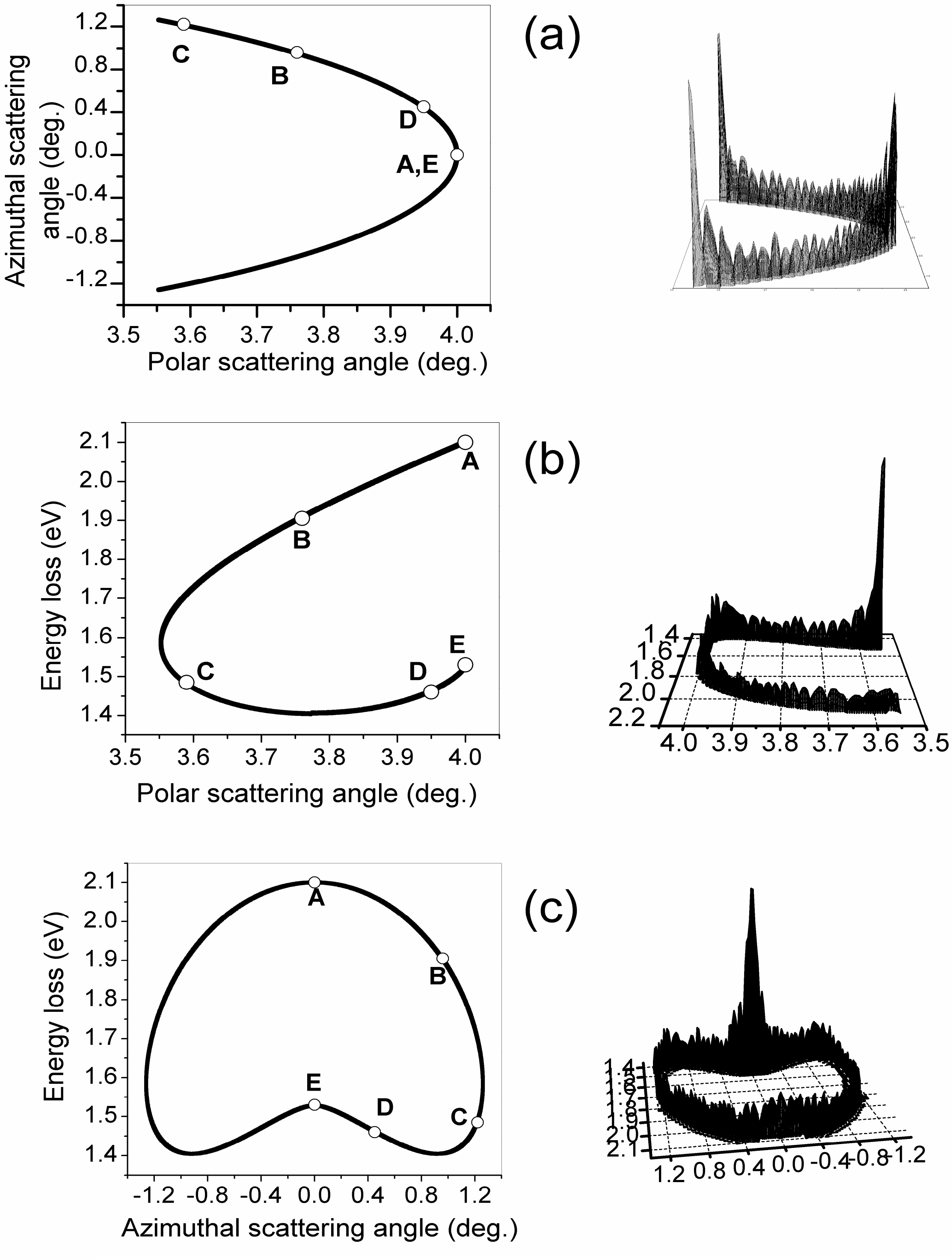

Figure 7: (a) The polar angle as a function of azimuthal angle. **(b)** The energy loss as a function of the polar angle. **(c).**The energy loss as a function of the azimuthal angle. In all there cases the intensity distributions are constructed from 3000 random trajectories.

to the variation observed when moving toward the top of the second layer row (point E). The rainbow features discussed previously can clearly be recognized in figure 7(a).

Figure 7(b) shows the polar scattering angle as a function of energy. Again, the points corresponding to our sample trajectories are indicated on the figures. At point A, the energy loss is at its maximum. Moving from trajectory A toward B, the energy loss decreases with the polar scattering angle. The polar angle reaches the minimum between points B and C. Moving through the C trajectory; the energy loss continues to decrease, but now with an increasing polar angle. At a point between the C and D trajectories, the energy loss reaches its minimum and begins to increase with the polar angle as the D trajectory is approached. Finally, from point D to point E, the energy loss continues to increase with increasing polar angle. At E, the polar angle has returned to the maximum value, but with smaller energy loss than for point A. The energy loss at this point is at a local maximum. In the corresponding intensity figure, the main peak is at point E. This is formed by projectiles whose starting y component is close to the atomic rows of the second layer (close to trajectory E). The peak is a result of focusing of these trajectories by adjacent first-layer rows. Similarly, for the scattering azimuthal angle versus energy loss shown in figure 7(c), at point A, the projectiles undergo the maximum energy loss and minimum deflection (ϕ= 0º). As the trajectory is varied along B toward the C point, the energy loss decreases while the azimuthal angle increases. Shortly before point C, the projectiles' azimuthal angle reaches its maximum. Progressing onward through C, the energy loss continues to decrease, now with a decreasing azimuthal angle. At a point between trajectories C and D, the projectile experiences the minimum energy loss. Finally, along through D to E, the energy loss increases with decreasing azimuthal angle. At point E, the azimuthal angle returns to the minimum. Similarly, in the intensity figure, the peak is contributed by the projectiles whose starting y component is around the atomic rows of the second layer. Note that when the scattered intensity is plotted as a function of both the energy loss and the polar (or azimuthal) scattering angle, only one of the three peaks observed in the 2-D energy distribution (figure 6(d1)) remains evident. The other peaks are spread out in the angular distribution.

The intensity distributions shown figure 7 and in figure 6(b1-d1) are representative of the type of distributions that can be measured experimentally. These figures illustrate how peaks in the scattered distribution can be correlated with particular structures on the surface. In particular, figures 7(b) and(c) demonstrate the strong intensity enhancement that can arise as a result of atomic rows acting to focus the incoming projectiles. Of course, such pronounced features can not be observed experimentally since thermal vibrations, electronic processes and surface defects all act to defocus the scattered projectiles. However, with the inclusion of vibrational and electronic effects, detailed modeling allows the correlation of experimentally observed scattering distributions with specific structural features of the surface.

3.4 Conclusion

In this study, grazing scattering of 3 keV Ar from a Si(100) surface is simulated. In this study, all calculated trajectories underwent surface planar channeling. String scattering occurs when the y coordinate of the starting points is aligned with the atomic rows of the first layer. When the y coordinate is close to the atomic rows of the second layer, surface hyperchanneling is observed. In the simulation the elastic energy loss is small. The energy loss and angular distribution are sensitive to the impact points and rainbow scattering under surface channeling can be observed nicely.

The source code appears to work well, producing simulated results that are physically reasonable. Due to the initially static surface and the neglect of electronic processes, the way in which surface topography influences the scattered distribution can be clearly observed. It can be concluded that full MD is required in order to fully model the interaction process. With the inclusion of inelastic processes such simulations should act as an important compliment to grazing incidence experiments on clean and plasma treated surfaces.

References

[1] J.W. Rabalais, Low Energy Ion-Surface Interaction, Now York, Wiley, 1993.
[2] R. Brako, D.M. Newns, Rep. Prog. Phys. 52 (1989) 655.
[3] H. Niehus, W. Heiland, E. Taglauer, Surf. Sci. Rep. 17 (1993) 213.
[4] J. Los, J.J.C. Geerlings, Phys. Rep. 190 (1990) 133.
[5] J.P. Gauyacq, A.G. Borisov, J. Phys.: Condens. Matter 10 (1998) 6585.
[6] S.R. Kasi, H. Kang, C.S. Sass, J.W. Rabalais, Surf. Sci. Rep. 10 (1989) 1.
[7] M. Maazouz, L. Guillemot, V.A. Esaulov, D.J. O'Connor, Surf. Sci. 398 (1998) 49.
[8] D.B. Graves, M.J. Kushner, J. Vac. Sci. Technol. A 21 (2003) S152.
[9] B. Hird, R.A. Armstrong, P. Gauthier, Phys. Rev. A 49 (1994) 1107.
[10] F. Xu, G. Manico, F. Ascione, A. Bonanno, A. Oliva, R.A. Baragiola, Phys. Rev. A 57 (1998) 1096.
[11] R. Souda, K. Yamamoto, W. Hayami, T. Aizawa, Y. Ishizawa, Phys. Rev. Lett. 75 (1995) 3552.
[12] A.-S. Barbara, J. Appl. Phys. 94 (2003) 4776.
[13] F.A. Cameron, B.G. David, J. Appl. Phys. 86 (1999) 5938.
[14] T. Bernhard, R. Pfandzelter, H. Winter, Surf. Sci. 543 (2003) 36.
[15] W. Yutong, G. Eric, E.M. Theodore, J. Vac. Sci. Technol. A 14 (1996) 2554.
[16] H. Winter, Phys. Rep. 367 (2002) 387.
[17] H. Winter, A. Schűller, Nucl. Instr. and Meth. B 232 (2005) 165.
[18] A. Robin, W. Heiland, J. Jensen, J.I. Juaristi, A. Arnau, Phys. Rev. A 64 (2001) 052901.
[19] Z.L. Fang, W.M. Lau, J.W. Rabalais, Surf. Sci. 581 (2005) 1.
[20] A.W. Kleyn, T.C.M. Horn, Phys. Rep. 199 (1991) 192.
[21] J. Lindhard, J. Phys. Lett. 12 (1964) 126.
[22] D. S. Gemmell, Rev. Mod. Phys. 46 (1974) 129.
[23] F. Gou, M.A. Gleeson, A.W. Kleyn, Vacuum, 81 (2006) 196.
[24] D. C. Schram, Nucl. Instr. and Meth. B 139 (1998) 136.
[25] T.R. Mark, M.T. Ian, Phys. Rev. B 9 (1974) 5008.
[26] A.D. Tenner, K.T. Gillen, T.C.M. Horn, J. Los, A.W. Kleyn, Phys. Rev. Lett. 52 (1984) 2183.
[27] A.D. Tenner, R.P. Saxon, K.T. Gillen, D.E. Harrison, T.C.M. Horn, A.W. Kleyn, Surf. Sci. 172 (1986) 121.
[28] A.D. Tenner, K.T. Gillen, A.W. Kleyn, Nucl. Instr. and Meth. B 17 (1986) 108.
[29] D. Danailov, K. Gärtner, A. Caro, Nucl. Instr. and Meth. B 153 (1999) 191.
[30] D. Danailov, J.H. Rechtien, K.J. Snowdon, Surf. Sci. 259 (1991) 359.
[31] M.P. Allen, D.J. Tildesley, "Computer Simulation of Liquids", New York, Oxford Science Publications, 1987.
[32] G. Moliere, Z. Naturforsch A2 (1947) 133.
[33] H. Feil, J. Dieleman, B.J. Garrison, J. Appl. Phys. 74 (1993) 1303.
[34] M.E. Barone, D.B. Graves, J. Appl. Phys. 77 (1995) 1263.
[35] I.M. Torrens, "Interatomic Potentials", New York, Academic Press, 1972.
[36] D.J. O'Connor, J.P. Biersack, Nucl. Instr. and Meth. B 15 (1986) 14.

[37] J. Tersoff, Phys. Rev. Lett. 56 (1986) 632.
[38] R.J.W.E. Lahaye, A.W. Kleyn, S. Stolte, S. Holloway, Surf. Sci. 338 (1995) 169.
[39] W. Swope, H. Andersen, P. Berens, K. Wilson, J. Chem. Phys. 76 (1982) 637.
[40] T.C.M. Horn, A.W. Kleyn, E.A. Gislason, Chem. Phys. 127 (1988) 81.

Chapter 4

MD simulation of Ar scattering from defected Si (100) at grazing incidence

Abstract: In the present study we present molecular dynamics simulations of Ar scattering from perfect and point-defected Si(100) surfaces at grazing incidence. For scattering from the smooth surface, the effect of changing the incidence angle on surface channeling is discussed. Point defects are simulated by the random addition of adatoms to the smooth surface. The simulated results demonstrate that the angular and energy distributions of the scattered particles are extremely sensitive to small adatom coverages. Experimentally, the bulk of energy lost during scattering at grazing incidence is as a result of inelastic energy loss processes. An electron-stopping model is included in the simulations to account for such inelastic processes.

4.1 Introduction

Grazing-incidence ion scattering can be used to probe the structure of clean and defected surfaces [1-3]. At grazing angles, incident particles can travel a long distance parallel to the surface, while not penetrating very deep into the sample. The projectile trajectories are highly sensitive to both short- and long-range lateral surface structure. Consequently, grazing incident scattering is potentially a good technique for monitoring the modification of surfaces in real-time [4; 5]. An example of a possible application is as a probe of the interaction of plasma with surfaces. We have built an instrument to study plasma-treated surfaces in real-time and in-situ by means of grazing incidence ion scattering. The desire to better understand and interpret the experimental data produced prompted us to undertake a complementary program of simulations [6].

Typically surfaces under investigation will initially be (atomically) smooth and well ordered. In many cases single-crystal samples will be used. Under grazing incidence, projectiles can follow ‘special’ trajectories (channeling effects) as a result of long-range order on the surface [7; 8]. Fang et al have performed classical molecular dynamics (MD) simulations to provide a detailed study of Ar channeling on the Pt(111) surface [9]. They found that the projectile-surface interaction geometry, the projectile type and the surface structure had strong influences on the channeling phenomena. Plasma-treatment of surfaces may lead to the formation of defects. Such defects will disrupt the long-range order of the surface and will alter the scattering behavior. A detailed understanding of the influence of defects on the scattering process is necessary for a correct and complete interpretation of experimental data. Pfandzelter reported the effects of defects (thermal displacements, surface steps and islands) on the scattering process using the binary collision approximation [10]. He reported that the angular distributions of the scattered particles depend directly on the defect structure of the outer-most surface layer.

In the present study, we present molecular dynamics (MD) modeling of scattering from perfect and defected Si (100) at grazing incidence with respect to the surface plane. MD has been widely used in modeling the grazing incidence scattering [7; 8]. In scattering from defect-free Si (100), we discussed the surface channeling of Ar. We show the results of Ar scattering from surfaces with point defects. Finally, the incorporation of the electron stopping in the simulations results in a good agreement with experimental data.

4.2 Description of the simulation

Details of the MD method used can be found elsewhere, but we describe the procedure briefly here. Molecular dynamics simulations track the particles in a system by numerically integrating Newton’s equations of motion. The net force exerting on each atom is derived from an inter-atomic potential energy function. In current simulations, the Molière potential is used to describe the Ar interaction with Si atoms in the substrate. The Morse potential was used to describe the interactions between the silicon atoms. More details about the potentials used can be found in references [6; 11].

The target consisted of a “box” containing three layers of atoms. Increasing either the number of layers or the number of atoms in each layer did not affect the calculated trajectories. The side of the box facing the incident atoms served as the unreconstructed Si(100) surface. For the other sides, the atoms were fixed to their equilibrium positions. All atoms inside the box and at the surface were movable under force. At the beginning, the atoms were placed at their equilibrium positions. For scattering from the surface at 0 K, zero-point motion of the lattice atoms was neglected.

At the beginning of each trajectory, the incident Ar was initially placed at 5 Å above the surface, where the potential was less than 10^{-5} eV, with a random (x, y) position relative to one of the surface unit cells. We use the velocity Verlet scheme with a variable time step to numerically integrate Newton’s equations of motion [12]. For each time-step in the trajectory, pair potentials were summed for atoms within a defined radius of the incident atom. Both the radius and the integration time-step were chosen to achieve an accuracy of better than 0.1% deviation of the total energy. Polar angles are defined with respect to the surface plane. Azimuthal angles are defined with respect to the plane described by the initial Ar trajectory and the surface normal.

In order to account for the inelastic energy loss mechanisms, a simple electron-stopping model based on the model outlined by Ferrell et al. can be incorporated into the simulations [13]. In the model used, the energy lost per unit length when an ion of charge, Ze, moves with velocity, *V*, located a distance Z_0 from the surface and is given by:

$$dE / dZ = \frac{2.0(Z_e)^2 (r_s)^3 M_{ep}}{3.0(Z_0)^3} V$$

where r_s represents the averaged one electron radius and M_{ep} is the ratio of the mass of an electron to the mass of a proton. In the simulation r_s is the only adjustable parameter and determines the quality of the fit between the simulation and the experimental data.

4.3 Results and Discussion

Atomic scattering at grazing angles along a low index direction of a single crystal surface is dominated by a series of small-angle collisions with surface atoms [6]. Figure 1 shows top- and side-views of selected trajectories for 4 keV Ar scattering from Si(100) surfaces along the [100] direction. The trajectories were selected to illustrate surface channeling effects. The same subset of atom starting conditions was calculated for incidence angles of 2°, 4° and 7° with respect to surface plane. From the side view in figure 1(a) we note that for 2° incidence the Ar atoms do not penetrate the surface, but none-the-less there is an apparent focusing effect observable in the top-down view. For 4°, the incident atoms penetrate into the first layer, but not to the depth of the second layer. Zig-zag trajectories are clearly observed between the atomic rows. For 7° the Ar atoms penetrate to the depth of the second layer. The lateral interaction length is shortest because of the relatively large angle of incidence. In all three cases it is apparent from the top views that the atoms are being confined between two atomic rows of the first layer and a channeling effect is operative. As the incident angle is increased, the mechanism changes from planar- to hyper- to sub-surface channeling (see the work of Fang et al [9]). The essential mechanism is the same in the three cases, with the normal energy of the incident particles dictating the depth of penetration into the surface.

In order to understand the affect of defects on scattering, different Si adatom coverages are placed randomly on the smooth Si(100) surface prior to scattering. A total of 3000 trajectories with randomly selected initial x- and y-coordinates were calculated for 3 keV Ar incident at a polar angle of 2° along [100] direction of the surface. As seen from figure 1(a), at this angle of incidence the atoms do not penetrate to the depth of the first layer during scattering. The defect density is defined as the ratio of Si adatoms to the number of Si atoms in a complete surface layer. In our simulations, we compared defect densities of 0.0 (no adatoms), 0.1, 0.3, 0.5, 0.7 and 0.9. Figure 2(a) shows the resulting scattered distributions as a function of the polar scattering angle for the different defect densities. From the figure, we note that the shape of the distribution is very sensitive to the adatom density. For the defect-free surface, atoms are scattered in a narrow distribution centered on the specular scattering angle (4°). With the addition of a 10% coverage of Si adatoms, the maximum of the scattered intensity also occurs around the specular angle, but the distribution is now much broader and the intensity at maximum much lower. As the defect density is increased, the scattered distribution becomes progressively sharper and begins to resemble scattering from the smooth surface at a defect density of 0.9.

Figure 2(b) shows the full-width at half-maximum (FWHM) of the polar scattering distributions as a function of the adatom density. For the perfect crystal, the FWHM is ~0.3°. At a defect density of 0.1 it is ~1.4°. The FWHM decreases gradually as the defect density increases from 0.1 to 0.5, while for densities from 0.5 to 0.9 it decreases sharply. The two regions evident from figure 2(b) represent a shift in the nature of the defected surface being simulated. For defect densities less than 0.5, the surface can be described as a smooth crystal with adatoms. Once the defect density is greater than 0.5, the adatoms begins to resemble an atomic layer with point vacancies. Figure 2 clearly demonstrates that grazing scattering is much more sensitive to the presence of adatoms than to vacancies and that the most dramatic

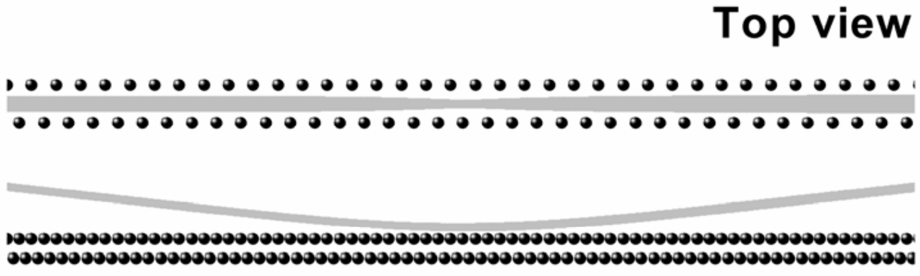

(a) 2° incidence angle

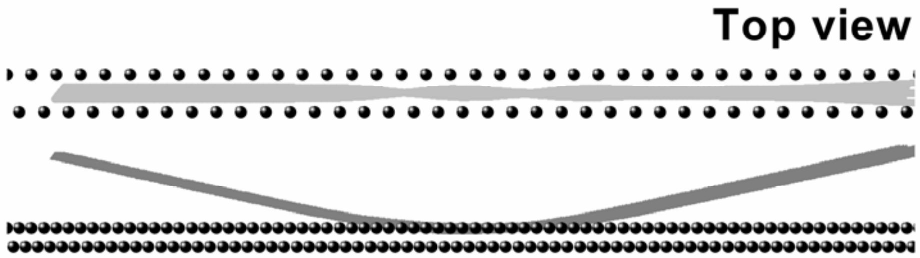

(b) 4° incidence angle

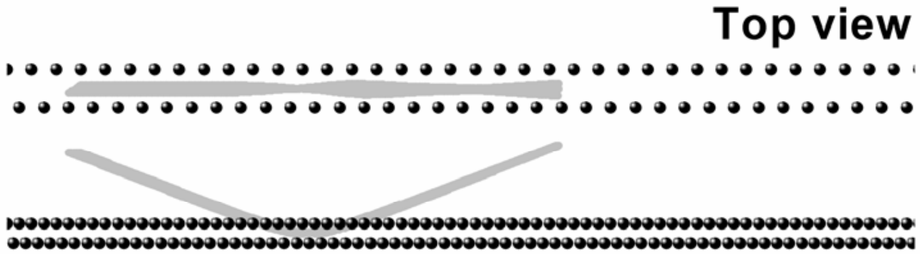

(c) 7° incidence angle

Figure 1: Top- and side-views of selected trajectories for 4 keV Ar scattering from Si(100) along the [100] direction. The surface temperature was 0 K and incident angles of **(a)** 2°, **(b)** 4°, and **(c)** 7° were calculated.

effect occurs for very low adatoms coverages. As illustrated by figure 1, grazing incidence scattering from an ideal surface is characterized by smooth, long-range interactions. The scattered distributions will be most sensitive to any defect that can readily disrupt this process. At grazing incidence vacancy defects are shielded from the incident projectiles by shadowing effects. Adatoms are much more likely to give rise to hard (small impact parameter) collisions and hence to significantly alter the scattered distribution. Note that by increasing the incidence angle, as shown in figure 1, the scattering can be made more sensitive to the presence of vacancies. At larger angles of incidence (for a fixed incident

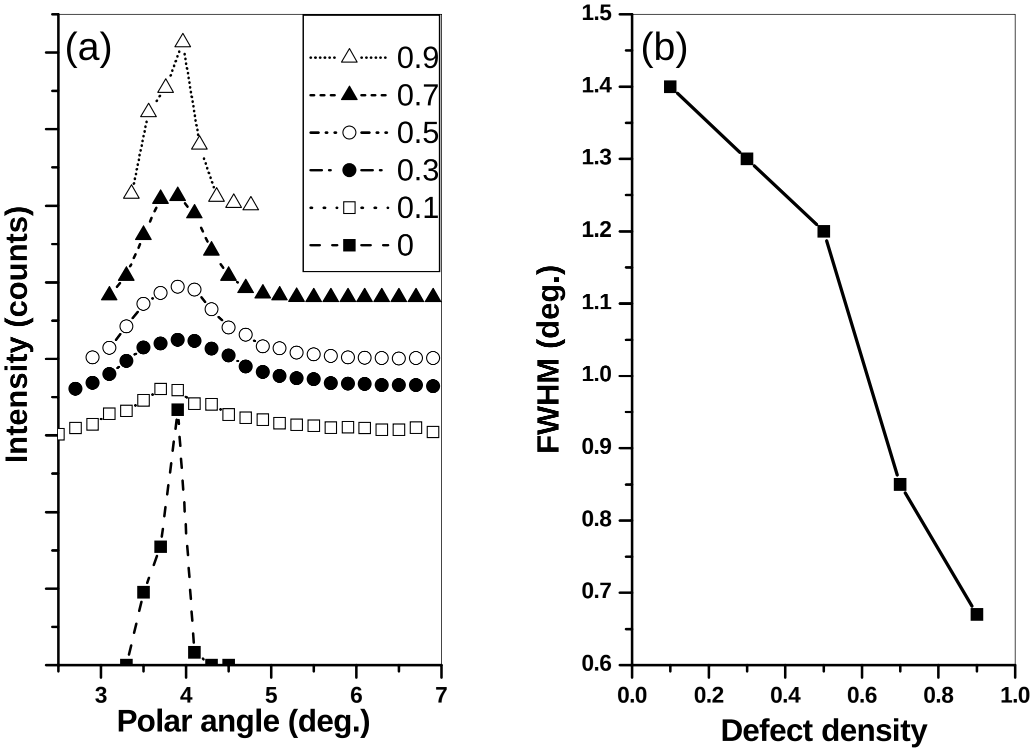

Figure 2: (a) Scattered distributions for 3 keV Ar as a function of the polar angle for different defect densities at 300 K (incident angle of 2°). **(b)** Full-width at half-maximum (FWHM) of the polar scattering distribution as a function of the adatom density.

energy) the lateral interaction distance is reduced and the atom penetrates deeper into the surface. Both effects will enhance the relative influence of vacancies on the scattering process.

Figure 3 shows the distributions of scattered atoms as a function of the azimuthal scattering angle. Three peaks are evident from the smooth surface. The two outermost peaks at ±1.25°, corresponding to maximum out-of-plane scattering, are rainbow features that arise as a result of scattering from the atomic rows of the first layer [6]. Atoms incident along trajectories not aligned with the atomic rows tend to be scattered out-of-plane. The central peak is due to in-plane scattering, occurring when atoms are incident along trajectories aligned the first and second layer atomic rows. From the figure, we note that all three peaks are strongly dependent on the adatom density. Similar to figure 2, the biggest effect is observed for the lower adatom densities. For low defect densities all three peaks are absent from the scattered distributions. The peak at 0° is the first to re-emerges as the defect density is increased. The out-of-plane scattering features are slower to re-emerge since they require a greater degree of surface order (adjacent atomic rows) than the in-plane scattering peak.

Figure 4 shows the scattered distribution as a function of the *elastic* energy loss for the different defect densities. For a perfect crystal, the peak in the energy loss distribution is at about 2.7 eV. Similar to figures 2 and 3, the addition of adatoms results in significant changes in the calculated distribution. However, in this case the largest effect does not occur for the 0.1 defect density. With 10% adatom coverage, the distribution is very broad, but the position of the peak maximum is unchanged. When the defect density is increased to 0.3, the entire distribution is shifted to a larger energy loss. As the defect density is increased further, the distribution gradually reverts to that of the smooth surface.

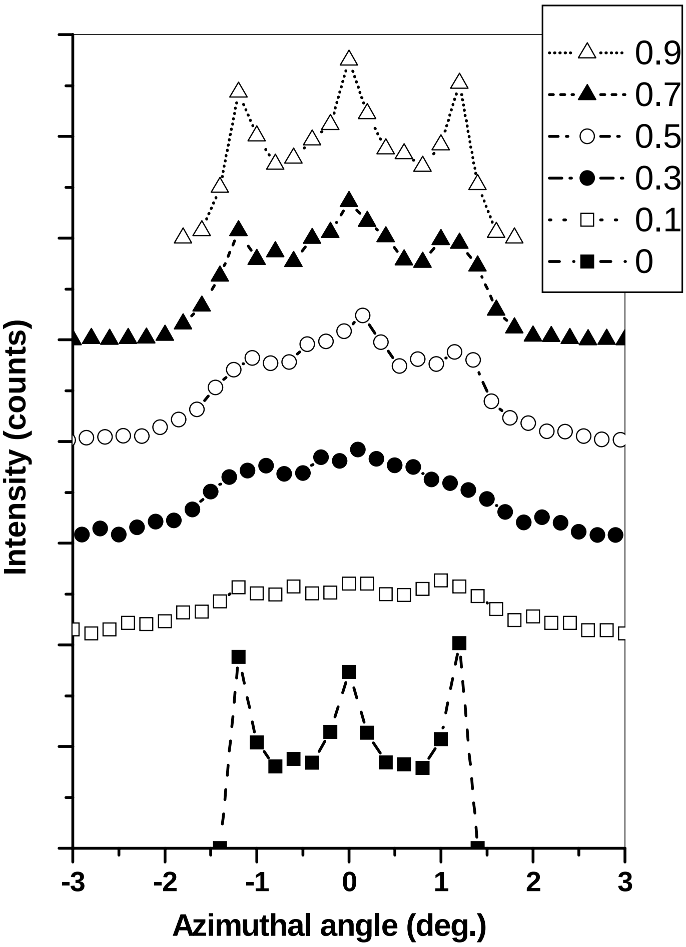

Figure 3: Scattered distributions for 3 keV Ar as a function of the azimuthal angle for different defect densities at 300 K (incident angle of 2°).

The preceding discussion has focused solely on the scattering of neutral Ar atoms from surfaces and only considered mechanical loss processes are considered. In reality, most experiments of the type we seek to simulate will involve incident ions and electronic loss processes will dominate the interaction [3]. In order to account for this, the loss model outlined in the previous section was incorporated into the code. Figure 5 shows a comparison between an experimental measurement for 2.5 keV Ar^+ incident at 2.5° with respect to the surface and a simulated energy loss spectra with the inclusion of the inelastic model. Details of the experimental set-up and procedures can be found in [14]. It is immediately evident from the experimental data that the energy loss is much larger than that predicted on the basis of elastic scattering (figure 4). Using the inelastic energy loss model, with r_s=1.35 $Å^{-1}$, the simulated energy loss shown was obtained. By incorporating the electron-stopping model into the simulation good agreement between the calculated energy loss and the experimental data can be obtained.

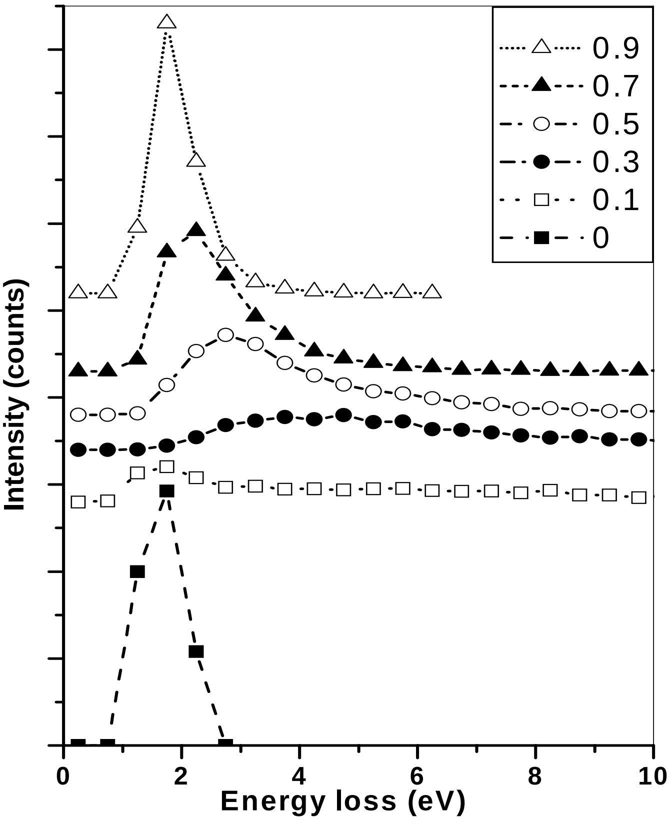

Figure 4: Scattered distributions for 3 keV Ar as a function of the elastic energy loss for different defect densities at 300 K (incident angle of 2°)

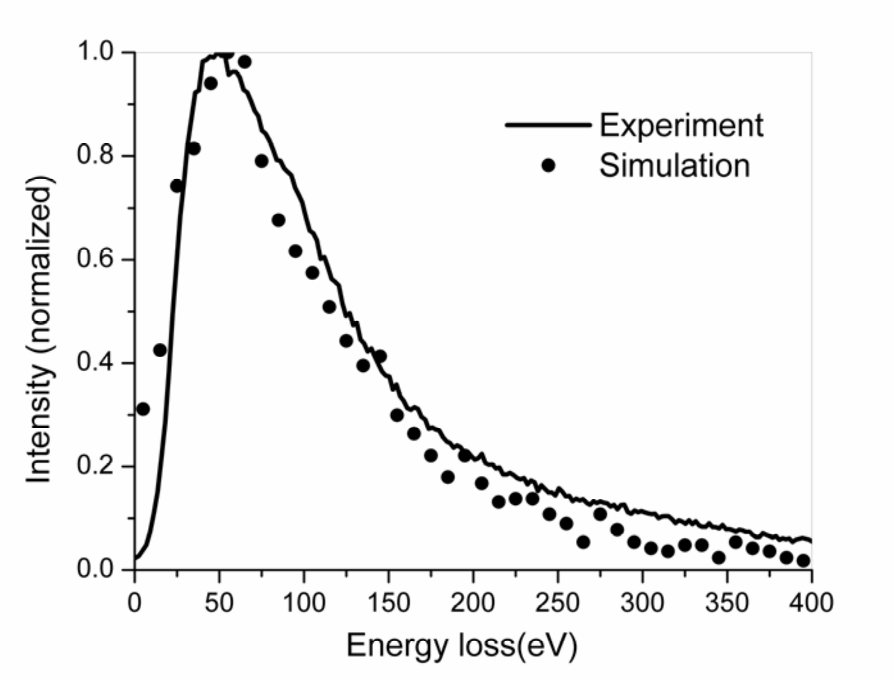

Figure 5: Comparison between experimental and simulated (including electron stopping model) energy loss spectra for 2.5 keV Ar^+ incident at 2.5° and 300 K.

It is necessary to address the charge state of the projectile used in the current simulations and the applicability of the results to typical experimental measurements. The simulations are performed for neutral atoms. The inelastic energy loss model is used in figure 5 to account for inelastic loss processes (in effect all electronic process). Previous figures show simulations that do not include this model, and so no electronic effects are considered. The mechanical scattering features predicted should be equally applicable to the scattering of ions and neutrals (neglecting image-charge effects, whose main influence will be to increase the effective angle of incidence). In addition, efficient neutralization of the incident ions means that for the bulk of the interaction time the majority of projectiles will be neutral atoms. The inelastic energy loss makes it difficult to derive information on defect densities from the energy loss spectra. In order to determine if the inelastic loss model also changes the simulated angular distributions, we compared the distributions (polar and azimuthal) obtained for simulations including the inelastic loss model with those considering only elastic effect. The angular features observed were not significantly altered by the inclusion of the model (see also [10]). Hence, the conclusions reached on the basis of figures 1-3 are not altered.

4.4 Conclusion

In this study, MD simulations were performed to investigate Ar scattering from perfect and defected silicon surfaces. The results clearly indicate that grazing incidence ion scattering has potential as a probe of defect formation at surfaces. For very grazing incidence, the largest effect is observed in the angular distributions of scattered Ar for low adatom densities. Hence, grazing scattering is most sensitive to the initial stages of layer formation during deposition and the final stages of layer removal during etching (assuming layer-by-layer removal). Vacancies are much less visible at very grazing angles, but the relative sensitivity to such defects can be influenced by changing the incidence angle. Experimentally, inelastic processes dominate energy loss at grazing incidence. By incorporation of an electron-stopping model into the simulations, good agreement could be obtained with experimentally measured data.

References

[1] J. W. Rabalais, Low Energy Ion-Surface Interaction, Now York, Wiley, 1993.
[2] H. Winter, Prog. Surf. Sci. 63 (2000) 177.
[3] H. Winter, Phys. Rep. 367 (2002) 387.
[4] L. Pedemonte, G. Bracco, R. Tatarek, R. Beikler, E. Taglauer, K. Bruning, W. Heiland, Nucl. Instrum. Methods Phys. Res., Sect. B 193 (2002) 557.
[5] R. Pfandzelter, T. Igel, M. Ostwald, H. Winter, Appl. Surf. Sci. 142 (1999) 470.
[6] F. Gou, M. A. Gleeson, J. Villette, A. W. Kleyn, Nucl. Instrum. Methods Phys. Res., Sect. B 247 (2006) 244.
[7] D. Danailov, K. Gartner, A. Caro, Nucl. Instrum. Methods Phys. Res., Sect. B 153 (1999) 191.
[8] D. M. Danailov, D. J. OConnor, K. J. Snowdon, Surf. Sci. 347 (1996) 215.
[9] Z. L. Fang, W. M. Lau, J. W. Rabalais, Surf. Sci. 581 (2005) 1.
[10] R. Pfandzelter, Phys. Rev. B 57 (1998) 15496.

[11] M. P. Allen, D. J. Tildesley, Computer Simulation of Liquids, New York, Oxford Science Publications, 1987.
[12] W. C. Swope, H. C. Andersen, P. H. Berens, K. R. Wilson, J. Chem. Phys. 76 (1982) 637.
[13] T. L. Ferrell, P. M. Echenique, P. H. and Ritchie, Solid State Commun. 32 (1979) 419.
[14] F. Gou, M. A. Gleeson, J. Villette, A. W. Kleyn, Vacuum 81 (2006) 196.

Chapter 5

Theoretical modeling of energy redistribution and stereodynamics in CF scattering from Si(100) under grazing incidence

Abstract: We have simulated CF scattering from Si (100) using the molecular dynamics method. Translational energy loss spectra are presented. The shape of the energy loss distribution as a result of internal energy release is analyzed. At the classic turning point, the internal energy of the molecule is mainly in form of rotational energy. The strong rotational excitation results in additional molecule-surfaces interactions during the latter half of the collision. These additional collisions permit some molecules that initially gain internal energy exceeding the bond strength to ultimately survive the collision process via rotational de-excitation. The rotational motion exhibited by surviving molecules is determined by the combination of the molecular axis orientation and the local surface structure during the collision process. The rotation planes of the surviving molecules are preferentially aligned with the surface normal (cartwheel-like and propeller-like motions). In this study, propeller-like motion of the surviving molecules is observed for the first time. The majority of surviving molecules exhibit a cartwheel-like motion. However, molecules that gain a propeller-like rotation exhibit a much better alignment of their planes of the rotation compared with molecules exhibiting cartwheel-like motion.

5.1 Introduction

Understanding the interaction of gas-phase molecules with solid surfaces has relevance for a wide range of technologically important processes [1-4], including catalysis, surface modification, etching and passivation. The interaction can be broadly split into two components, the electronic and the mechanical. Invariable both components are operative, but the relative importance varies depending on the particular molecules and surfaces involved and on the initial state of the molecule. Investigating the interaction of molecules with surfaces is challenging when compared to atom-surface studies. Molecular interaction contains the added possibilities of excitation of internal modes and/or dissociation. Given the extra complexity, it can often be difficult to experimentally distinguish the root cause of a particular observation. In this regard, computer simulation is a valuable tool for providing explicit information about the dynamics of molecules over short (picosecond) time scales and is ideally suited to the microscopic study of molecule-surface interaction and related phenomena [5; 6].

Previously, simulations have indicated that the degree of collision induced dissociation for grazing incident molecules is primarily determined by the normal energy and is only weakly dependent on the parallel energy [7]. Under grazing conditions, molecules with a large total energy can have normal energies of less than 10 eV. Such energies are typical for the activation of chemical reactions at surfaces. As a consequence, results obtained for grazing incidence (e.g. internal energy uptake and dissociation rate as a function of normal energy) may be qualitatively applicable to less grazing geometries. This is highly advantageous when seeking to study the interaction of low energy (1-50 eV) particles with surfaces. A relative lack of adequate beam sources and efficient detectors hampers experimental investigation in this energy range. Provided normal-energy scaling at grazing incidence can be demonstrated to adequately mimic the dynamics of low energy particles at normal incidence, then more efficient sources and detectors can be applied to the investigation of such low energy particle-surface interactions. Of course, when such an experimental approach is adopted [8; 9], it is necessary to rigorously investigate the applicability and limits of normal energy scaling.

In the past decades much theoretical work has been done on grazing scattering of homo-nuclear diatomic molecules from metal surfaces [2]. Van den Hoek and Kleyn [10] have performed MD simulations of O_2 scattering from the Ag (111) surface over a range of incidence energies from 1eV to 3 keV. These calculations show that for grazing incidence, both the total energy loss and the dissociation fraction go through a maximum at several 10's of eV incident beam energy before becoming independent of total energy beyond several hundred eV while keeping normal energy fixed. Heiland's group performed classical trajectory calculations of fast N_2 scattering from Pd (111) at grazing incidence, based on ab initio density functional theory calculations[6]. Their results show that the molecule-surface interaction seems to be strongly dependent on the azimuthal direction of incidence and the orientation of the molecular axis. Many studies have focused on the rotational dynamics arising from the scattering. Studies by Gerber et al. have shown a strong preference for rotational inelastic transitions resulting in the vibrational deactivation of I_2 scattering from MgO(100)[11]. Relatively few studies have been performed on scattering of hetero-nuclear molecules from surfaces. Martin et al. have studied the dissociation dynamics and energy transfer processes of NO scattering from GaAs (110) [12]. Trajectory calculations by Polanyi and Wolf show that the initial orientation angle of CO strongly affects the final rotational state and angular distribution [13].

In this paper we present MD simulations of CF molecules scattering from the Si (100) surface in order to gain insight into the mechanism of scattering and CID. The current simulations involve molecules incident on the silicon surface at grazing incidence (<10° with respect to the surface plane). One of the primary motivations for the selection of scattering geometry and surface was work being performed using a grazing-incidence ion scattering apparatus at our laboratory. Such experiments can be utilized for the validation of computer models, which can then be applied to the simulation of surface interactions at different geometries and incident energies. Although the current simulations may not be directly comparable to experimental results (since electronic effects have been wholly neglected), the mechanical collision processes outlined in this paper should none-the-less be operative during molecular scattering (as illustrated by the observation of CID effects in the scattering of CF_3^+ from Ag(111) [14]). In terms of relevance to ion scattering, the current work would be directly applicable to incident ions that are not neutralized or are neutralized to the ground state (e.g. via auger neutralization). Comparison between theory and experiments can be used to derive information on electronic processes based on differences as well as similarities.

Molecules that neutralize to an excited state would have an additional internal energy component that is absent in the current work. Dissociative neutralization is a factor that is completely absent at present.

Experimentally, relatively little beam work has been performed on the interaction of fluorocarbon molecules with surfaces. The main work that has been done has involved the use of ion beams. Koppers et al. have studied the dissociative scattering of CF_3^+ ions from clean and barium covered Ag (111) surfaces [15]. Unsurprisingly, the results showed that dissociation occurs mainly as a result of electronic processes. However, it was noted that the crystal orientation has a measurable influence on dissociation, indicating that impulsive collisions also played a role in fragmenting the incident molecules. Koppers et al. also investigated CF_x^+ (x=1-3) scattering from a liquid perfluoropolyether (PFPE) surface [16; 17]. PFPE is an insulating surface and consequently fragmentation was solely due to collision-induced dissociation (CID). The degree of dissociation was correlated with the number of bonds in the incident molecule. The results suggested that the orientation at impact played an important role in the degree of internal energy uptake (and hence dissociation) of the incident molecules.

Under grazing scattering conditions, the incident particles are very sensitive to the outermost atomic layers of the surfaces. The combination of small perpendicular velocity and large parallel velocity results in incident molecules traveling a long distance close to the surfaces. The use of a well-ordered surface can give rise to ‘special’ scattering effects. For instance, channeling of atoms by atomic rows on the surface can be observed [9]. In the case of molecular projectiles, the possibility of channeling also exists. In addition, molecular scattering may give rise to experimentally observable effects, either solely due to the molecular orientation (e.g. orientation dependent dissociation [17]) or by the combination of the molecular orientation and the surface structure. In order to properly interpret experimental results, such effects should be accurately identified. Simulation is an ideal tool to check for structural effects in the scattering of molecules. It is trivial to perform calculations with a well-defined starting molecular orientation (equivalent to producing an oriented beam experimentally). Equally, angular distributions, dissociation probability variations and selective excitations of the scattered particles can be readily identified. Of course, observing such effects experimentally may be difficult in many cases. None-the-less simulations can act as a useful indicator of scattering effects that may be experimentally observable.

In the current work we analyze the translational energy loss, the internal energy uptake and the amount of the vibrational and rotational excitation of CF scattered from Si (100). We examine the relationship between dissociation, molecular orientation, orientation of the rotational angular momentum ($\vec{J}$) and the effect of the surface structure and demonstrate that the type of rotational motion exhibited by scattered molecules is closely related to both the initial molecular orientation and the surface structure.

5.2 Description of the molecular dynamics simulation

In this paper we focus on the simulation of CF scattering from Si (100) using a fixed parallel energy of 1500 eV and varying the normal energies ($E_\perp = E\sin 2\theta_i$) from 4 eV to 31 eV. This combination of energies corresponds to incident angles θ_i of between 2.9° and 8.2° with respect to the surface plane. Under such grazing incidence conditions, the scattering mode is expected to change from binary collision between the incident molecules and individual surface atoms to simultaneous multi-body interactions between the molecule and the surface atoms. Many simulations propose that the binary collision model is still suitable at grazing incidence. However, trajectory analysis shows that the binary collision model is not entirely suitable for the grazing scattering case [5]. Consequently, we have utilized MD simulations to examine the scattering of CF from Si (100) surfaces.

Details of the MD method can be found elsewhere [18], but we briefly describe the procedure here. Molecular dynamics simulations calculate the positions and velocities of a system of atoms by numerically integrating Newton's equation of motion. The net force exerted on each atom is calculated from the gradient of an inter-atomic potential energy function. In our simulation we use a pair potential to describe the intermolecular C-F interaction [19].

$$V_{ij}(r) = A_{ij} \exp(-\lambda_{ij} r_{ij}) - B_{ij} \exp(-\mu_{ij} r_{ij})$$

where A_{ij} and B_{ij} are 909.2022 eV and 219.7799 eV. λ_{ij} and μ_{ij} are 3.7128 Å^{-1} and 2.1763 Å^{-1}. The Molière potential is used to describe the interaction of silicon atoms with C and F [20]. We use a spring potential to describe the interaction among the crystal atoms and each crystal atom interacts only with its nearest neighbors [21]. The choice of a spring potential to describe the Si-Si interactions was made in order to reduce the overall computation time. Clearly this is an unphysical description of the way in which the surface atoms interact with each other. However, we believe the use of a spring potential is not significantly detrimental to the computation results due to the incident molecules having a large translational velocity parallel to the surface. As a consequence, the time spent in the vicinity of an individual Si atom is small and the interaction of the molecules with individual silicon atoms is dominated by the initial collision. The subsequent response of the Si atoms occurs after the molecule has left the vicinity and does not influence the trajectory or the energy exchange between the molecule and the surface. Although the energy redistribution within the crystal is not accurately described, this is not relevant to the trajectory of the exciting molecule. Each trajectory is scattered from a 'new' surface, so lattice excitations from one trajectory do not transfer to subsequent molecules.

The use of a spring potential does not permit the sputtering of surface atoms, although this should in principle be possible given the highest normal energy employed (31 eV). Again, due to the large parallel velocity and the use of a fresh surface for each molecule, the neglect of sputtering can be considered a minor omission. If the study were expanded to include surface defect then the issue of sputtering would become more critical. Test trajectories, performed utilizing both Morse [22]and Tersoff potentials [23-25] for the Si-Si interaction, were compared to calculations using the spring potential. There was no significant difference between the molecular distributions observed for the three lattice potentials, supporting the conclusion that a precise description of the Si-Si interaction is not critical for grazing incidence simulations. In order to check the applicability of "normal-energy scaling", some sample calculations were performed using normal incident molecules (no parallel energy). In these cases, the Tersoff Brenner potential was used for the Si-Si interaction.

We use the velocity Verlet scheme with a variable time-step to numerically integrate Newton's equations of motion. For each time-step in the trajectory, pair potentials are summed for atoms within a cut-off distance (R_c = 6Å) of the incident ion from the surface. Given the large surface area required in order to simulate grazing scattering, the use of a cut-off was necessary in order to limit computation time. Both R_c and the integration time step are chosen to achieve an accuracy of better than 0.1% deviation from total energy. Sample calculations were run to confirm that neither increasing Rc nor decreasing the time-step resulted in a significant change in the simulated results. In order to obtain good statistics, at least 10,000 trajectories have been run at each of the incident energies.

The target consists of a “box” containing three layers of atoms. The side of the box facing the incident molecules serves as the unreconstructed Si (100) surface. For the other sides, the atoms are fixed at their equilibrium positions. Atoms inside the box and on the surface are movable under force. The simulated cell was ~160 Å long (in the scattering direction), ~40 Å wide and ~10 Å deep. The surface area was ~6400 Å^2. Test simulations were done to ensure that increasing either the number of layers or the number of atoms per layer did not significantly change the simulation results. At the beginning, the crystal atoms are set to their equilibrium positions and then thermally displaced in terms of the Debye model. According to this, uncorrelated Gaussian distributions are assumed for the atomic displacement and the mean square atomic displacement is proportional to T/Θ, where T is the crystal temperature and Θ is the Debye temperature. The velocity components of the crystal atoms are calculated from the Gaussian distribution. To distinguish thermal effects, results are compared to simulations performed at 0 K (no initial lattice vibration included).

The incident CF molecules are initially placed just above the surface (~6 Å) with a random (X, Y) position, referred to one unit cell on the surface. At this point the surface potential is less than 10^{-5} eV. The incoming (θ_i) and outgoing (θ_f) angles are defined with respect to the surface plane. The polar (in-plane) scattering angle (θ) is defined as the sum of θ_i and θ_f. The azimuthal (out-of-plane) scattering angle (ϕ_i) is measured with respect to the scattering plane, which is defined by the incident atom direction and the surface normal. The initial orientation of the molecular axis is chosen randomly for each trajectory, with proper weighting. The initial angular momentum $\vec{J}$ is zero in order to conserve the orientation until impact. The CF molecules have no initial vibrational energy.

In our calculation, the molecular orientation and the rotational motion are specified by two types of angle: the polar orientation angles, θ_o (θ_J), are between the molecular axis (the rotational angular momentum, $\vec{J}$) and the surface plane; the azimuthal orientation angles, ϕ_o (ϕ_J), are between the projection of the molecular axis (the projection of $\vec{J}$) onto the surface and the initial trajectory along the surface, such that $\phi_o = 0^\circ$ and 180° correspond to the molecular axis projection($\vec{J}$ projection) being parallel to the initial trajectory. In our simulations, $\theta_o = 0^\circ$ and 180° correspond to the molecular axis being perpendicular to the surface; in these instances, no azimuthal orientation is defined. Figure 1(a) shows the definition of the polar and azimuthal orientations of the molecular axis (θ_o and ϕ_o). Similarly, figure 1(b) shows the definition of the polar and azimuthal angles of the rotational angular momentum vector $\vec{J}$ (θ_J and ϕ_J, respectively). Molecular rotation with $\theta_J = 0^\circ$ and $\phi_J = 0^\circ$ is referred to as propeller-like motion (see figure 1 (c)), $\theta_J = 0^\circ$ and $\phi_J = \pm 90^\circ$ is called cartwheel-like motion (figure 1(d)) and $\theta_J = 90^\circ$ is helicopter-like motion (figure 1(e)). The rotational energy at a certain point is defined as $\vec{J}^{\,2}/2\mu r$, where μ is the reduced mass and r is the bond length of the molecule. The internal energy is calculated as the sum of the relative kinetic energy and the relative potential energy of the molecule.

5.3 Results and discussion

5.3.1 Energy loss distributions and degree of dissociation

We begin by presenting simulated energy loss distributions of the scattered particles for CF incident on Si(100) at four different normal energies ($E_\perp$= 4 eV, 13 eV, 19 eV and 28 eV). In each case the parallel energy was 1500 eV and the surface temperature was 300 K. Increasing the normal energy while maintaining a fixed parallel energy means that the

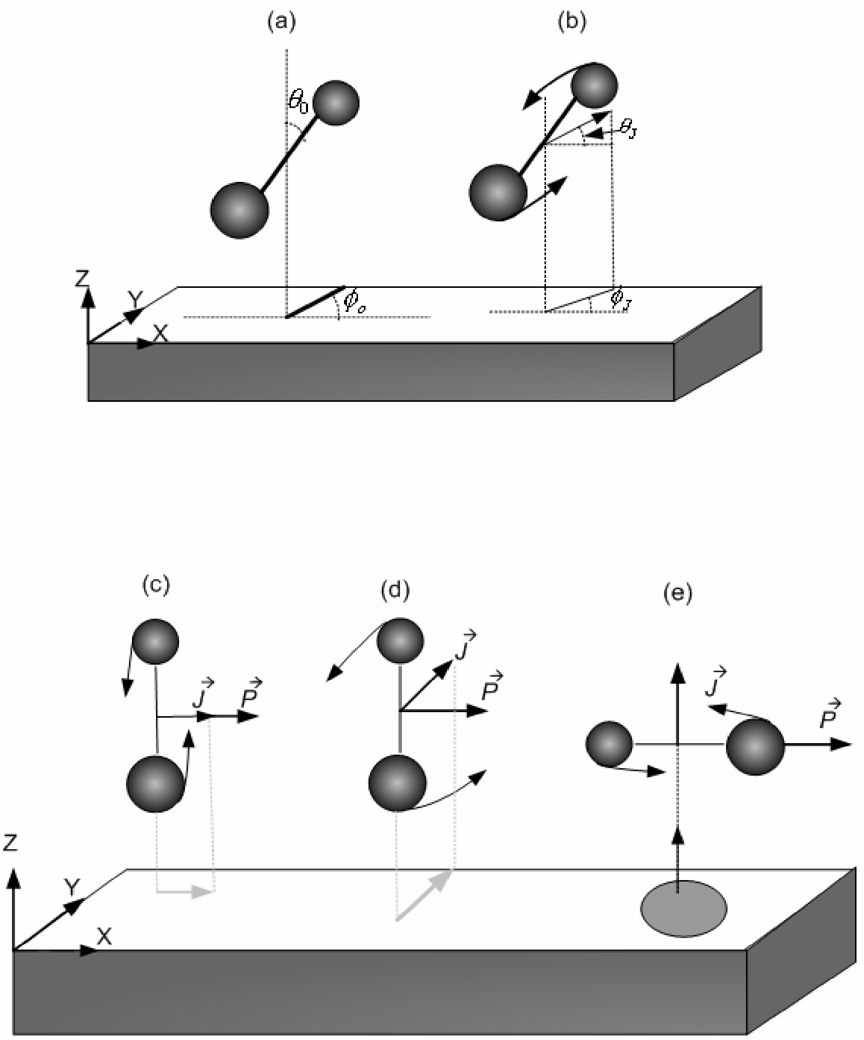

Figure 1: Illustration of the coordinate system used in this paper. (a) Orientation of the inter-nuclear axis. (b) Orientation of the rotational angular momentum. (c) Propeller-like rotation (θ_J =0° and ϕ_J=0°). (d) Cartwheel-like rotation (θ_J =0° and ϕ_J= ±90°). (e) Helicopter-like rotation (θ_J=90°). $\vec{P}$ and $\vec{J}$ are defined as the momentum and angular momentum, respectively.

incidence angle, θ_i (with respect to the surface plane) also increases. The resulting scattered particles are shown in figure 2(a)-(d) as a function of their energy loss.

Each of these distributions is based on the simulation of 30,000 trajectories of CF molecules. The molecules were scattered sequentially, with a randomly selected orientation of the molecular axis as outlined in the previous section. The changes observed in the scattered distribution with increasing normal incidence energy are a result of enhanced energy exchange with the surface.

For $E_{\perp}$=4 eV (less than the 5.7 eV bond energy of CF) no dissociation occurs as a result of the collision. The peak of the scattered CF distribution corresponds to an energy loss of 2.1 eV. The energy width at half-maximum of the distribution is ~2.5 eV. These values are remarkable low considering the presence of 1500 eV of parallel energy in the incident molecules. Clearly, at grazing incidence the parallel energy is not readily accessible, neither for excitation of the internal modes of the molecule nor for energy exchange with the surface.

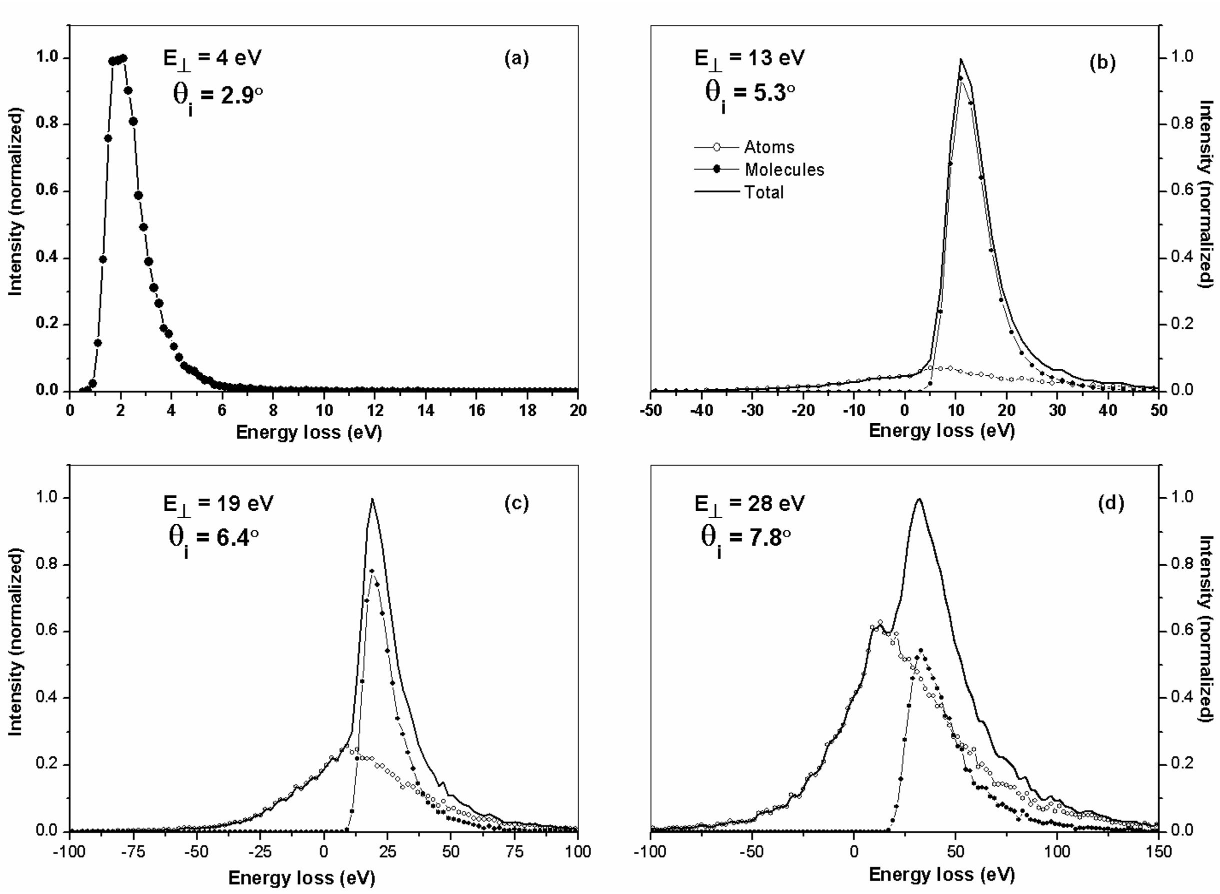

Figure 2: Energy loss of scattered particles (C and F atoms represented by open circles; surviving CF molecules represented by filled circles). $E_{//}$ =1500 eV and surface temperature of 300 K. (a) $E_\perp$ = 4 eV (b) $E_\perp$ = 13 eV (c) $E_\perp$ =19 eV (d) $E_\perp$ = 28 eV. The energy gain exhibited by some of the scattered atoms is a consequence of internal energy release in the CM frame when the molecule dissociates (see text for details).

For $E_\perp$= 13 eV dissociation becomes evident. As a consequence, the energy loss distribution of the scattered particles contains two parts: one due to scattered molecules, the other due to scattered atoms arising from dissociation. In addition to the overall distribution, the individual distributions of the scattered molecules and scattered atoms are indicated on figure 2(b). The overall distribution is dominated by the contribution from scattered molecules. The molecular distribution has a similar shape to that observed for $E_\perp$=4 eV, however the energy loss at maximum intensity is larger and the distribution is broader.

It is found that 13% of the incident molecules dissociate at $E_\perp$= 13 eV. The energy loss of the resulting atoms is determined by subtracting the final energy of a scattered atom from the proportion of the initial energy of the molecule that can be assigned to that atom on the basis of its mass. The energy loss distribution of the atoms is very broad and almost symmetric. Some atoms have a final energy that exceeds its initial energy (negative energy loss on the figure). This is a consequence of internal energy release upon dissociation (see details below). In contrast, all scattered molecules have energies lower than the initial energy.

Increasing the normal energy to 19 eV (shown in figure 2(c)) further increases the dissociation rate. At this energy, 35% of the incident molecules dissociate. The atomic component of the scattered distribution is now clearly evident. The shapes of both the atomic and molecular distributions are similar shape to the equivalent distributions observed at $E_\perp$=13 eV, but are much broader. In this case, the energy loss at the maximum of the molecular distribution (~22 eV) exceeds the initial normal energy. This indicates that as the normal energy is increased (less grazing incidence) the parallel energy becomes more accessible to the collision process. However, the total energy loss is still remarkably low compared to the amount of parallel energy in the molecule. When the normal energy is increased to 28 eV (shown in figure 2(d)), about 60% of the molecules dissociate. At this point the components due to scattered molecules and scattered atoms can be clearly distinguished. As before, the increased normal energy results in more energy loss (at maximum) and broader distributions. Note that the maxima of the atom distributions are consistently lower (in energy loss) than those of the corresponding molecule distributions. In the first instance, this is counter-intuitive: the molecules that dissociate (most internal energy uptake/hardest collision) exhibit less cumulative energy loss. Briefly, it is due to the number of interactions between the molecule and the surface atoms influencing both the total energy loss and the survival probability. This point will be addressed later.

The ability of some atoms to exceed their initial energy as a result of dissociation has been observed experimentally, for instance in the case of N_2 scattering from Pd(111) surface [6]. The effect is due to the release of excess internal energy gained during the collision (energy exceeding the bond strength) upon dissociation [26]. This excess energy is released in the molecule's center-of-mass (CM) frame. For a diatomic molecule, assuming the velocity change by the atoms is parallel to the (pre-dissociation) molecular trajectory, the resultant energy of the atoms, observed in the laboratory frame, can be obtained from the following Galilei transformation [27]:

$$E_{m1} = (m_1+m_2)^{-1}(m_1{*}E_0 + m_2{*}\varepsilon\pm2{*}(m_1.m_2E_0.\varepsilon)^{1/2}) \qquad (1)$$

E_0 is the kinetic energy of molecule before dissociation, m_1 and m_2 are the atomic masses, and ε is the internal energy released from the molecule in the CM frame. There are two solutions to equation 1. The larger value represents the atom that increases its velocity and thus gains energy in the laboratory frame after dissociation; the smaller value represents the other atom, which loses energy in the laboratory frame. Note that for every fragment that gains energy as a result of the dissociation, there is a corresponding fragment that loses energy (hence the broad and relatively symmetric distribution). To illustrate, figure 3 shows the maximum energy change anticipated for the atoms of a CF molecule with E_0=1513 eV as a function of the internal energy released (ε).

We are assuming that the C atom gains energy while the F atom loses energy in the measurement frame. For the purposes of this calculation, the energy released is assumed to already be in the molecule and thus is not extracted from E_0. After dissociation, an internal energy release of between 0-10 eV results in a maximum energy broadening of 0-230 eV for the fragments (difference between the observed energy gain by C and the observed energy loss by the corresponding F). This range is comparable with that of the simulated results shown figure 2. Note that the large energy spread exhibited by the atoms does not imply a large energy exchange with the surface. It is purely a consequence of the excess internal energy in the molecule.

The calculation shown in figure 3 represents the optimum case in which the translational momentum given to the atoms in the CM frame is along the CM momentum of the molecule prior to dissociation. Of course, experimentally there will, almost invariable, be a random distribution of the molecular orientation prior to dissociation. Since the velocity gained by the atoms as a result of internal energy release is independent of the trajectory of the molecule and can be perpendicular to it, the atoms exhibit a broader angular distribution as well as a broader energy distribution when compared to the surviving molecules. The inset on figure 3 shows a comparison between the polar angle distribution of the scattered molecules and scattered atoms. In both cases, the maximum intensity corresponds to the specular scattering

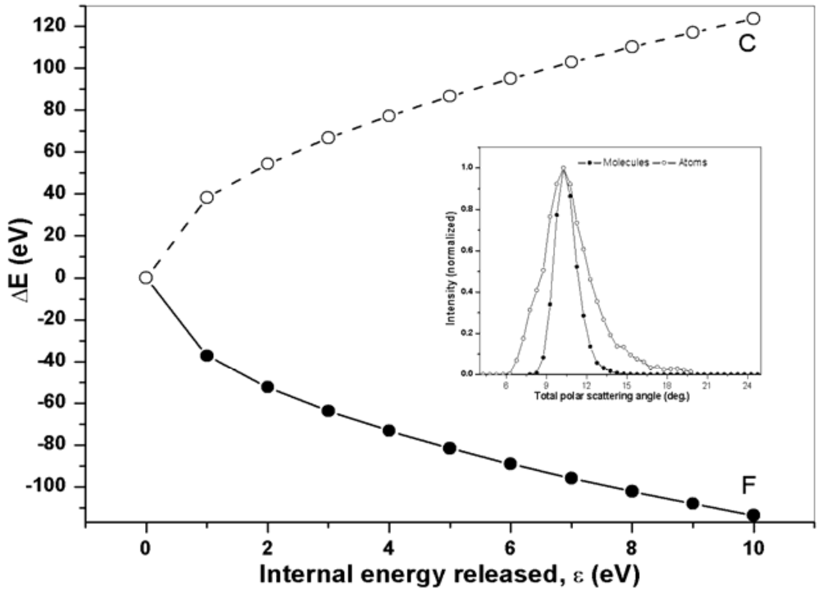

Figure 3: Maximum energy broadening of C and F fragments calculated from equation 1 (see text for details). Inset: polar scattering angle distribution of C and F atoms (open circles) and surviving CF molecules (filled circles). $E_{\perp}$=13 eV; $E_{//}$=1500

direction. However, the angular width of the scattered atoms is substantially broader than that of the molecules.

The energy loss observed and the degree of dissociation are a consequence of the transfer of translational energy from the molecule both to the surface atoms and to the molecule's internal degrees of freedom. Figure 4(a) shows the variation of the averaged internal energy uptake (left ordinate) and the averaged total translational energy loss (right ordinate) as a function of the initial normal energy for molecules that survive the collision. Calculated curves are shown for scattering from a surface at 0 K and at 300 K.

The general behavior observed at the two surface temperatures is the same. With increasing normal energy, more translational energy is lost by the molecules. The scaling with normal energy is not linear. At low normal energies the translational energy loss is less than the normal incidence energy, but this reverses as the normal energy increases (less grazing angles). Hence, the parallel energy becomes increasingly accessible as a function of the increasing angle of incidence. However, even at the largest angle studies the maximum translational energy loss observed represent only ~3.6% of the total initial energy. The translational energy loss at 300 K is consistently greater than that at 0 K. This can be attributed to an increase in the surface roughness, due to thermal displacement of atoms, allowing collisions with smaller impact parameters (harder collisions) to occur. The translational energy lost by the incident molecule is transferred both to the lattice atoms of the surface and to internal energy of the incident molecule. The plot of the internal energy uptake as a function of the normal energy shows an initial rapid increase for small $E_{\perp}$, followed by a more gradual increase at higher $E_{\perp}$. The limit of the internal energy uptake is dictated by the molecular bond strength. The internal energy uptake by the molecules is greater for the 300 K surface than for the 0 K surfaces, consistent with the larger translational energy loss observed at the higher temperature.

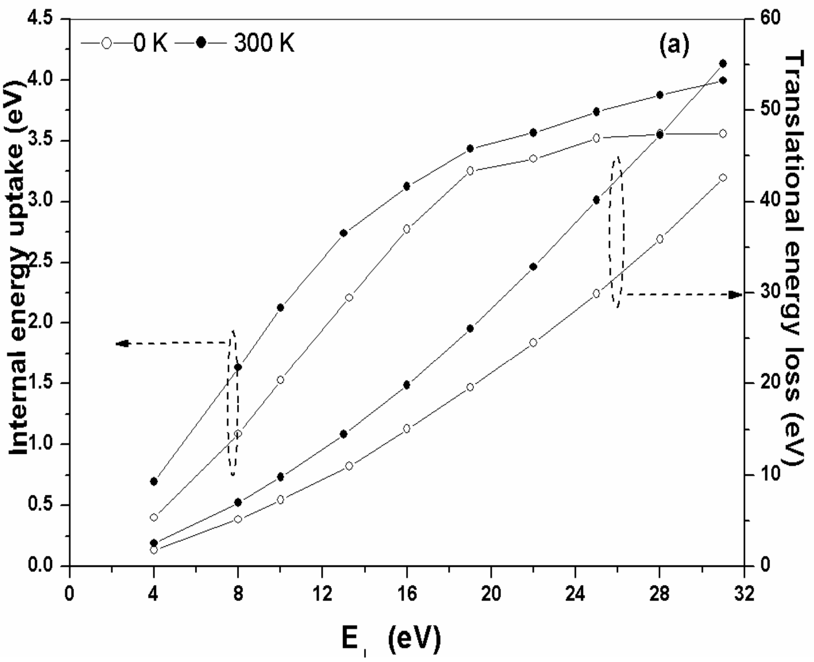

Figure 4(a): Average translational energy loss and average internal energy uptake as a function of $E_{\perp}$ for surviving CF.

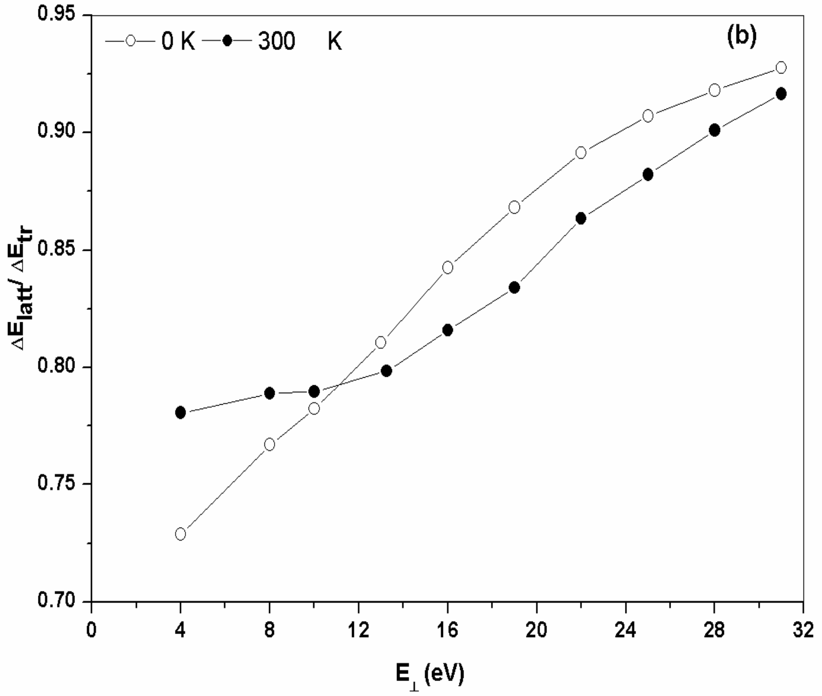

Figure 4(b): The fraction of the energy lost to the lattice atoms as a function of $E_{\perp}$ for surviving CF. Data shown for $E_{//}$ =1500 eV at surface

Figure 4(b) shows the fraction of the translational energy lost by the surviving molecules that is transferred to the lattice atoms as a function of the normal incidence energy at 0 K and at 300 K.

We note that the fraction transferred to the lattice atoms at 0 K varies from ~ 0.72 to ~0.92 as the normal incidence energy is increased from 4 eV to 31 eV. At 300 K the fraction varies form ~0.78 to ~0.93. Hence, in both cases, only a small fraction of the translational energy lost goes to the internal modes of the molecule. For relatively large normal incidence

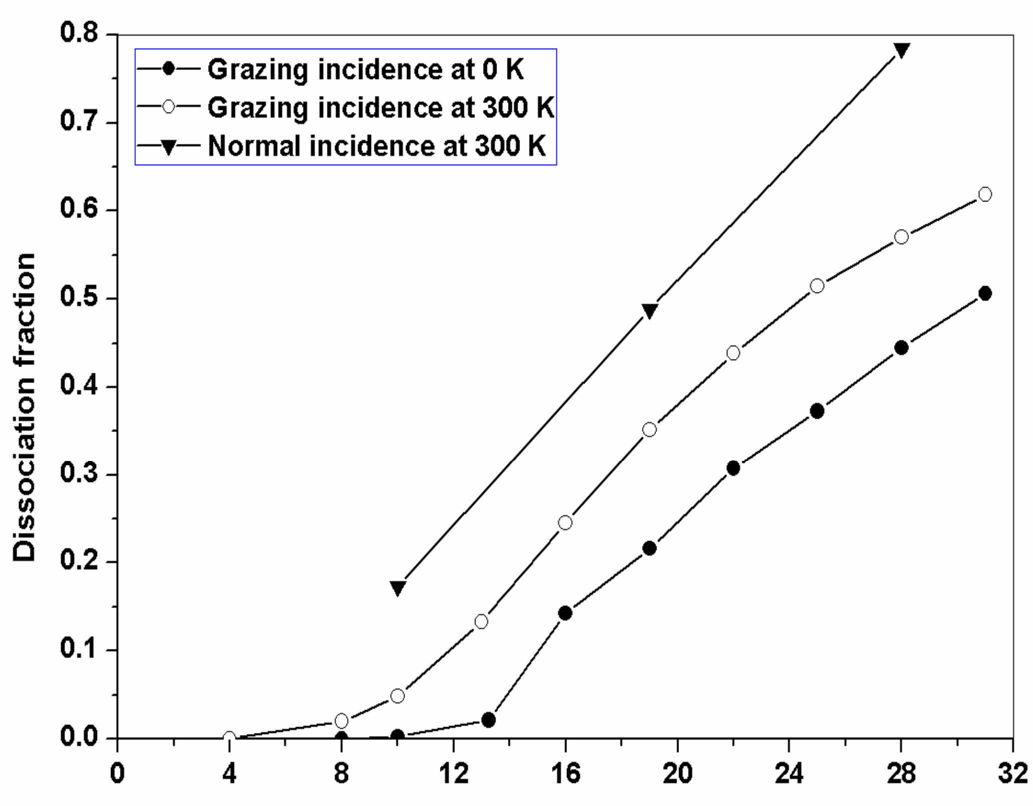

Figure 5: Dissociation fraction as a function of $E_{\perp}$ at surface temperatures of 0 K and 300 K for $E_{//}$ = 1500 eV; and at 300 K for $E_{//}$ = 0 eV.

energies ($E_{\perp}$ > 13 eV) the fraction transferred to the surface at 300 K follows the same trend as for 0 K. However, the absolute fraction is consistently lower for the room temperature surface, indicating a greater efficiency in the excitation of the molecule's internal modes compared to the 0 K surface. At more grazing incidence ($E_{\perp}$ < 13 eV), the fraction of translational energy that is transferred to the 300 K lattice becomes essentially constant at ~0.78. Hence, the redistribution of the translational energy between the surface atoms and the internal modes of the molecule has become independent of the normal energy/incidence angle in this region. A similar effect does not occur for the 0 K surface, indicating that it is a consequence of thermal motion of the surface atoms.

Molecules that gain internal energy (vibrational and/or rotational) as a result of a collision may subsequently dissociate [10]. Figure 5 shows the dissociation fraction of the scattered CF as a function of the normal incidence energy for the surface at 0 K and 300 K. At 0 K, there is a threshold for dissociation at $E_{\perp}$~12 eV, whereas for 300 K the threshold is at ~8 eV.

In both cases, the dissociation probability increases rapidly with increasing normal energy after the threshold. For a given normal energy, the dissociation fraction is consistently higher for the 300 K surface compared to the 0 K surface. This correlates with the larger translational energy loss and the larger internal energy uptake at 300 K observed in figure 4(a). Also shown on figure 5 are sample dissociation rates calculated for CF molecules incidence along the surface normal ($E_{//}$=0 eV) at 300 K. The data points show a similar trend to the grazing incidence data but are consistently higher. Thus, comparing molecules with different incident angles on the basis of their normal incidence energy is qualitatively valid, but not quantitatively reliable. The level of agreement between the grazing- and normal-incident molecules indicates that grazing incidence studies but utilized to gain information about low-energy molecular interaction with surfaces. Note that the total energy of the grazing-incident molecules is substantially greater than that of the normal incident molecules, but that the dissociation rate is lower. The dissociation rate is directly related to the 'final' internal energy of the molecules. The lower dissociation rate for grazing incidence scattering is a consequence of additional molecule-surface interactions that occur as a result of the efficient excitation of rotational motion (see later).

Gerber and co-workers have suggested that I_2 molecules scattering from rigid surfaces dissociate once the rotational energy exceeds the bond energy of the molecule [28; 29]. In the work by van den Hoek and Kleyn it was concluded that initial rotational excitation is converted to vibrational energy resulting in the dissociation of O_2 molecules scattered from a rigid surface at normal incidence [10]. In order to investigate the mechanisms operative in the scattering of CF scattering at grazing incidence from the Si surface, we compared the internal energy and the rotational energy of the surviving molecules both at the turning point and after the collision. The turning point is defined as the point where the normal velocity of the molecule's CM is zero - corresponding to the point of the closest approach to the surface. At the turning point all incident molecules are still intact. Hence, in order to ensure valid comparison, we select only the subset molecules that are found to ultimately survive the collision when comparing the situation at turning point with that after the collision.

5.3.2 Redistribution of internal energy.

The averaged total internal energy (E_{int}) and averaged rotational energy (E_{rot}) of CF, both at the turning point (TP) and after collision, are shown in figure 6(a) as a function of $E_{\perp}$. The difference between these two energies represents the vibrational energy. At the turning point, both the internal energy and the rotational energy increase in a linear fashion with increasing $E_{\perp}$ across the full range studied. After the collision, the internal and rotational energies also initially increase as a function of the normal incidence energy, but then begin to plateau at $E_{\perp}$ ~20 eV. Both the rotational energy and the internal energy at the turning point are always greater than the corresponding energies after the collision. The averaged rotational energy at the turning point for $E_{\perp}$=31 eV is 3.73 eV. This is still less than the bond strength of 5.7 eV. Note however that some individual molecules that ultimately survive the collision have rotational energies that exceed the bond strength at this point. After the collision, the averaged rotational energy has decreases to 1.39 eV. There is always a net loss of rotational energy after the turning point for the energy range studied. Figure 6(b) shows the fraction E_{rot}/E_{int} (ratio of rotational energy to total internal energy) for surviving molecules both at the turning point and after the collision as a function of their respective internal energies. In both cases, the rotational fraction decreases with increasing total internal energy. The initial decrease (for low internal energies) is relatively rapid, followed by a more gradual decrease at higher internal energies. It is clear from figure 6(b) that, for a given total internal energy, rotational excitation is always the dominant component when the molecules is at the turning point, as Gerber and coworkers concluded [11]. In contrast, after the collision the relative importance of rotational versus vibrational excitation shows significant variation depending on the total internal energy, with vibrational excitation being dominant as the dissociation limit is approached.

When considering the rotational fractions shown in figure 6(b), an important distinction must be made between the curve for molecules at the turning point and the curve for molecules after the collision. The curve at the turning point represents a snapshot of the molecules in a non steady-state condition. Energy exchange by translational energy loss to the internal modes and/or the surface and energy redistribution between the internal modes of the molecules are still on-going processes at this point. In contrast, the curve for the surviving molecules after the collision is for a steady-state condition. The shape of this curve is ultimately defined by the atomic potentials. An ensemble of scattered molecule that is

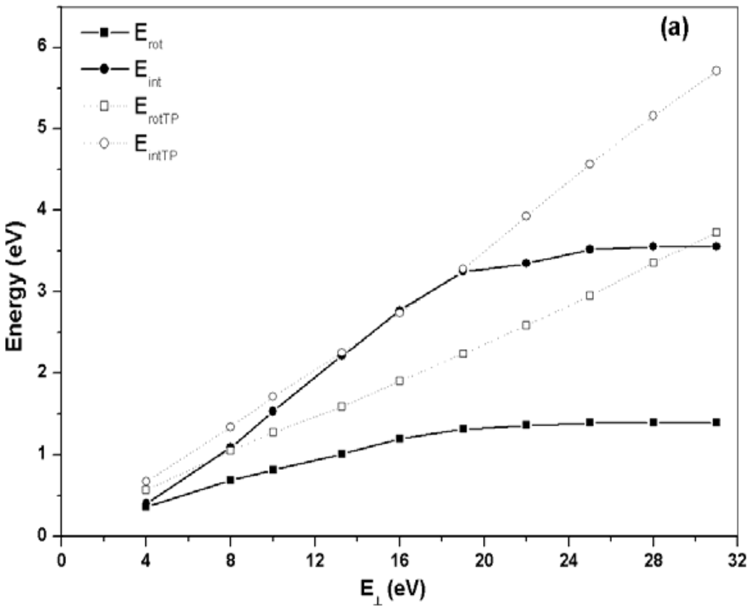

Figure 6(a): The internal and rotational energies at the turning point (open symbols) and after collision (filled symbols) as a function of the normal incidence energy for the surviving molecules.

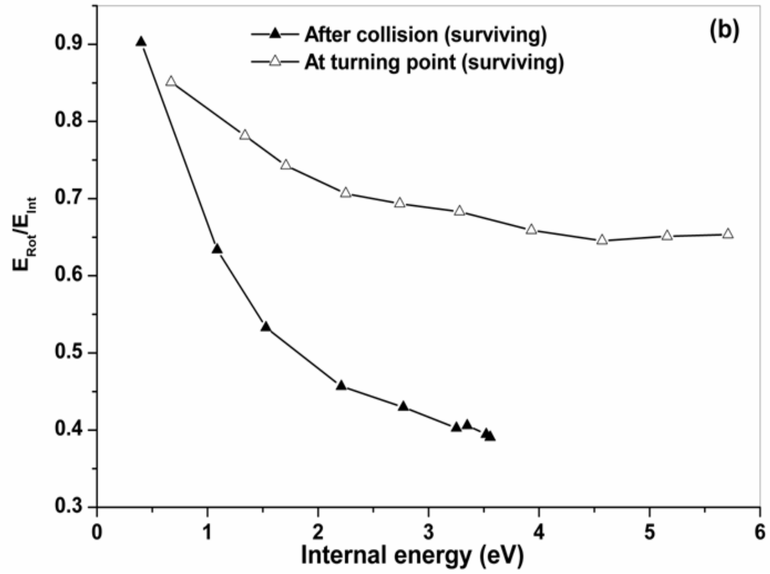

Figure 6(b): The rotational fraction at the turning point (open symbols) and after the collision (filled symbols) as a function of the internal energy for the surviving molecules. $E_{//}$=1500 eV and a surface temperature of 0 K

vibrationally and rotationally excited will distribute its total internal energy such that its rotational fraction will fall on the curve defined by the molecules after the collision shown on figure 6(b) (provided it is free of external influences). In this respect, the collision prior to the turning point with the surface serves only to provide the initial rotational and vibrational excitation and to determine the maximal internal energy of the molecule.

The molecules at the turning point can have an averaged internal energy that greatly exceed the bond strength because they are in a non-equilibrium state. In contrast, after the collision all surviving molecules have an internal energy less than the bond strength. This upper limit is the origin of the plateaus seen in figures 4 (a) and 6(a), and the bunching of the data points seen in figure 6(b) (each data point corresponds to a specific initial normal incident energy). For the energy range studied there is no indication of an upper limit to the transient internal energy that can be present in the molecule at the turning point, although such a limit should emerge for higher normal incidence energies. Comparing the rotational fraction of the surviving molecules at the turning point with that of the same molecules after the collision shows that in most cases the final rotational fraction is significantly lower. At the turning point, the rotational fraction of the internal energy in the surviving molecules is always more than 65%. At very grazing incidence, the fraction reaches more than 80%. In contrast, after the collision the rotational fraction is less than 50 % for molecules whose internal energy exceeds ~1.5 eV. It is clear from figure 6(b) that if the total internal energy is low (corresponding to the low normal incident energy data points), the rotational mode will be dominant, whereas the vibrational mode becomes more important as the total internal energy increases. Molecules at the turning point have a significantly higher rotational excitation than is observed for molecules in the steady-state with the same total internal energy.

In figure 7(a), the fractions E_{vib}/E_{vibTP}, E_{rot}/E_{rotTP} and E_{int}/E_{intTP} are presented, where E_{vib}, Erot and E_{int} denote the final averaged vibrational, rotational energy and total internal energies after the collision, respectively, and E_{vibTP}, E_{rotTP} and E_{intTP} represent the same energies at the turning point. The fraction E_{vib}/E_{rot} for molecules, both at the turning point and after the collision, is presented in figure 7(b). These ratios offer an insight into the redistribution of internal energy during the latter half of the scattering event. Considering the energy ratios shown in figure 7(a), any value greater than 1 represents a net gain in energy between the turning point and the final far field, while a value less than 1 represents a net loss. In the case of the total internal energy ratio, it initially increases with increasing normal incidence energy, reaches a maximum and subsequently decreases again. The maximum value, which occurs at normal incidence energy of 16 eV, is 1. At this point there is (on average) no net gain or loss of internal energy by the molecules as they travel from the turning point to the region in which the interaction with the surface ceases. It should be stressed that this does not necessarily mean that there is no energy exchange between the individual molecules and the surface, only that the net effect of all energy exchanges on the averaged total internal energy of the molecules is zero after the turning point. In all other cases, there is a net loss of internal energy to the surface.

We can see from figure 7(a) that the rotational ratio is less than 1 across the full range of normal incident energies, indicating that in all cases there is a net loss of rotational energy between the turning point and the end of the collision process. In contrast, the vibrational ratio is greater than 1 for most incidence energies indicating a net gain during the latter half of the collision. The notable exception is for the most grazing incidence trajectory ($E_{\perp}$ = 4 eV) where there is also a net loss of vibrational energy.

Figure 7(a) can be divided into two regions: one for normal incidence energies less that 16 eV and the other for normal incidence energies greater than 16 eV. When reducing the normal energy from 16 eV (moving to the left on fig 7(a)), the rotational ratio remains effectively constant as a function of the normal energy. In this region, the rotational energy is reduced by about 38% during the latter half of the collision, irrespective of the normal incidence energy. In contrast, the vibrational ratio decreases dramatically with decreasing normal energy, moving from a net gain at the higher values to a net loss for the lowest normal energy calculated. This drop in the relative importance of the vibrational mode is also evident in figure 7(b), where the ratio of vibrational to rotational energy after the collision drops dramatically as $E_{\perp}$ is decreased from 16 eV. In comparison, the change in this ratio at the

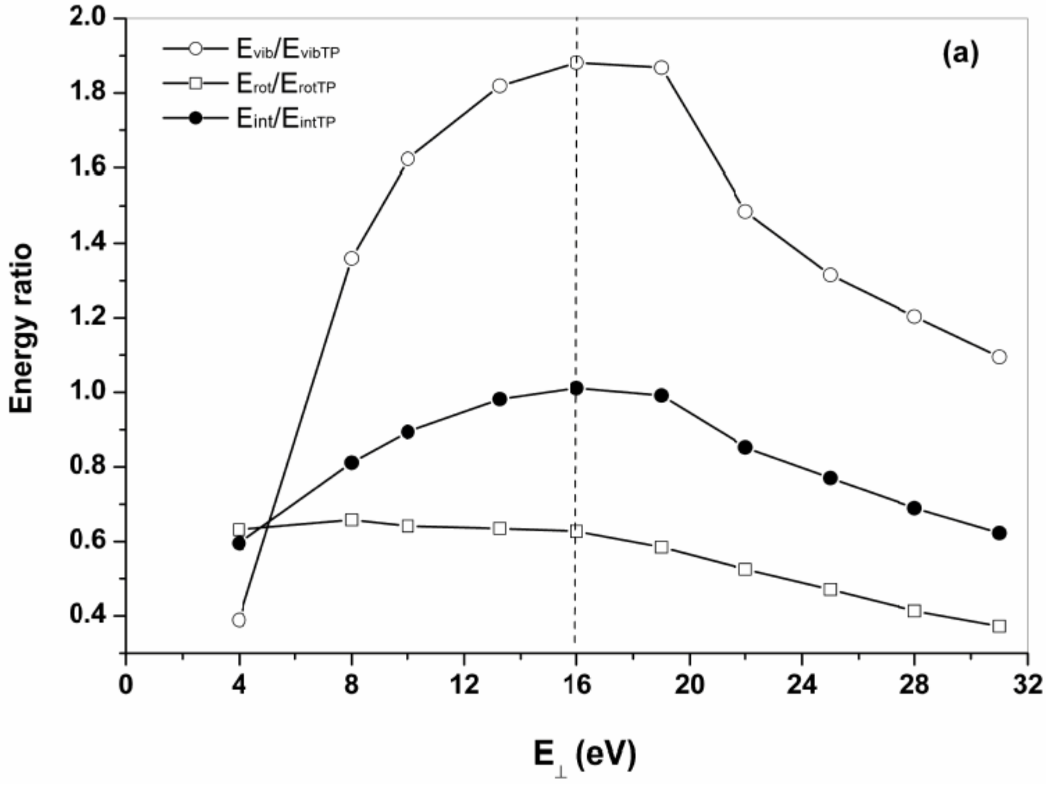

Figure 7(a): The fractions E_{rot}/E_{rotTP}, E_{vib}/E_{vibTP} and E_{int}/E_{intTP} as a function of the normal incidence energy for the surviving molecules. (b) The fraction E_{vib}/E_{rot}, as a function of the normal incidence energy at the turning point and after the collision for the surviving molecules. $E_{//}$=1500 eV and at a surface temperature of 0 K.

turning point as a function of $E_{\perp}$ is far less pronounced. The amount of vibrational excitation of the molecule at steady state is dependent on the total internal energy as shown in figure 6(b). With decreasing total internal energy, the fraction of the internal energy that can be accommodated in the vibrational mode decreases. To a lesser degree, the same is true of molecules at the turning point. As $E_{\perp}$ decreases, less of the rotational excitation gained at the turning point is converted to vibrational excitation at the steady state. For normal energies greater than 16 eV (moving to the right on fig. 7(a)) both the rotational fraction and the vibrational fraction decrease along with the decrease in the internal energy fraction. Figure 7(b) shows that the ratio of vibrational to rotational excitation in this region is independent of $E_{\perp}$ both at the turning point and after the collision. The absolute vibrational energy after the collision is greater than that at the turning point in this region ($E_{vib}/E_{vibTP} > 1.0$), even though the total internal energy of the molecules is decreasing (i.e. the molecules are still gaining vibrational energy between the turning point and the final equilibrium). In contrast, there is a net loss of rotational energy after the collision and the fraction lost increases with the normal incidence energy. The loss of rotational energy between the turning point and the steady state is a consistent feature across the full range of normal incidence energies. The gain in vibrational energy after the turning point can be attributed mainly to conversion from rotational excitation. This conversion occurs in competition with the loss of internal energy to the surface.

In order to illustrate the conversion dynamics between the rotational and vibrational modes after the turning point, we present their evolution for a single dissociating molecule (shown in figure 8(a)) and a single surviving molecule (shown in figure 8(b)).

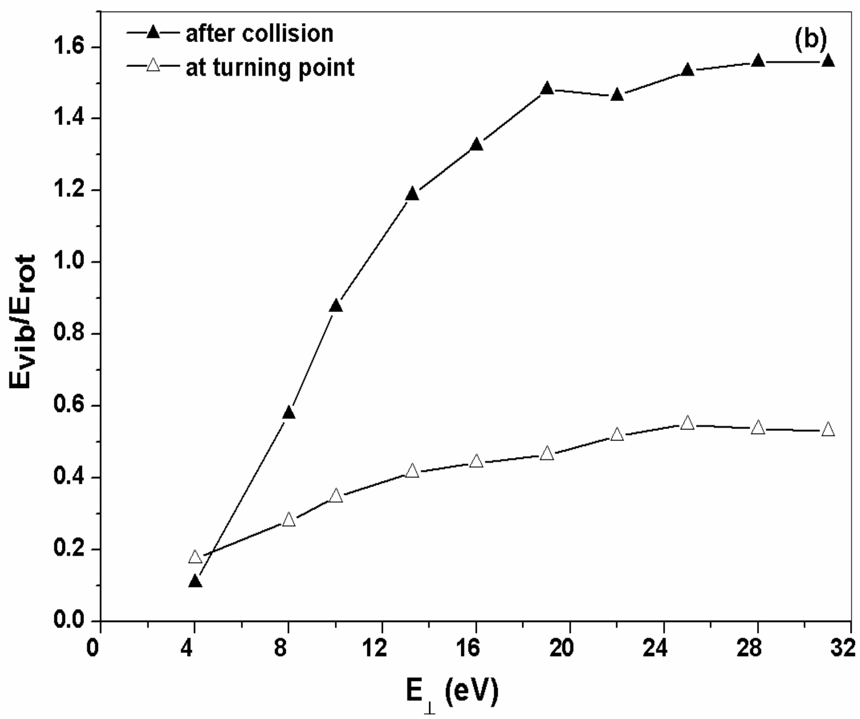

Figure 7(b): The fraction E_{vib}/E_{rot}, as a function of the normal incidence energy at the turning point and after the collision for the surviving molecules. $E_{//}$=1500 eV and at a surface temperature of 0 K.

The initial translational energy is 1531 eV ($E_{//}$= 1500 eV, $E_{\perp}$=31 eV). For the dissociating molecule, rotational excitation becomes evident at ~25 fs. At the turning point (33.5 fs), the rotational energy reaches a maximum value of 17.5 eV (more than three times the bond strength) and then decreases, while the vibrational energy increases continuously until dissociation. From the figure, we can determine that some of the initial rotational energy is transferred to vibrational excitation and some of it is transferred to the surface atoms. The energy exchange between the rotational motion and the surface atoms is evident from the oscillations that occur in the 35-60 fs region of the trajectory. Similar, but weaker, oscillations appear in the vibrational. Ultimately, dissociation results from the molecule gaining vibrational energy sufficient to overcome the bond strength. For the surviving molecule (figure 8(b)), there is simultaneous excitation of rotational and vibrational energies, although rotational excitation is the most dominant. At the turning point, the rotational energy reaches a maximum value of 11.5 eV (two times the bond strength). As before, after the turning point there is a large reduction in rotational energy and a corresponding increase in vibrational energy. Again, there are energy oscillations due to sequential interactions with the surface atoms. Ultimately, the molecule does not dissociate and after it has left the surface region there is a long-range oscillation of internal energy between the rotational and vibrational modes.

In order to highlight the role of the surface atoms in rotational energy transfer, identical trajectories are recalculated, but the interaction between the projectile and the surface atoms is removed once the turning point is reached. The results are shown in figure 8(c) for the dissociating molecule and figure 8(d) for the molecule that previously survived (but now also dissociates). By removing the interaction with surface atoms, we can clearly see that the rotational energy transfers completely to vibrational energy leading to dissociation. The decrease in the rotational energy after the turning point is slower in both figures 8(c) and (d) than it is in the corresponding curves in figures 8(a) and (b) and is completely smooth in the absence of a surface interaction. Hence, the redistribution of rotational energy is enhanced by

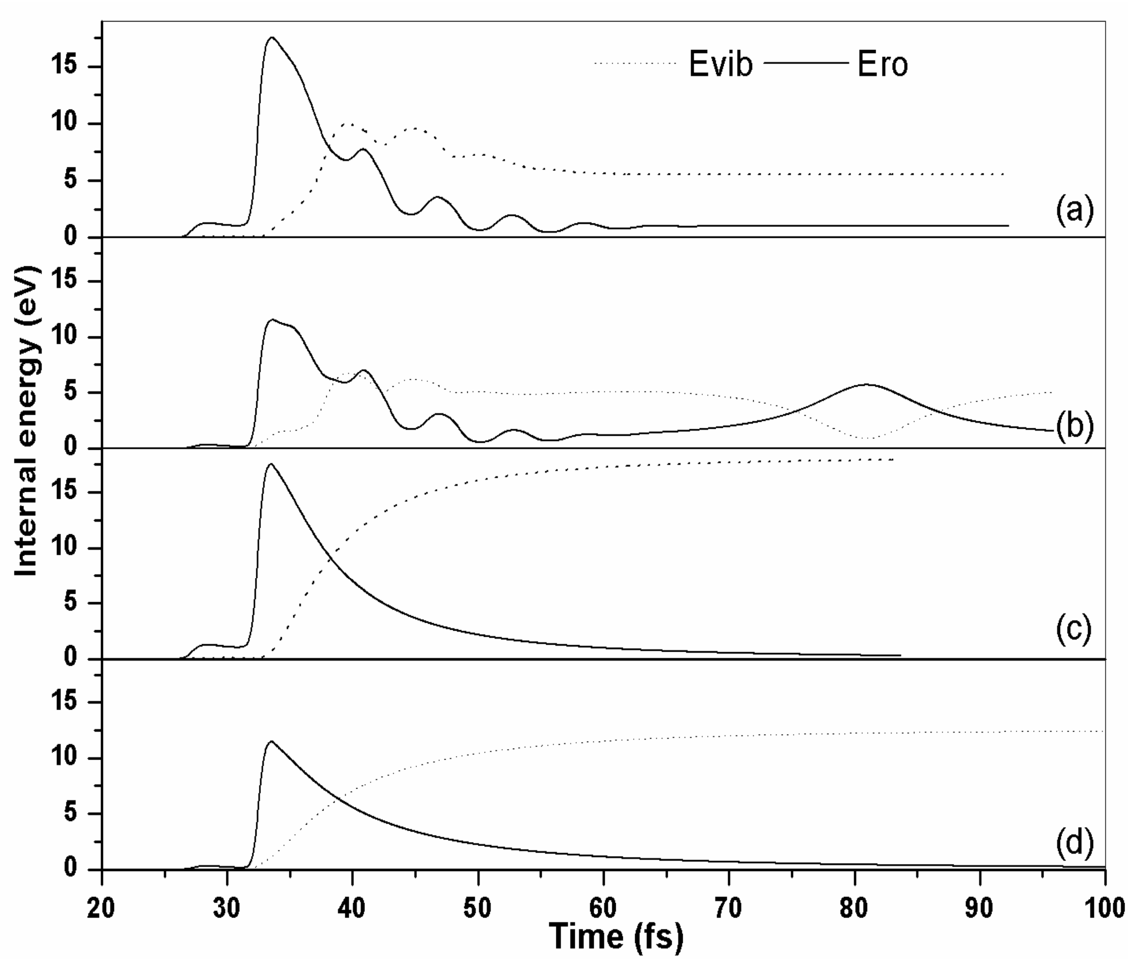

Figure 8: The evolution of the vibrational and the rotational energies for a dissociating molecule; (a) and a surviving molecule (b). After the removal of the surface interaction at the turning point, the evolution of the vibrational and the rotational energy for the same dissociating molecule (c) and the same "surviving" molecule (d).

the interaction with the surface atoms and it is clear that the oscillations in the rotational and vibrational energies seen on figure 8(a) and (b) result from interaction of the projectile with the surface atoms. By removing the surface interaction, the rotational energy, which is much larger than the bond strength at the turning point, remains in the molecule and results in dissociation. In both figure 8(c) and (d) the final "vibrational energy" is significantly higher than when the surface interaction is considered for the entirety of the collision. The main effect of the surface interactions after the turning point is to remove internal energy from the molecule, thus increasing the survival probability. Referring back to figure 2, the reason that the scattered atoms exhibit a smaller energy loss (at maximum) compared to the surviving molecules is now evident. The initial collisions of the molecules with the surface results in translational energy loss coupled with an internal energy uptake. However, after the initial strong excitation of the internal modes (primarily rotational), subsequent collisions allow for further translational energy loss coupled with a net loss of internal energy. Hence, molecules can lose more of their initial translational energy and simultaneously increase their survival probability. If there are few subsequent collisions, there is less loss of translational energy, but also less opportunity to reduce the initial large internal energy gain.

The behavior of CF differs from that of I_2 scattering from a flat surface [11], where I_2 molecules scattering from a flat surfaces dissociate if the rotational energy exceeds the bond strength. In the case of a corrugated surface (current simulation), molecule can temporarily gain rotation energy in excess of the bond strength and still ultimately remaining intact because some of the rotational energy gained can be transferred to the surface atoms. It is evident from the energy oscillations seen on figures 8 (a) and (b) that there are multiple interactions between the incident molecules and atoms of the surface. Rotational energy is removed as a result of the chattering type collisions [30], indicated by the rapid oscillations observed on figures 8 (a) and (b) for collision times between 35 and 60 fs. This is a natural consequence of the grazing angle of incidence utilized. The mechanism is similar to Ar scattering from Si (100) [5], where the trajectory of the projectile is gradually changed by a series of progressively harder interaction with the surface atoms, although the situation for molecular scattering is more complex. Following the classical turning point of CF (based on the CM of the molecule) over the trajectory gives a smooth trace with a single minimum at the point of closest approach to the surface. However, the individual atoms of the molecule invariably come closer to the surface than the CM. Efficient excitation of molecular rotation results in the individual atoms of the molecule experiencing several close interactions with the Si surface while the molecular CM is moving away from the turning point. Unlike Ar scattering, where the interaction potential between the projectile and the surface tends to be symmetric about the turning point, the interaction potential between CF and the surface is highly asymmetric about the classical turning point due to rotational excitation. The strongest interaction occurs around the turning point, but due to rotational and vibrational motion, a greater number of (weaker) interactions occur during the latter half of the collision. The overall picture arising from figures 6-8 is one where the incident molecules initially experience strong rotational excitation around the classical turning point. After this point two competing processes occur involving the transfer of rotational energy either to vibrational excitation or to the atoms of the surface. Some direct vibrational excitation occurs as a result of the collision with the surface but the main mechanism by which translational energy is converted to internal energy is rotationally mediated. Similarly, loss of internal energy to the surface during the latter half of the collision is mainly via rotational de-excitation.

5.3.3 Stereodynamics

For the simulations the initial polar and azimuthal orientations of the incoming molecules were selected randomly with a uniform distribution and the molecules had no initial rotational or vibrational excitation. All molecules that survive the collision have some degree of vibrational and rotational excitation. In order to characterize the stereodynamic motion of the surviving molecules, the distribution of the polar angle of the rotational angular momentum (θ_J), is shown in figure 9(a) for $E_{//} = 1.5$ keV, $E_{\perp} = 28$ eV at 0 K. Here, the polar angle is defined with respect to the surface plane as shown in figure 1. The distribution of polar angles, is peaked around $\theta_J = 0$, indicating that the rotational planes of the molecules are preferentially aligned with the surface normal. If these molecules rotate such that the plane of rotation is the same as the scattering plane, then the motion can be characterized as “cart-wheel”, whereas if the plane of rotation is perpendicular to the scattering plane (for θ_J=0°) the motion is “propeller”-like. The polar angle distribution shown in figure 9(a) has a minimum at θ_J=±90° indicating poor excitation of a “helicopter” like motion. In order to distinguish between cartwheel and propeller rotation of the scattered molecules, a contour diagram of the intensity distribution $I(\theta_J,\phi_J)$ is presented in figure 9(b). The azimuthal angle distribution (ϕ_J) is the angle of the projection of $\vec{J}$ onto the surface plane with respect to the initial incidence trajectory. Consequently, $\phi_J = 0°$ corresponds to the $\vec{J}$ projection being parallel to the initial trajectory along the surface (propeller-like motion) and $\phi_J = \pm 90°$ corresponds to the $\vec{J}$ projection being perpendicular to the initial trajectory (cartwheel-like motion). From the

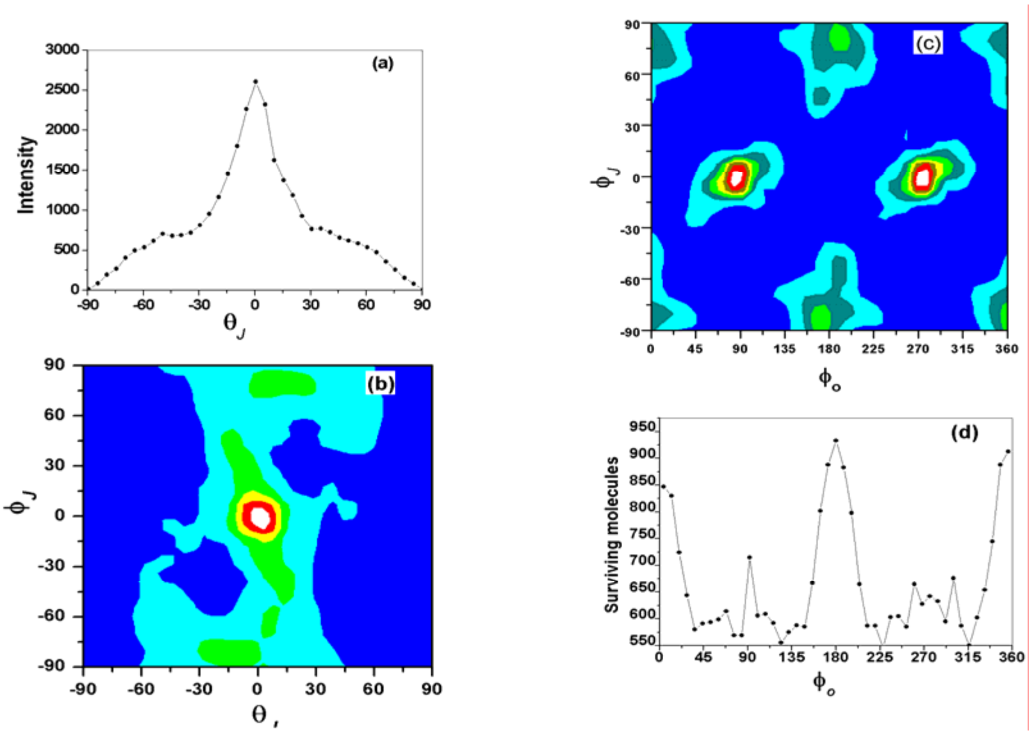

Figure 9: (a) The distribution of the polar angle of the rotational angular momentum (θ_J) of scattered CF molecules. **(b)** A contour diagram of the intensity distribution I(θ_J, ϕ_J) (ϕ_J represents the azimuthal angle of the rotational angular momentum). **(c)** A contour diagram of the intensity distribution I(θ_J, ϕ_o), where ϕ_o is the initial azimuthal orientation of the molecular axis. **(d)** The number of surviving molecules as a function of ϕ_o. $E_{//}$ = 1500 eV, $E_\perp$ = 28 eV at a surface temperature of 0 K.

contour diagram, two peaks are observed. The most intense peak is at θ_J =0° and ϕ_J = 0° corresponding to propeller-like motion. To our knowledge, this is the first prediction of propeller-like motion in molecular scattering from surfaces. A broader peak, located at θ_J =0° and ϕ_J = ±90°, is due to cartwheel-like motion. A contour diagram of the intensity distribution I(θJ,ϕo) is presented in figure 9(c) to illustrate the relationship between the initial azimuthal orientation of the molecular axis (ϕ_o) and the final motion of the surviving molecules. For molecules oriented parallel to the initial trajectory along [100] atomic rows (corresponding to 0°, 180° and 360° in the figure), the cartwheel-like motion is dominant. For molecules oriented perpendicular to the initial trajectory, the propeller-like motion is dominant. The number of surviving molecules as a function of the initial azimuthal orientation is shown in figure 9(d). Note that the maximum number of the surviving molecules is observed for the orientation that exhibits a cartwheel-like motion after scattering, while survival is significantly lower for orientation that yields a propeller-like rotation. However, the maximum intensity on the contour plots shown in figures 9(b) and (c) is due to the molecules with a propeller-like motion. The reason is that, although fewer molecules with a propeller-like motion survive the collision, those that do survive have a significantly narrower distribution of ϕ_J (better alignment with respect to each other). Figures 9(c) and (d) illustrate that the type of rotational motion observed is strongly dependent on the initial azimuthal orientation of the molecule, and that this also affects the survival probability. Similar analysis showed no dependence of the dissociation probability on the initial polar orientation of the molecules. It is clear that the molecular orientation with respect to the surface plays a role in the survival probability and the molecular motion. Consequently, we investigated whether the surface structure also influenced these properties. In Ar trajectory calculations under grazing

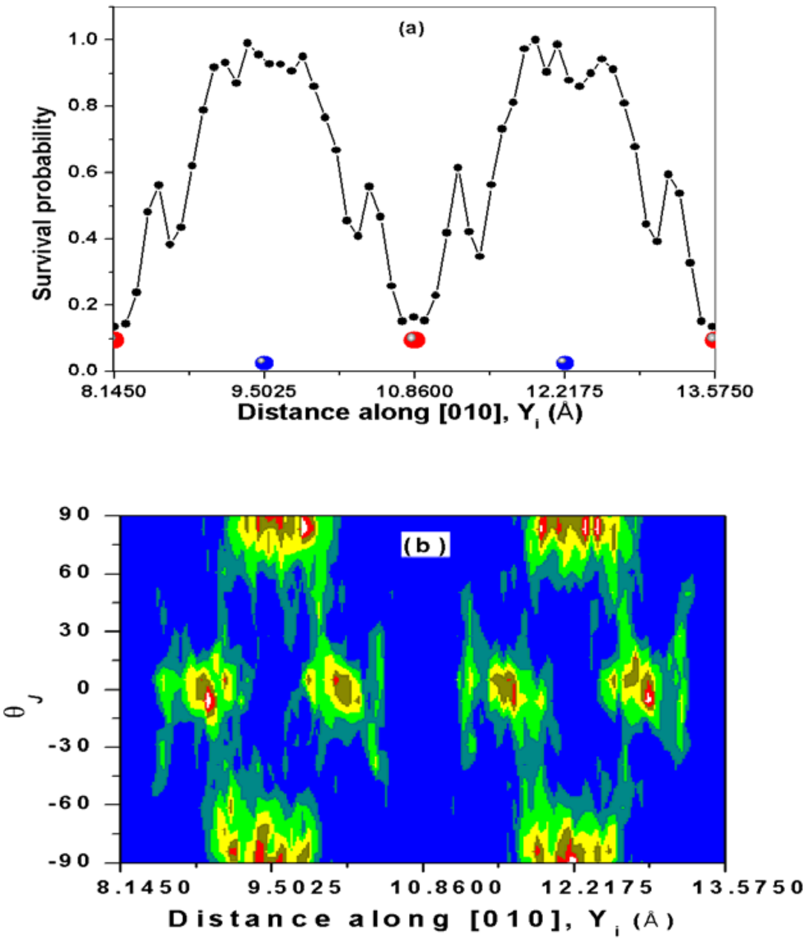

Figure 10: (a) Survival probability as a function of the initial Y component of the CM of the incident molecules (Y_I). **(b)** A contour diagram of the intensity distribution I(Y_i, ϕ_J). . $E_{//}$ = 1500 eV, $E_{\perp}$ = 28 eV at a surface temperature of 0 K.

incidence, it was found that the atoms undergo maximum translational energy loss when they impact just over the atomic rows of the first layer. Figure 10(a) shows the dependence of the survival probability on the initial Y-value of the CM of the molecules for $E_{//}$ = 1.5 keV, $E_{\perp}$ = 13 eV. The initial orientations of the incoming molecules are again chosen randomly with a uniform distribution. When the CM is aligned exactly with the atomic rows of first layer, the survival probability is less than 20%, consistent with the large energy loss observed for Ar scattering [5]. Molecules scattering from the first layer rows have the highest CM turning point. Such molecules have the lowest probability of further interaction with the surface atoms after the turning point and hence are less likely to be able to transfer internal energy back to the surface. When the CM is over the atomic rows of the second layer, almost no dissociation occurs. Comparing to the Ar scattering simulations, scattering from the second layer rows involves longer interaction times and weaker individual interactions with the surface atoms. This correlates with the higher survival probability observed for CF. Figure 10(b) shows a contour graph of the intensity distribution I(Y_i, θ_J). Here, Y_i denotes the initial CM component of the incident molecule. Due to the high dissociation probability of molecules with a CM aligned with the first layer atomic rows, there is a minimum in the contour plots at these points. From this figure, we can see that the cartwheel-type motion is dominant when the CM is aligned with the atomic rows of the second layer. These molecules are in effect scattering from the bottom of the ‘valley’ formed by the adjacent atomic rows of the surface atoms. The propeller-type motion is dominant when the CM is between the atomic rows of the first and the second layers. This can be characterized as scattering from the 'valley' walls created by the first-layer atomic rows. From figure 10(b) it is evident that the bulk of the molecules exhibiting propeller-like motion scatter from points nearer to the second layer atoms (i.e. nearer the bottom of the 'valley' wall). These effects will be analyzed in greater detail in a subsequent paper.

5.4 Conclusion

Redistribution of internal energy during molecule-surface interactions is a complex and angle dependent process. In particular, at grazing incidence angles the maximum internal energy uptake during the collision process can be substantially larger than the final internal energy once the interaction with the surface ceases. Around the point of closest approach to the surface, the internal energy gain by the molecules is at a maximum. At grazing incidence there is always strong rotational excitation at this point. After the turning point the internal energy gained is redistributed both between the internal modes of the molecule and between the molecule and the surface atoms. Some of the rotational energy is converted to vibrational energy while the loss of internal energy to the surface is mainly mediated via the rotational mode. The ability to lose internal energy to the surface allows some molecules to temporarily gain internal energy far larger than the bond strength and yet still ultimately survive the collision.

In the current study, all surviving molecules were rotationally excited with their planes of rotation preferentially aligned with the surface normal. Both cartwheel- and propeller-like motion is evident in the rotation of the scattered molecules. The type of rotational motion can be correlated with the initial molecular orientation and the local atomic structure of the surface. Molecules whose axis is aligned with the initial trajectory along the surface have a higher probability of surviving the collisions. These molecules tend to exhibit cartwheel-like motion. In contrast, molecules whose axis is perpendicular to the initial trajectory have a lower survival probability and tend to exhibit propeller-like motion. Excitation of cartwheel like motion occurs predominantly from the bottom of channels formed by the first layer atomic rows, while propeller-like motion arises from collisions with the sides of these channels. Molecules with predominantly a propeller-like motion exhibit a significantly better alignment of their rotational planes (narrow $<\vec{J}>$ distribution) when compared with molecules with a pre-dominantly cartwheel-like motion.

The degree of dissociation as a function of $E_{\perp}$ is comparable for $E_{//}$=1500 eV and $E_{//}$=0 eV (normal incidence). This clearly indicates that experiments at grazing incidence provide valuable details of dissociation dynamics and allow validation of computer models. The knowledge obtained can be used for better understanding of processes, such as plasma etching, in which this large parallel velocity is absent.

References

[1] J. P. Chang, J. W. Coburn, J. Vac. Sci. Technol. A 21 (2003) S145.
[2] G. R. Darling, S. Holloway, Rep. Prog. Phys. 58 (1995) 1595.

[3] W. Heiland, U. Imke, S. Schubert, K. J. Snowdon, Nucl. Instrum. Meth. B 27 (1987) 167.
[4] A. W. Kleyn, J. Phys.-Condens. Mat. 4 (1992) 8375.
[5] F. Gou, M. A. Gleeson, J. Villette, A. W. Kleyn, Nucl. Instrum. Meth. B 247 (2006) 244.
[6] T. Schlatholter, T. Schlatholter, M. Vicanek, W. Heiland, J. Chem. Phys. 106 (1997) 4723.
[7] P. J. Van den Hoek, T. C. M. Horn, A. W. Kleyn, Surf. Sci. 198 (1988) L335.
[8] P. H. F. Reijnen, P. J. Van den Hoek, A. W. Kleyn, U. Imke, K. J. Snowdon, Surf. Sci. 221 (1989) 427.
[9] H. Winter, Phys. Rep. 367 (2002) 387.
[10] P. J. Van den Hoek, A. W. Kleyn, J. Chem. Phys. 91 (1989) 4318.
[11] R. B. Gerber, A. Amirav, J. Phys. Chem. 90 (1986) 4483.
[12] J. S. Martin, B. T. Feranchak, J. R. Morris, J. N. Greeley, D. C. Jacobs, J. Phys. Chem. 100 (1996) 1689.
[13] J. C. Polanyi, R. J. Wolf, Ber. Bunsenges. Phys. Chem. 86 (1982) 356.
[14] W. R. Koppers, J. H. M. Beijersbergen, K. Tsumori, T. L. Weeding, P. G. Kistemaker, A. W. Kleyn, Phys. Rev. B 53 (1996) 11207.
[15] W. R. Koppers, K. Tsumori, J. H. M. Beijersbergen, T. L. Weeding, P. G. Kistemaker, A. W. Kleyn, Int. J. Mass. Spectrom. 174 (1998) 11.
[16] W. R. Koppers, M. A. Gleeson, J. Lourenco, T. L. Weeding, J. Los, A. W. Kleyn, J. Chem. Phys. 110 (1999) 2588.
[17] W. R. Koppers, J. H. M. Beijersbergen, T. L. Weeding, P. G. Kistemaker, A. W. Kleyn, J. Chem. Phys. 107 (1997) 10736.
[18] M. P. Allen, D. J. Tildesley, Computer Simulation of Liquids, New York, Oxford Science Publications, 1987.
[19] J. Tanaka, C. F. Abrams, D. B. Graves, J. Vac. Sci. Technol. A 18 (2000) 938.
[20] G. Molière, Z. Naturforsch 2a (1947) 133.
[21] R. J. W. E. Lahaye, A. W. Kleyn, S. Stolte, S. Holloway, Surf. Sci. 338 (1995) 169.
[22] P. M. Morse, E. C. G. Stueckelberg, Physical Review 33 (1929) 932.
[23] J. Tersoff, Phys. Rev. Lett. 61 (1988) 2879.
[24] J. Tersoff, Phys. Rev. B 38 (1988) 9902.
[25] J. Tersoff, Phys. Rev. B 39 (1989) 5566.
[26] K. Bruning, W. Heiland, T. Schlatholter, I. A. Wojciechowski, M. B. Medvedeva, V. K. Ferleger, J. Chem. Phys. 113 (2000) 2456.
[27] J. R. Peterson, Y. K. Bae, Phys. Rev. A 30 (1984) 2807.
[28] R. Elber, R. B. Gerber, J. Chem. Phys. 79 (1983) 4087.
[29] R. B. Gerber, L. H. Beard, D. J. Kouri, J. Chem. Phys. 74 (1981) 4709.
[30] J. N. Greeley, J. S. Martin, J. R. Morris, D. C. Jacobs, J. Chem. Phys. 102 (1995) 4996.

Chapter 6

CF interaction with Si (100)-(2x1): Molecular Dynamics Simulation

Abstract: In this study, the interaction of CF with the clean Si (100)-(2x1) surface at normal incidence and room temperature was investigated using molecular dynamics simulation. Incident energies of 2, 12 and 50 eV were simulated. C atoms, arising from dissociation, preferentially react with Si to form Si-C bonds. A $Si_xC_yF_z$ interfacial layer is formed, but no etching is observed. The interfacial layer thickness increases with increasing incident energy, mainly through enhanced penetration of the silicon lattice. Silicon carbide and fluorosilyl species are formed at 50 eV, which is in good agreement with available experimental data. The level of agreement between the simulated and experimental results is discussed.

6.1 Introduction

Fluorocarbon plasma dry-etch processing techniques are widely used in the fabrication of silicon-based integrated circuits, display and related applications such as micro-electromechanical system (MEMS) [1; 2]. The ability to better control the processes and improve capabilities depends on a better quantitative understanding of the plasma-surface interaction. However, etching consists of many chemical and physical processes at surfaces and thus the precise mechanisms are still poorly understood. In order to establish and quantitatively describe surface-interaction mechanisms in the plasma environments, many measurement techniques have been utilized. For incident and outgoing flux analysis, optical techniques (such as the imaging of radicals interacting with surface (IRIS) [3; 4]) and mass spectrometry [5] have been utilized. For etching surfaces, general surface analytical tools have been used to characterize the plasma-treated surfaces (for example, X-ray photoelectron spectroscopy (XPS) [6], Auger electron spectroscopy (AES) [7; 8]). In addition, real-time measurement techniques have been implemented in recent years (for example, ellipsometry [9], Fourier-transform infrared spectroscopy [10] and low energy ion scattering at grazing incidence [11]).

Ions play an important role in fluorocarbon plasma processes. Many experiments involving mass- and energy-selected beams interacting with surfaces have been carried out in an attempt to understand the dynamics of plasma-surface interactions [12-14]. Koppers et al. have studied the dissociation mechanisms of CF_3^+ interacting with a variety of surfaces [15;

16]. The work by Coburn shows CF_3^+ bombardment of etched surfaces enhances the etching rate of neutral species [17]. Experimental results for CF^+ bombarding a silicon surface by Chang et al show how the interfacial composition changes with the incident energy [18]. However, the complex and highly coupled nature of plasma-surface interactions makes direct observation of microscopic physical and chemical processes occurring at surfaces experimentally challenging.

Atomic-scale simulation methods have been widely recognized as an efficient tool to investigate the dynamic processes occurring during plasma-surface interaction. Molecular dynamics (MD) simulations have been successfully used to study fluorocarbon-silicon interactions [19-25]. In the group of Graves, a Tersoff-form potential parameterized for a system including C, F and Si has been used to simulate CF_x (x=0-3) deposition and etching on amorphous silicon surfaces [26-28]. Their simulations show that a $Si_xC_yF_z$ interfacial layer was formed on the surface after bombardment and that the thickness was dependent on the incident energy. However, they pointed out that their simulated results [28] were not consistent with the experiments performed on HF-treated Si(100) by Chang et al. Using XPS measurements, Chang et al. [18] concluded that very few fluorocarbon species were present on the surface at 100 eV, while Abrams and Graves predicted a fluorocarbon layer atop the mixed $Si_xC_yF_z$ interfacial layer. There were a number of practical differences between the experiments and the simulations. Chang et al used a single-crystal Si(100) which was hydrogen passivated [18; 29]. No in-vacuum clean was applied and so the un-exposed sample surface contained hydro-carbon contaminants. The previous simulations were performed on bare amorphous Si surfaces [26]. The simulations were performed for exposure up to 4 time longer that the experimental measurements. Additionally, Chang et al investigated bombardment of Si(100) at 2, 10, 20 and 100 eV, while the simulations of Abrams and Graves were performed for 50, 100 and 200 eV incident energies.

In the current simulations we utilize a crystalline sample with a bare Si (100)-(2x1) surface and performed MD simulations of CF interacting with it at incidence energies of 2, 12 and 50 eV. Exposures of 10 ML (comparable to the experimental conditions) are simulated, focusing on the surface chemistry such as bond breaking and formation. The current simulations use an improved form of the Si-F potential compared to the previous measurements [21]. We seek to provide a detailed picture of how the process of adlayer formation changes as the incident energy is increased. The reasons for the discrepancies between experimental and theoretical results are discussed.

6.2 Computational details

Classical molecular dynamics are used to simulate the interaction of CF with the Si (100)-(2x1) surface. We utilize a code developed by Abrams and Graves [26]. Details of the MD method used can be found elsewhere [30], but we briefly describe the procedure here. Molecular dynamics simulations calculate the time-dependent positions and velocities of a system of atoms by numerically integrating Newton’s equation of motion. The net force exerted on each atom is calculated from the gradient of an inter-atomic potential energy function.

The reactive empirical bond order (REBO) potential, developed by Brenner [31] has been extensively utilized to evaluate the dynamic effects of hydrocarbons on surface. This is a many-body potential, classical and empirically derived by fitting to data from experiments and *ab initio* calculations. The REBO potential allows for bond breaking and new bond formation over the course of a simulation. The original REBO potential for hydrocarbons has been extended to include F, Si and C by Tanaka et al [32]. We utilized this potential, incorporating the improved Si-F potential of Humbird and Graves [21], to describe the C-F-Si system. In order to overcome the deficiency of the Tersoff formalism in the repulsive potential at very close separation distances, a Molière-type repulsive screened Coloumb potential for all pairwise interactions is introduced. More details about this potential can be found in references [21; 32].

An unreconstructed crystal consisting of 3x3x4 Si (100) unit cells with a lateral area of about 300 $Å^2$ and a depth of about 20 Å was created. The simulation cell had periodic boundaries in the x and y directions. In order to obtain a well-ordered reconstructed surface, the atoms of the unreconstructed surface were displaced and dimerized and the resulting crystal was equilibrated using MD at 300 K to obtain a relaxed Si (100)-(2x1) surface. The Si potential can automatically generate dimer pairs without requiring manual displacement of the surface atoms. However, this does not result in the formation of perfect dimer rows. Manually displacing the atoms ensured that an ‘ideal’ 2x1 reconstruction was formed. In order to check that the sample used was sufficiently large to accurately describe the interaction process at 50 eV, the results were compared with test simulations done on a larger 4x4x6 sample (surface area ~500 $Å^{-2}$; a similar sample size has been previously used for energies up to 200 eV [26; 28]). No significant differences were found between the results produced by the two different sample sizes.

CF molecules with the appropriate kinetic energy were directed at the surface in a sequential fashion. On the basis of the sample size, 18 impacts was equivalent to a 1 ML exposure. The initial vibrational and rotational energies of the molecules are zero and in the simulations molecules are treated classically. At the beginning of each impact, the CF molecule was equilibrated at 300 K. The vertical position above the surface was set so that it was just beyond the range of the surface interaction potential (the potential between them was $<10^{-6}$ eV). The initial horizontal position(x, y) of the molecule was selected randomly within the simulation cell. The initial orientation of CF molecules was also selected randomly. The incident angle was always normal to the surface, consistent with the experimental condition of Chang et al [18]. The velocity-Verlet method with a time step of 0.5 fs was used for integration of the equation of motion for a total of 0.4 ps [33]. Increasing the integration time had no obvious effect on the simulated results. In the simulation, the crystal atoms are divided into two different types. The bottom two layers are held rigid in order to maintain the structure. The other layers are set to be thermostat atoms. Thermostat atoms dissipate the extra energy resulting from bombardment and thus maintain the system temperature at close to 300 K. The Berendsen heat bath with a coupling time of 0.01 ps was employed for temperature control [34]. Similar to the methodology used in [28], in our simulations the Berendsen scheme was applied for all atoms that were not the incident CF molecule or fixed Si atoms over the entire trajectory. After integration, atoms and molecules that were not bound to the surface were removed from the configuration and a new CF molecule was directed at the modified surface. Since we rescale the temperature during the entire trajectory, no time between impacts is considered. In the simulations by Abrams and Graves, it was found that relaxation of bombarded samples for 10 ps produced no significant changes in the deposited layers [28].

6.3 Result

Continuous bombardment by energetic CF molecules results in surface modification. Snapshots of the modified surface are shown in figure 1 after 180 impacts by 2 eV and 50 eV molecules. As can be determined from the figure, after bombardment with 2 eV CF molecules silicon carbide and fluorocarbon species are present on the modified surface. These species

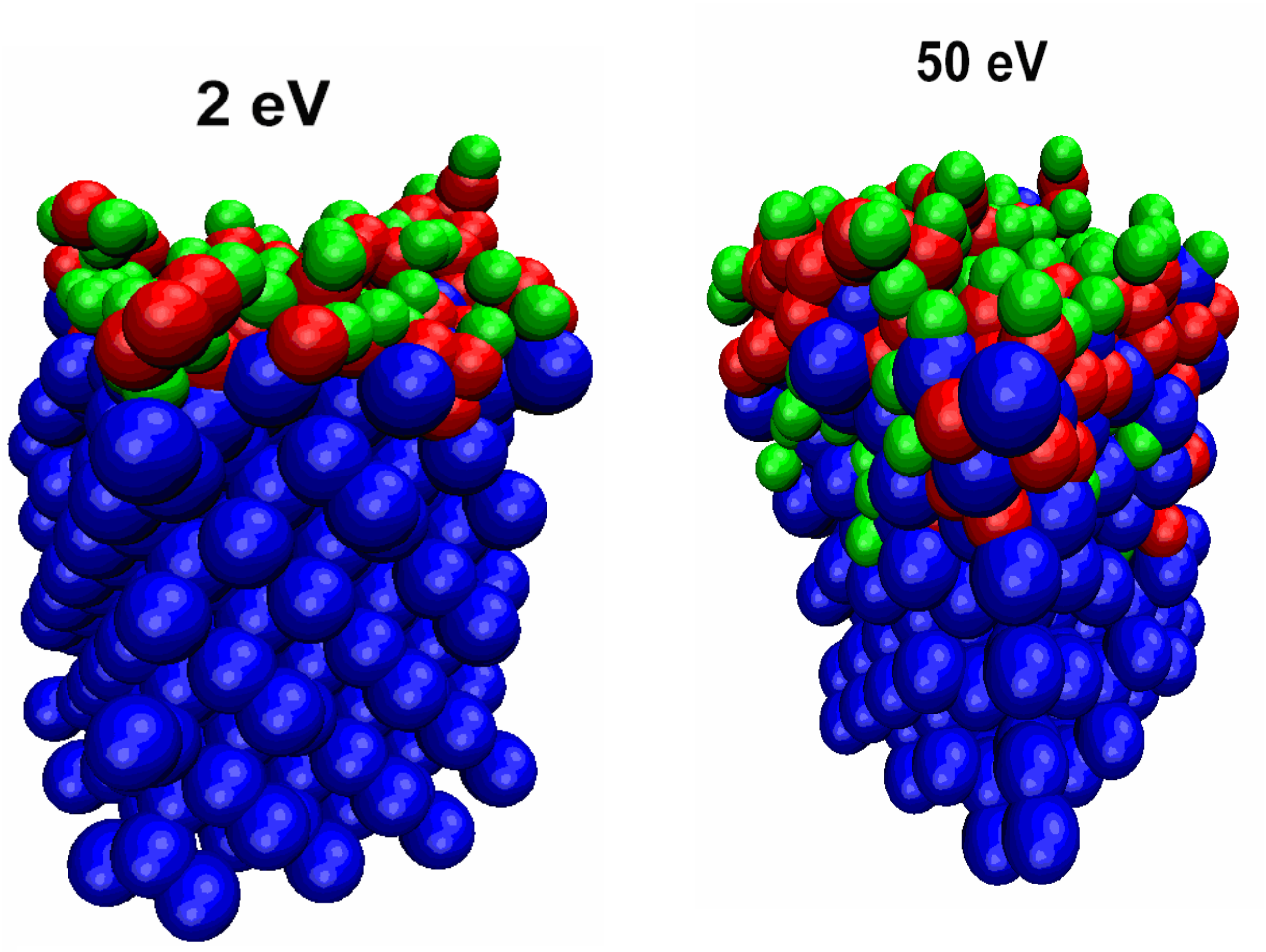

Figure 1: Snapshots of the modified surface after 180 impacts by 2 and 50 eV CF molecules. Blue represents Si; Red represents C; Green represents F.

are concentrated at the top of the sample. Fluoro-carbon chains are observed, but no obvious fluorosilyl species are evident. After bombarding with 50 eV CF molecules, silicon carbide, fluorocarbon and fluorosilyl species are present on the modified surface. We also note that some C and F atoms penetrate into the bulk and react with silicon atoms beneath the surface layer. A thicker SiCF-containing interfacial layer is created in the 50 eV case compared to the 2 eV case.

To characterize the structure of the modified surface, depth profiles of the F, C and Si and the total atomic densities are presented in figure 2 for surfaces bombarded with 2, 12 and 50 eV CF. From the profiles, we note that the modified surface depth (the interfacial layer) is strongly dependent on the incident energy. All three energies result in layer growth beyond the position of the original Si surface. The extent of this growth is not very energy dependent, although there is somewhat more growth at lower incident energies. With increasing incident energy, the atomic density in the vicinity of the original surface increases; C and F atoms penetrate deeper into the crystal; and more silicon atoms are displaced resulting in a broader interfacial layer. At 2 eV, CF molecules have insufficient energy to penetrate the crystal and are mainly absorbed on the surface. Subsequent CF molecules can only be incorporated into the growing layer or reflected from the surface. Consequently, the interfacial layer remains thin with a depth of about 2 monolayers. In this layer, the C and F distributions as a function of depth are almost identical.

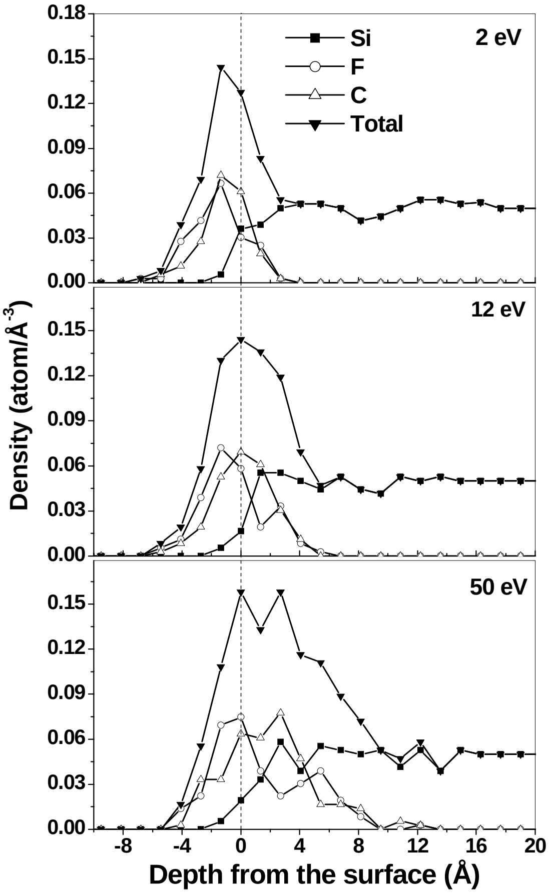

Figure 2: The depth profiles of F, C and Si atoms and the total density profiles for surfaces bombarded with 2, 12 and 50 eV CF. In each case, a total of 180 impacts were used.

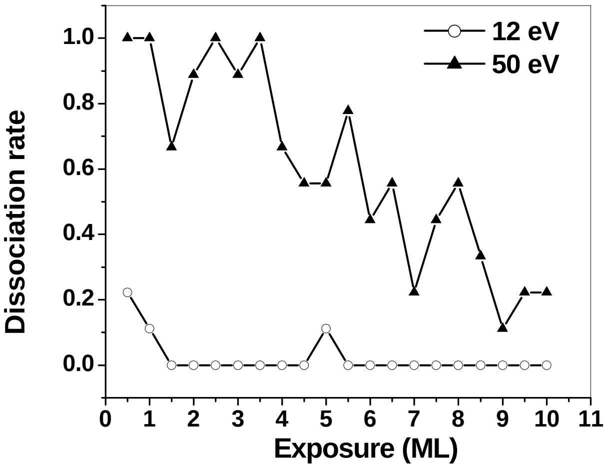

Figure 3: The dissociation rate as a function of exposure for 12 eV and 50 eV bombardment. The rate is calculated from successive groups of 9 incident CF molecules, each representing an exposure equivalent to 0.5 ML

At 12 eV, penetration of the lattice structure becomes possible. A thicker interfacial layer is formed and the distributions of C and F start to differ. At 50 eV, the interfacial layer becomes even broader. The number of fluorine atoms exceeds the number of carbon atoms

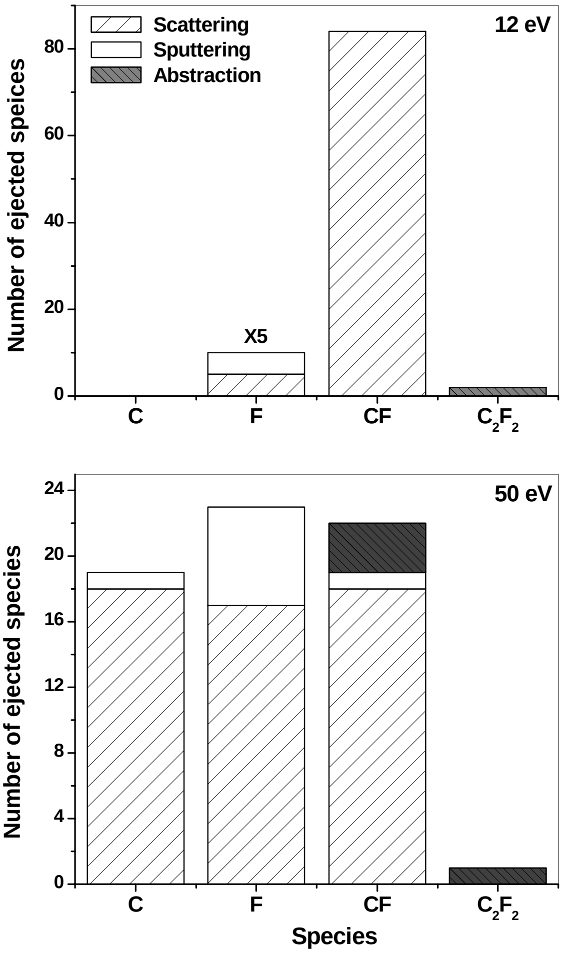

Figure 4: The cumulative yield of gas phase species that are ejected from the surface for 2, 12 and 50 eV after 10 ML exposure.

near the surface and an F-rich surface layer is formed. This is somewhat counter-intuitive since the energy carried by the individual atoms of the molecule is equal to the respective mass fraction (neglecting any internal energy stored in the molecule). Hence, the energy carried by the F atom (61%) is greater than that of the C atom (39%) and F atoms are in principle capable of penetrating deeper into the bulk. There is some indication of a two component structure in the F distribution at 12 and 50 eV incident energies.

Upon impact with the surface, the incident molecule transfers its energy to atoms near the surface and to its own internal degrees of freedom. At 2 eV the available energy is much less the C-F bond energy (5.7 eV). Hence no dissociation occurs but internal energy is gained by the molecule. The calculation demonstrates that all the incident CF molecules remain intact and either scatter away without reacting (~60%) or absorb on the surface (~40%). The molecules that scatter away lose about 80% of their initial translation energy with about 10% of it being transferred to internal energy.

Figure 3 shows the dissociation rate as a function of exposure for 12 eV and 50 eV bombardments. The rate is calculated from successive groups of 9 incident CF molecules, each representing an exposure equivalent to 0.5 ML. Changes in the dissociation rate occurs as a result of the surface modification. From the figure, we note that at 12 eV, very few incident molecules dissociate. Dissociation occurs mainly during the initial stages (0-1 ML exposure), with a single dissociation event occurring at a higher exposure. The cumulative dissociation of incident molecules represents only ~3% of the trajectories. All resulting C fragments are absorbed on the surface, while in one case a single F atom is scattered away. 50% of the molecules that survive the collision scatter away. The scattered molecules generally leave the surface without reacting although in a small number of cases an additional species is abstracted. The scattered molecules lose ~90% of their initial translational energy and only 3.5% of the translational energy is transferred to internal energy.

At 50 eV, 60% of the incident molecules dissociate due to the collision. From figure 3, we see that during the initial stages of exposure the dissociation rate is very high (typically close to 100%). As the adlayer develops the rate of dissociation drops in an approximately linear fashion with increasing exposure. The drop in the dissociation probability can be attributed to the formation of the interfacial layer. Since the bulk of the atoms in this layer (C and F) are lighter than Si, incident molecules will generally lose less translational energy compares to collisions with the clean surface. Internal energy uptake is directly related to translational energy loss [35]. Hence, if less translational energy is lost, less energy is available to dissociate the molecule. Of the surviving molecules, 25% scatter away from the surface; while 75% are absorbed or penetrate into the substrate and react with Si or previously embedded C atoms. The calculation demonstrates that the scattered molecules retain only about 10% of their initial translational energy and that only 2% of the initial translational energy is transferred to the internal energy (about 0.8 eV).

Upon impact some of the surface atoms are displaced and they in turn displace the atoms they come in contact with. During these events clusters can be ejected from the surface to the gas phase. Analyzing the ejected species is useful in understanding plasma chemistry and determining specific reaction mechanisms responsible for surface modification. The total yields of the species that are ejected from the surface after 180 impacts are shown in figure 4. Ejected species are sub-categorized based on whether they arise as a result of scattering, sputtering or abstraction. From the figure, we note that the number and nature of the ejected species is strongly dependent on the incident energy. With increasing incident energy, the CF yield decreases dramatically, whereas the yield of C and F atoms increases. For 2eV, only CF species arising from direct scattering are observed (not shown).

For 12 and 50 eV incident energies, no Si-containing species have been found in the gas phase. Hence, no etching occurs and that there is only a net deposition in the cases studies. For 12 eV, F, CF and C_2F_2 species leave the surface. The F atoms originate both from dissociation of the incident molecules (50%) and by sputtering of F from the growing thin film. As was the case for 2eV bombardment, CF gas-phase species arise only as a result of direct scattering. C_2F_2 is produced by abstraction of a CF species from the thin film rather than by sputtering of a molecular fragment from the surface. For 50 eV, the ejected products are C, F, CF and C_2F_2 species. C, F and CF are ejected in roughly equal amount. About 90% of C arises from scattering of an atom after dissociation. The remainder is from sputtering of the deposited film. About 25% of the F atoms are from sputtering of thin film. At this energy we observe ejected CF arising from mechanisms other than scattering. Of the CF species, 82% are due to direct scattering, 4.5% are from sputtering and the remaining 13.5% are from abstraction by an atomic fragment. Again, the C_2F_2 species are solely due to abstraction by an incident CF. Relative to 12 eV, less C_2F_2 is produced at 50 eV. The abstraction probability decreases because the survival probability of CF molecules and the interaction time in the vicinity of the surface both decreased with increasing incident energy.

To gain a more complete understanding of the thin film development, it is important to examine the deposition of C and F atoms on the surface. The evolution of the adsorbed fractions, defined as the number of atoms remaining on the surface divided by the total

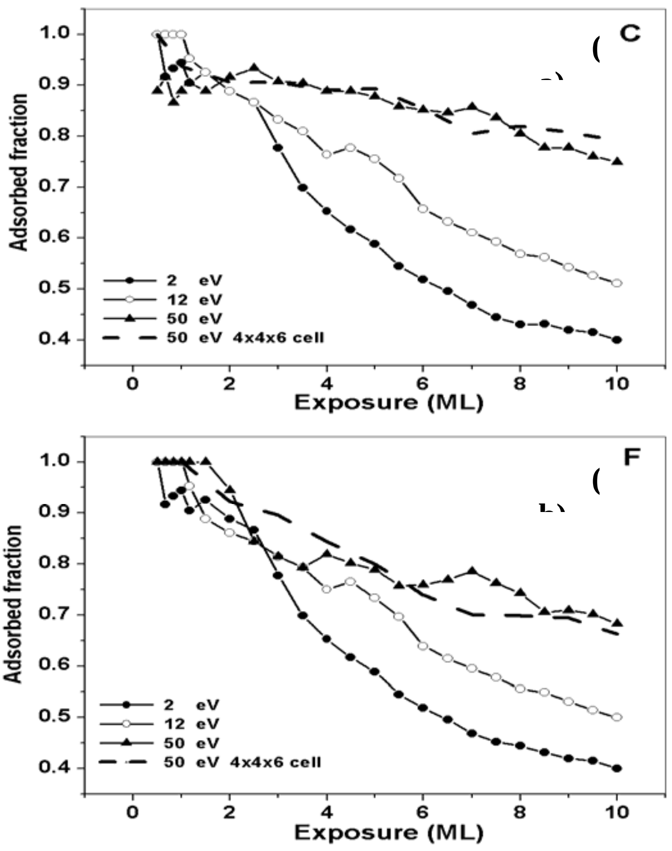

Figure 5: The adsorbed fraction of carbon and fluorine as a function of CF exposure for 2, 12 and 50 eV bombardment on Si (100) (3x3x4 unit cells) and 50 eV bombardment on Si (100) (4x4x6 unit cells). The adsorbed fraction is the number of C (F) atoms sticking on the surface divided by the number of incident molecules.

number of incident molecules, are shown in figure 5. Adsorbed fractions of both C and F are show for 2, 12 and 50 eV CF bombardment. Also shown are the adsorbed fractions for 50 eV bombardment of the larger 4x4x6 sample, illustrating the level of agreement between the two different sample sizes.

As shown in figure 5(a), the adsorbed fraction of C atoms depends strongly on the incident energy of the molecules. During the initial stages of adlayer formation, the sticking probability of the C atoms for 2 and 12 eV incident molecules is 1. For 2 eV, the adsorbed fraction decreases sharply after 1 ML, whereas for 12 eV, the drop occurs after a longer exposure. For 50 eV, during the initial stages the adsorbed fraction of C atoms is less than unity due to scattering. As the exposure increases the adsorbed fraction drops in a steady fashion for all three incidence energies. The drop is steepest for the lowest energy and most gradual for the highest energy.

The adsorbed fraction of F as a function of CF exposure is presented in figure 5 (b). Similar to C, it is sensitive to the incident energy of the molecules. During the initial stages of adlayer formation, all F atoms are absorbed on surfaces at the three incident energies. Subsequently, the adsorbed fraction decreases for all three incident energies. Note that since dissociation does not occur at 2 eV incidence energy and is only a minor component at 12 eV, the curves for the F adsorbed fraction essentially match those for C at the same energy. Only at 50 eV is there significant deviation between the two species.

Comparing the relative retention of C and F atoms for 50 eV incident energy, more C than F atoms remain on the surface as the exposure increases. Figure 6 shows the C/F ratio on the

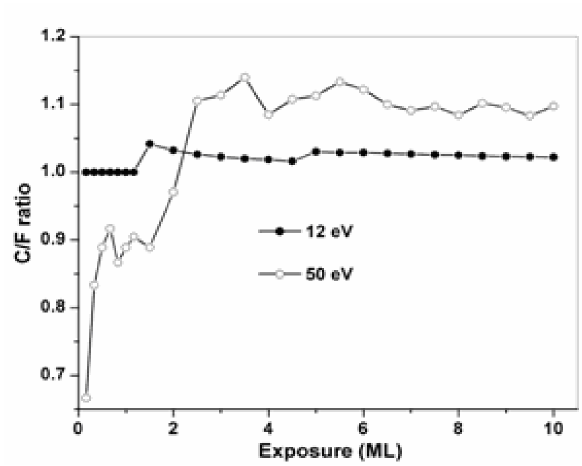

Figure 6: The ratio of the uptake of C to the uptake of F for 12 and 50 eV bombardments as a function of exposure.

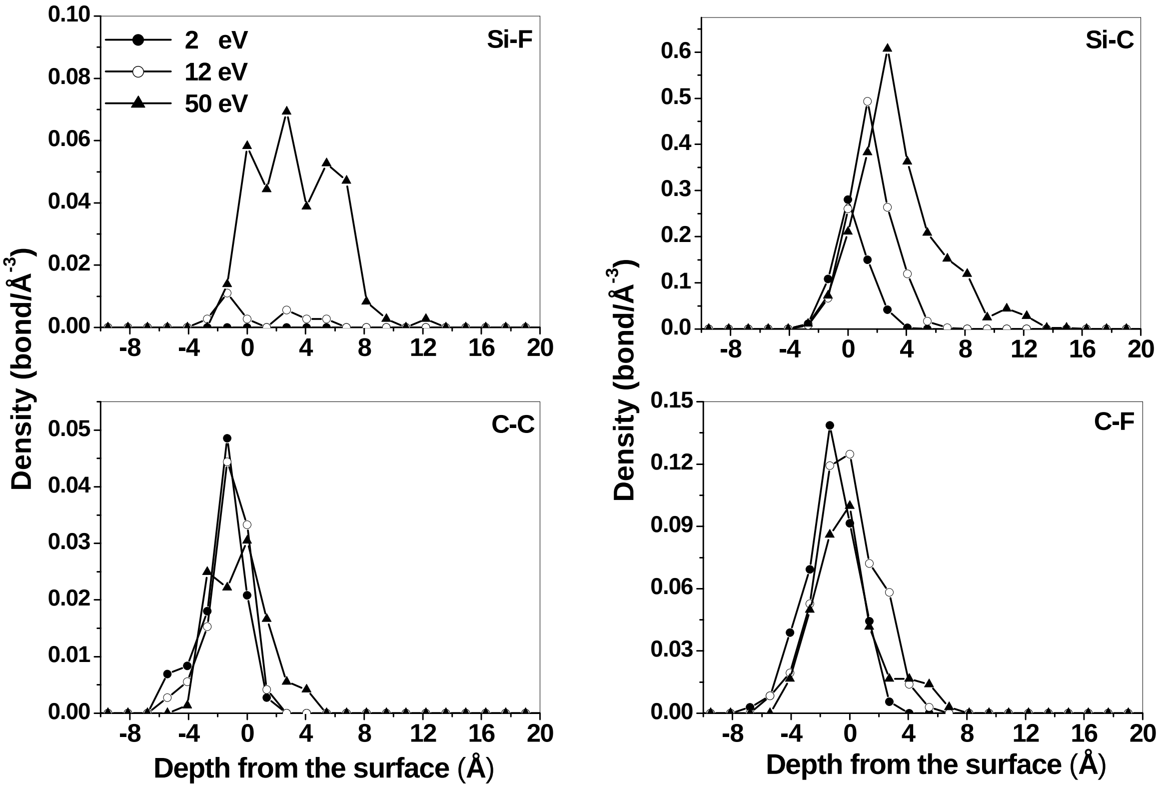

Figure 7: Calculated depth profiles of Si-F, Si-C, C-C and C-F bond density in the sample for 2, 12 and 50 eV bombardment after 10 ML exposure.

sample for 12 and 50 eV. For 12 eV, during exposure) the C/F ratio is unity. After 1.5 result of an F atom being sputtered from exposure of ~5 ML) is due to dissociative ratio is less than 1 before 2.5 ML exposure exposure, the film becomes C-rich the initial stages (less than 1.5 ML ML exposure, the C/F ratio increases as a the surface. The second increase (at an scattering of an F atom. For 50 eV, the C/F and the film is F-rich. After 2.5 ML

Reaction on the surface leads to the formation of Si-F, Si-C, C-C and C-F bonds in the film. In order to obtain more information about the surface chemistry of silicon subjected to CF bombardment, the calculated densities of these bonds as a function of depth are shown in

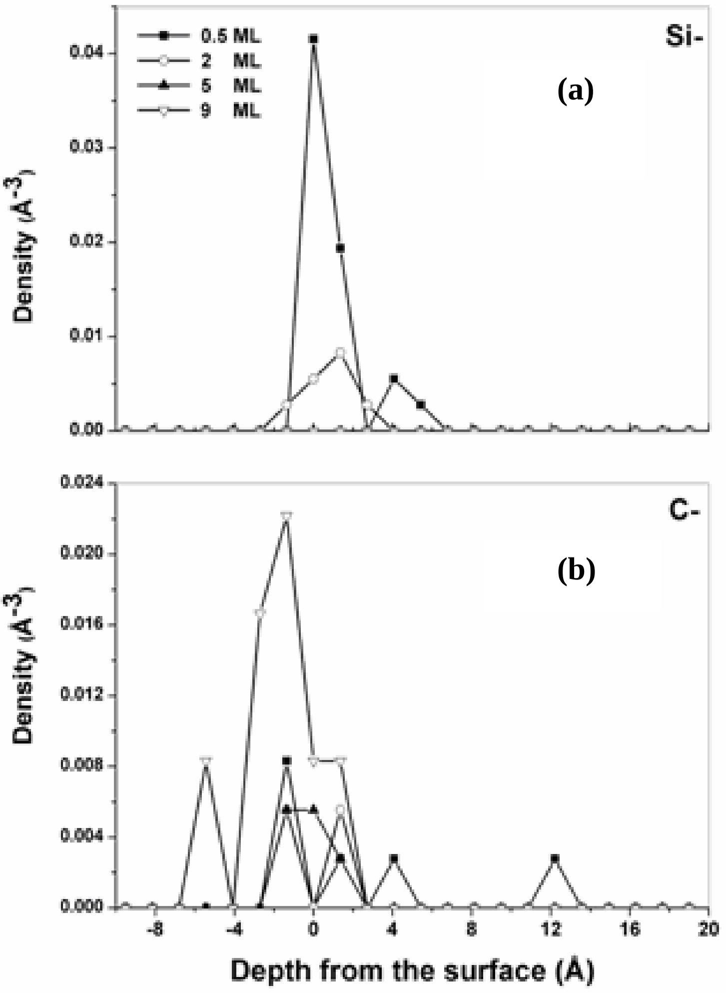

Figure 8: The dangling bond density of Si and C atoms as a function of sample depth after different exposure times. The surface was bombarded by 50 eV CF for exposures equivalent to 0.5, 2, 5 and 9 ML

figure 7. From the relative magnitudes, we note that the Si-C bonds are dominant. This is in part due to the fact that a single C atom can contribute up to 4 Si-C bonds. The density of Si-F bonds increases with increasing incident energy. No Si-F bonds are formed at 2 eV since dissociation does not occur. For 12 eV, the Si-F density is small due to the low dissociation probability. Since this energy is not sufficient to allow significant penetration into the bulk, the bonds are concentrated near the sample surface. For 50 eV, a 60% dissociation rate results in many more reactive F atoms being available to form Si-F bonds. From the figure we note that the resulting F atoms penetrate into the subsurface region of the film forming a broad Si-F distribution.

From figure 7, the Si-C bond density in the film increases and the distribution becomes broader with increasing incident energy. Even at 2 eV, there is significant formation of Si-C bonds. Unlike F, the carbon atom of the CF molecule can form bonds with silicon atoms on the surface without prior dissociation. At low kinetic energies Si-C bond formation is limited to the surface region. With increasing incident energy, the molecules and fragments penetrate deeper and react with bulk Si atoms to a higher degree. With increasing incident energy, the C-C bond density decreases slightly while the distribution becomes broader. The bulk of C-C bonds are formed above the position of the original Si surface; carbon that penetrates the Si lattice is much more likely to react with Si atoms. The C-F distribution has a similar energy

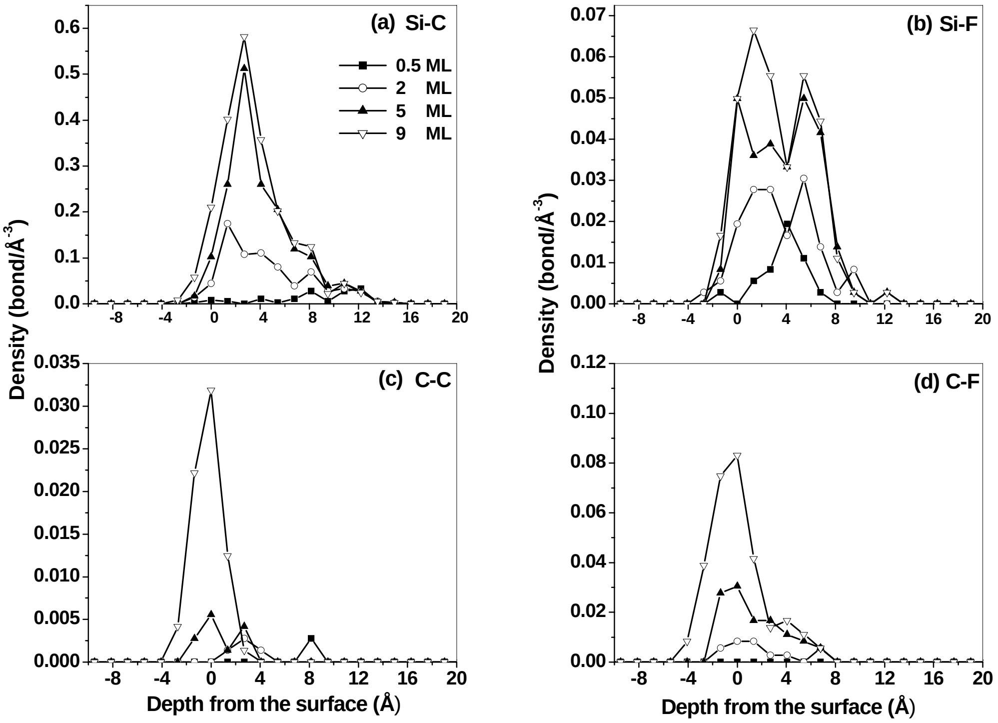

Figure 9: The Si-C, Si-F, C-C and C-F bond densities as a function of sample depth after different exposure times. The surface was bombarded by 50 eV CF for exposures equivalent to 0.5, 2, 5 and 9 ML.

dependence to the C-C distribution. Since there is very little dissociation at the lower incident energies, the presence of these bonds can be attributed to molecular adsorption rather than reaction after dissociation.

Incident molecules transfer the bulk of their initial kinetic energy to the surface. This energy transfer can cause recoiling of deposited C and F atoms into the bulk and breaking of existing bonds in the film. The process of film growth involves many complex chemical and physical reactions, involving bond breaking and formation. The dangling bond density is an important factor in determining the properties of the thin films formed. We present the dangling bond density of C and Si atoms as a function of a depth in figure 8 for different exposure times.

Note that dangling bonds are determined on the basis of atomic coordination. Surfaces bombarded by 50 eV CF for 0.5, 2, 5 and 9 ML exposures are shown. On clean Si (100)-(2x1), each surface atom has a single dangling bond available. As shown in figure 8(a), after 2 ML exposure the number of these bonds has been drastically reduced. The remaining Si dangling bonds are still concentrated near the initial surface region. Occasionally, isolated dangling bonds are created in the crystal bulk as a consequence of bombardment. These do not persist, presumably because of reaction with a subsequent atom that penetrates the crystal. C dangling bonds are present in the film at all stages after the initial exposure. As shown in figure 8(b), they are also concentrated near the surface region. The density of these bonds increases dramatically with exposure (as the overlayer grows).

In order to further describe the layer growth, the evolution of Si-C, Si-F, C-C and C-F bond densities for the same 4 exposures are presented in figure 9. The densities of all four bonds increase with increasing exposure. Comparing the relative densities, we note that the Si atoms preferentially react with C to form Si-C bonds. Relatively few Si atoms react with F

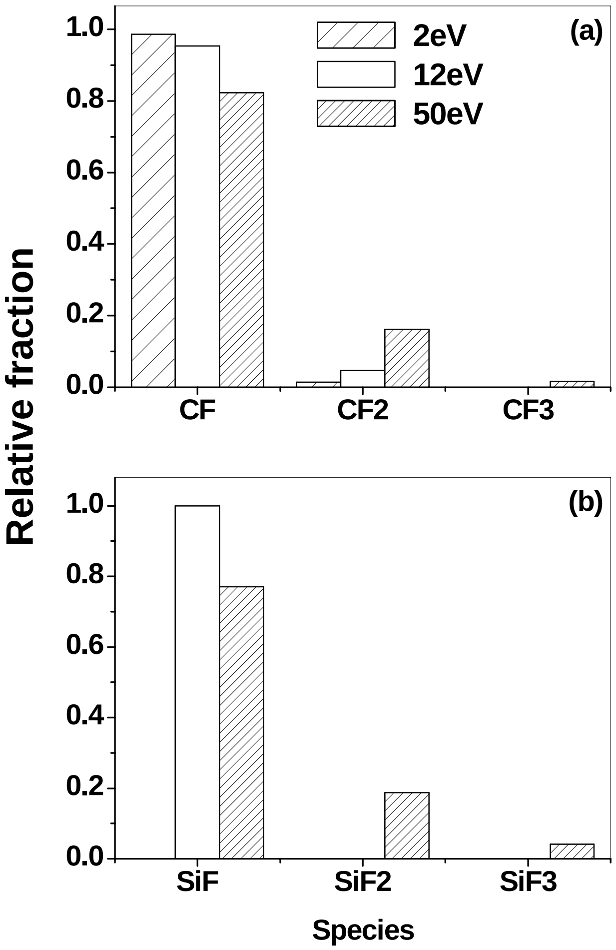

Figure 10: The relative fractions of (a) CF_x and (b) SiF_x(x=1-3) on the sample for 2, 12 and 50 eV bombardment of the sample. In each case the exposure was equivalent to 10 ML.

atoms to form Si-F bonds, as shown in figure 9(b). The absence of Si dangling bonds at higher exposures indicates that any Si-Si bonds that are broken are subsequently fully saturated, usually by C atoms.

During the initial stages, very few C-C bonds are formed. In contrast to bonds involving Si, these bonds only emerge strongly once the exposure exceeds 5 ML. This is matched by a strong increase in the C-F bond density. Two factors are at play here. Firstly, the increasingly thick adlayer results in more adsorption as a result of C-C bond formation rather than Si-C bond formation. Secondly, the decrease in the dissociation probability as the exposure increases results in an increase in the C-F bond density as a consequence of enhanced molecular adsorption.

Reactions at the surface give rise to more complex molecules, in the interfacial layer. Figure 10(a) shows the relative fractions of CF, CF_2 and CF_3 present in the sample after 10 ML exposure at the three incident energies. CF is always dominant, but with increasing incident energy the relative fractions of CF_2 and CF_3 increase. At energies of 2 and 12 eV, less than 10% of CF_2 is formed. CF_3 species only appear at 50 eV. Figure 10(b) shows the corresponding relative fractions of SiF, SiF_2 and SiF_3 in the substrate. For 12 eV, only SiF species are found. For 50 eV, SiF_2 and SiF_3 are also found.

We can also consider the evolution of chemical species as a function of exposure. Figure 11(a) shows the relative fractions of CF_x(x=1-3) species as a function of the exposure for 50 eV incident molecules. Consistent with figure 10 (a), CF species are dominant and very few CF_3 species are present in the sample during the film growth. With increasing exposure, the fraction of CF decreases, while the fraction of CF_2 increases. During the very early stages of exposure, some CF_2 species emerge on the sample. However, these are eliminated by the impact of subsequent molecules. Only with increasing exposure does the probability of production versus destruction shift in favor of CF_2 growth. Note that CF_3 is being continuously created and destroyed over the exposure range studied. Figure 11(b) shows the fractions of SiF_x(x=1-3) species as a function of the exposure. SiF is dominant and few SiF_3 species are formed. With increasing exposure, the fraction of SiF decreases slightly and SiF_2 increases.

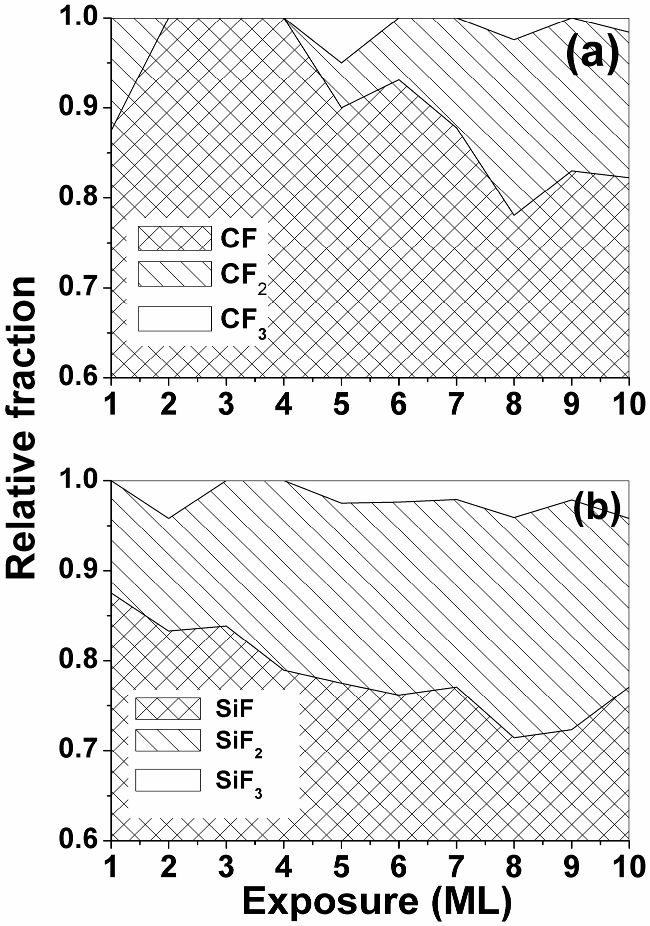

Figure 11: The relative fractions of (a) CF_x and (b) SiF_x(x=1-3) on the sample as a function of exposure to 50 eV CF molecules

6.4 Discussion

In the energy-selected experiments performed by Chang et al. [18; 29], HF-treated Si(100) surfaces were exposed to the equivalent of 10 ML CF^+ with 2, 10, 20 and 100 eV incident energies. The resulting overlayers were studies by X-ray photoelectron spectroscopy.

The results showed no silicon-carbon and fluorosilyl species present on the surface at 2 eV. Instead, CF was absorbed, forming polymeric carbon bonds. At 10 and 20 eV, the reaction was confined to the surface and little Si-F bonds formation was observed. CF, CF_2 and CF_3 species were found on the surface with the CF being dominant. At 100 eV incidence energy significant formation of SiF_x (x=1-3) was reported. In addition, the formation of SiC was observed at this energy. These experiments differ from the current (and previous) simulations in several crucial aspects. The first is the use of a H-terminated surface produced by acid treatment prior to insertion into vacuum chamber. The second is the absence of additional surface cleaning of the Si crystal before the ion bombardment experiments. Consequently, as noted in the paper, the surfaces bombarded experimentally had substantial amounts of "adventitious carbon" deposits. These deposits represent the bulk of the carbon signal detected by Chang et al. during the course of their experiments.

The previous simulations by Abrams and Graves involved incident energies of 50, 100 and 200 eV [28]. Our current results at 50 eV are in good agreement with their results. Hence the use of a single crystal surface and an improved Si-F potential did not dramatically alter the resulting interfacial layer. Under 50 eV bombardment the Si(100) surface is quickly roughened. Hence, the structure of the surfaces under bombardment in the two sets of simulations will rapidly converge.

In our MD simulations, the formation of silicon–carbon bonds at all energies is predicted. At 2 eV, 100% of absorbed species are CF and no SiF_x is formed. Molecular adsorption on the surface involving the formation of carbon chains is in agreement with the experimental results. The current simulations indicate that for low energy bombardment the main process will be layer growth as a result of molecular adsorption. In contrast, at higher energies the main process switches to dissociation and penetration of the crystal lattice. Considering the results for 2 eV bombardment, all molecules remain intact and layer growth occurs only through the adsorption of molecules. The sticking probability is highest on the bare surface and drops in a steady fashion as the total exposure is increased. If we seek to make comparison with the experimental results obtained by Chang et al. the situation is complicated by the presence of adsorbed hydro-carbon contaminants on the surface used experimentally. As a first approximation, we can regard these contaminants as being analogous to the fluorocarbon layers that are grown during the initial stages of the current simulation. In effect, while the simulation starts from the clean surface, the experiments start by bombarding an already "deposited" adlayer. Hence layer growth in the low energy experiments was mediated mainly via the surface contaminants rather than via the silicon atoms. Assuming the adlayer present in the experiments (essentially a carbon layer) behaves in a similar manner to the fluorocarbon layer that is deposited during the initial stages of the simulation, then the 2 eV experiments effectively start at a later stage of film growth than the current simulations. Based on figure 5, this would mean that the experiments started a point where the sticking probability was already relatively low when compared with the clean surface.

In the current simulations, film growth at 2 eV is facilitated by the presence of Si dangling bonds and subsequently by unsaturated carbon atoms in the growing CF films. In the experiments, the ability of the film to grow at low incident energies would be significantly hampered by the passivation of the Si surface atoms and the fact that contaminants tend to be fully saturated. 2 eV incident ions lack the energy to create new reaction sites on the surface. Consequently, the sticking probability in the experimental case should be substantially lower than that predicted by the simulations.

At 12 eV some CF molecules that impact the bare surface dissociate and the resulting F atoms react with Si atoms in the crystal to form fluorosilyl. At this energy the dissociation probability remains very low. The bulk of the molecules that dissociate do so during the early stages of exposure, with the growing adlayer reducing the dissociation probability. The current simulations show a small amount of CF_2 formation and no CF_3 formation. In marked contrast, the experimental results for 10 eV bombardment show significant formation of both CF_2 and CF_3 species on the surface. One possible reason for the discrepancy is the excitation state of the molecule prior to impact with the surface. In the simulation the molecules initially have no extra internal energy, whereas the ions used in the experiment may be in an excited state prior to impact with the surface. In addition, neutralization of the ions in the vicinity of the surface can results in the formation of an excited molecule (or even direct dissociation). Consequently, the energy required for dissociation in the experimental case may be less than that required in the current simulations. This would enhance the dissociation rate and allow for formation of more complex molecular species.

At higher incident energy, CF molecules and fragments penetrate more deeply into the crystal. At 50 eV, the simulated results show that F atoms can penetrate to a maximum depth of 10 Å below the initial surface. Compared to 12 eV, more C and F atoms are generated. The probability of F atoms reacting with Si and C atoms to form SiF_x and CF_x (x=1-3) is greatly enhanced. At both 12 eV and 50 eV, the simulations indicate the formation of a “dual-layer” fluorine structure. The fluorine is found to have a higher concentration deep in the crystal as would be expected due to the higher energy “carried” by this atom and also (more counter-intuitively) to have a higher surface concentration. The enhanced F concentration in the surface region is consistent with experimental results of Chang et al., who suggested a combination of higher fluorine diffusivity and higher volatility as the origin [18]. The current simulations suggest that some surface enrichment can occur directly as a result of bombardment.

In the experiments, 20 and 100 eV CF molecules have sufficient energy to penetrate the contaminant film and break Si-H bonds on the surface to create reactive sites. Consequently CF_x and SiF_x species were detected. The best agreement between the current simulations and the experimental results is found for the higher incident energies. This is at least in part due to the passivation and the contamination layers that were present on the experimental surface. As the incident energy is increased, these layers become less important in determining the reactions that occur on the surface. In addition, any initial or neutralization-induced excitation of the incident molecules becomes relatively less important as the translational energy is increased.

6.5 Conclusions

MD simulations of CF bombardment of Si (100)-(2x1) were performed for incident energies of 2, 12 and 50 eV. At 2 eV, CF molecules are absorbed on the surface and only silicon-carbon bonds are formed. At 12 eV and 50 eV, silicon carbide and fluorosilyl species are found, which were previously observed in experimental measurements. For all incident energies, Si-C bonds are formed on the surface. At low energy Si-C bond formation is limited to the surface region. In the interfacial layer formed at higher energies, SiF species are dominant over SiF_2 and SiF_3 and CF species are dominant over CF_2 and CF_3. The simulations produce results that are consistent with experimental measurements at the higher energies even though the initial surfaces differ. At lower incidence energies the surface state critically influences the overlayer formation. Hence, the results from simulation and experiment show substantial differences.

References

[1] J. P. Chang, J. W. Coburn, J. Vac. Sci. Technol. A 21 (2003) S145.

[2] J. W. Coburn, Appl. Phys. A - Mater 59 (1994) 451.

[3] I. T. Martin, E. R. Fisher, J. Vac. Sci. Technol. A 22 (2004) 2168.

[4] K. L. Williams, C. I. Butoi, E. R. Fisher, J. Vac. Sci. Technol. A 21 (2003) 1688.

[5] H. Sugai, H. Kojima, A. Ishida, H. Toyoda, Appl. Phys. Lett. 56 (1990) 2616.

[6] D. Vender, M. Haverlag, G. S. Oehrlein, Appl. Phys. Lett. 61 (1992) 3136.

[7] E. L. Z. Velasquez, M. C. A. Fantini, M. N. P. Carreno, I. Pereyra, H. Takahashi, R. Landers, J. Appl. Phys. 75 (1994) 543.

[8] J. M. Webb, Z. H. Amini, Characteristics of gate oxide surface material after exposure to magnetron-enhanced reactive ion etching plasma, Santa Clara, CA, USA, SPIE, 1991, 47.

[9] G. S. Oehrlein, J. Vac. Sci. Technol. A 11 (1993) 34.

[10] E. S. Aydil, R. A. Gottscho, Y. J. Chabal, Pure & Appl. Chem (1994) 34.

[11] F. Gou, M. A. Gleeson, A. W. Kleyn, Vacuum 81 (2006) 196.

[12] E. T. Ada, L. Hanley, S. Etchin, J. Melngailis, W. J. Dressick, M.-S. Chen, J. M. Calvert, J. Vac. Sci. Technol. B 13 (1995) 2189.

[13] L. Hanley, D. G. Schultz, E. T. Ada, Surface modification by molecular ions, AIP, 1999, 757.

[14] W. M. Lau, R. W. M. Kwok, Int. J. Mass Spectrom. Ion Processes 174 (1998) 245.

[15] W. R. Koppers, M. A. Gleeson, J. Lourenco, T. L. Weeding, J. Los, A. W. Kleyn, J. Chem. Phys. 110 (1999) 2588.

[16] W. R. Koppers, K. Tsumori, J. H. M. Beijersbergen, T. L. Weeding, P. G. Kistemaker, A. W. Kleyn, Int. J. Mass Spetrom. 174 (1998) 11.

[17] J. W. Coburn, J. Vac. Sci. Technol. A 12 (1994) 1417.

[18] W. H. Chang, I. Bello, W. M. Lau, J. Vac. Sci. Technol. A 11 (1993) 1221.

[19] C. F. Abrams, D. B. Graves, J. Vac. Sci. Technol. A 16 (1998) 3006.

[20] S. Chiba, T. Aoki, J. Matsuo, Nucl. Instrum. Methods Phys. Res., Sect. B 180 (2001) 317.

[21] D. Humbird, D. B. Graves, J. Chem. Phys. 120 (2004) 2405.

[22] I. K. Jang, S. B. Sinnott, J. Phys. Chem. B 108 (2004) 18993.

[23] M. G. Luca, H. L. Jan, A. Fasolino, M. Evert Jan, Phys. Rev. B 72 (2005) 214103.

[24] T. A. Schoolcraft, A. M. Diehl, A. B. Steel, B. J. Garrison, J. Vac. Sci. Technol. A 13 (1995) 1861.

[25] F. H. Stillinger, T. A. Weber, Phys. Rev. Lett. 62 (1989) 2144.

[26] C. F. Abrams, D. B. Graves, J. Appl. Phys. 86 (1999) 5938.

[27] C. F. Abrams, D. B. Graves, J. Appl. Phys. 88 (2000) 3734.

[28] C. F. Abrams, D. B. Graves, J. Vac. Sci. Technol. A 19 (2001) 175.

[29] I. Bello, W. H. Chang, W. M. Lau, J. Vac. Sci. Technol. A 12 (1994) 1425.

[30] M. P. Allen, D. J. Tildesley, Computer Simulation of Liquids, New York, Oxford Science Publications, 1987.

[31] D. W. Brenner, Phys. Rev. B 42 (1990) 9458.

[32] J. Tanaka, C. F. Abrams, D. B. Graves, J. Vac. Sci. Technol. A 18 (2000) 938.

[33] L. Verlet, Phys. Rev. 159 (1967) 98.

[34] H. J. C. Berendsen, J. P. M. Postma, W. F. v. Gunsteren, A. DiNola, J. R. Haak, J Chem Phys 81 (1984) 3684.

[35] F. Gou, M. A. Gleeson, A. W. Kleyn, PCCP 8 (2006), 5522.

Chapter 7

Molecular dynamics simulation of CH_3 interaction with Si (100) surface

Abstract: Molecular dynamics simulations of the CH_3 interaction with Si (100) were performed using the Brenner potential. The H/C ratio obtained from the simulations is in good agreement with available experimental data. The results show that H atoms preferentially react with Si. SiH is the dominant form of SiH_x generated. The amount of hydrogen that reacts with silicon is essentially energy-independent. H atoms do not react with adsorbed carbon atoms. The presence of C-H bonds on the surface is attributed to molecular adsorption.

7.1 Introduction

Hydrocarbon thin films deposited by plasma enhanced chemical vapor deposition (PECVD) are important for many applications because their structure can be varied over a wide range [1]. Their property of high hardness makes them suitable as wear-resistant coatings, for example as protective layers in fuel injection valves and in very thin wear-resistant coatings on magnetic discs and magnetic read/write heads. The deposition of these films has been an active topic in fundamental research [2]. Hydrocarbon interactions are also important for the performance and the design of the ITER fusion reactor [3; 4]. Carbon is proposed as the material for the ITER divertor target [5]. Chemical sputtering of this wall will lead to the release of hydrocarbon compounds, which can be re-deposited elsewhere in the vessel. A better knowledge of film formation processes and transport of hydrocarbon species is useful in attempting to predict and minimize dust formation [6-8].

Although hydrocarbon films have been intensively investigated during recent years [9-12], the growth mechanism is still poorly understood due to limitations of in-situ and real-time measurement techniques for surface reactions in a plasma environment. Atomic scale molecular dynamics (MD) is a potential complement for experimental techniques when seeking to understand hydrocarbon-surface interaction mechanisms [7; 13; 14]. There have been many studies on MD simulations of hydrocarbon-surface interactions [15]. The initial film growth on the substrate, the steady-state deposition coefficients, and the H/C ratios of the deposited layers can be independently studied as a function of energy and molecular exposure.

7.2 Description of molecular dynamics model

The present investigation was performed on the basis of molecular dynamics simulation of CH_3 interacting with silicon surfaces. In an MD model, all atoms in the system are traced by Newtonian mechanics. Particles move under the influence of forces, derived from an interatomic potential. In this work, the Brenner-Tersoff type potential for C-H-Si system is used [16-24].

A (2x1) reconstructed Si (100) crystal consisting of 4x4x6 unit cells with a lateral area of ~500 Å2 and a depth of ~35 Å was created. The simulation cell had periodic boundaries in the x- and y-directions. The bottom two layers were held rigid in order to maintain the structure. At the beginning of each impact, the incident CH_3 molecule was placed at a distance above the substrate beyond the cutoff of the potential. The position of the incident molecule in the x- and y-directions was chosen randomly. Each trajectory is run for 1000x0.5 fs, giving a total of 0.5 ps per impact. The spatial trajectories of the atoms were integrated explicitly using the velocity Verlet scheme [25]. The substrate temperature was kept constant at 300 K, using the Berendsen heat bath algorithm [26]. The deposition process was simulated by exposing the substrate sequentially to CH_3 molecules. All impacts were normal to the surface. Energies of 60, 100 and 150 eV per molecule were simulated.

The simulated films were characterized based on coordination number, mass densities and corresponding depth profiles. The coordination of an atom was determined using the first minimum of the pair correlation function as the cutoff length. Depth profiles were calculated by averaging over intervals of 1.3575 Å. In this article twofold, threefold and fourfold coordinated carbon atoms are referred to as *sp1*, *sp2* and *sp3* hybridized, respectively.

7.3 Results and Discussion

After CH_3 collides with the surface, some C and H atoms are deposited. Figure 1(a) shows the number of H atoms sticking to the surface as a function of exposure for different energies.

With increasing exposure, the number of H atoms deposited on the surface increases for all incident energies. The deposition of H is largest for 60 eV incident energy. At 100 and 150 eV the deposition rates are effectively identical. For the range of exposures studied, an upper limit to the uptake of H was not observed. During the initial stages of exposure, the rate of H adsorption is highest. After ~7 ML exposure, steady-state deposition is established at a lower rate. At steady-state the deposition rates, defined as the number of H atoms deposited on the surface per incident CH_3, are 0.39, 0.19 and 0.16 for 60, 100 and 150 eV incident energies, respectively. Figure 1(b) shows the H/C ratio deposited on the surface as a function of exposure to CH_3 at the three different incident energies. In each case the H/C ratio initially

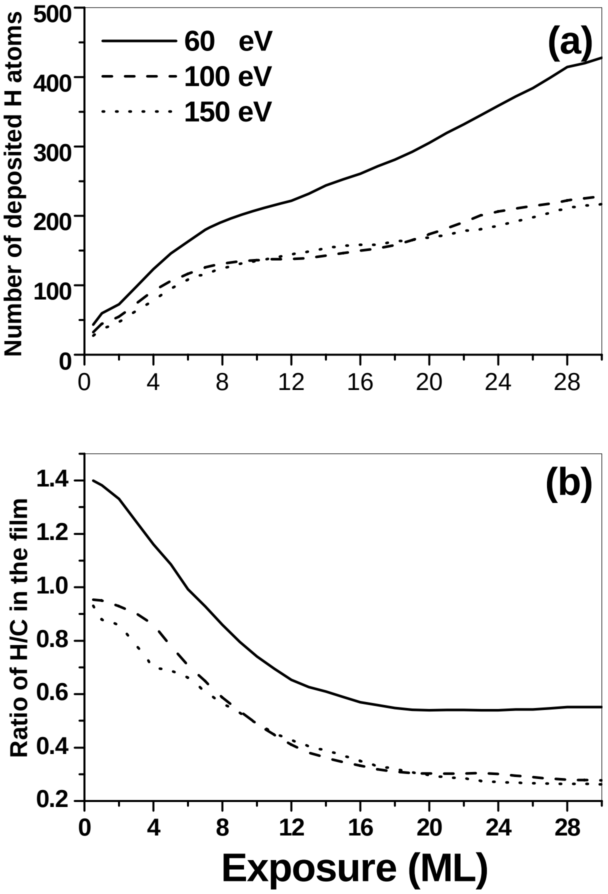

Figure 1: (a) Number of H atoms on the substrate as a function of exposure to CH_3 with incident energies of 60, 100 and 150 eV. **(b)** H/C ratio on the substrate as a function of exposure to CH_3 with incident energies of 60, 100 and 150 eV.

decreases rapidly before reaching a constant value. For 60 eV, the H/C ratio drops from ~1.4 during the early stages to ~0.54 after 15 ML exposure. For 100 and 150 eV, a steady-state H/C ratio of ~0.29 is obtained after 20 ML exposure. This is in good agreement with experimental data by Plank et al [10]. They measured H/C ratios at room temperature ranging between 0.3 and 0.4. Their HC ratio was effectively independent of the incident energy for energies from 150 to 3.0 keV. Our simulations suggest that this independence extends down to 100 eV.

Figure 2 shows the depth profiles of Si, H and C atoms in the films for 60, 100 and 150 eV after 30 ML exposure. From the figure, we note that the densities and distributions of H atoms are strongly dependent on the incident energy, whereas the C densities and distributions are relatively unchanged. With increasing energy, the C atoms penetrate somewhat deeper into the substrate, but the overall shape and intensity of the distribution are largely unaffected. In contrast, the distribution of H atoms shows major changes as the incident energy is increased. At all energies, this distribution contains 2 peaks. One is located above the position of the initial surface and the other is located beneath it. With increasing incident energy, the intensity of the H peak above the initial surface decreases, while the intensity of the peak below the initial surface is relatively unchanged but shifts to deeper in the bulk. For 60 eV, most C and H atoms are concentrated above initial surface and some Si atoms are shifted outward from

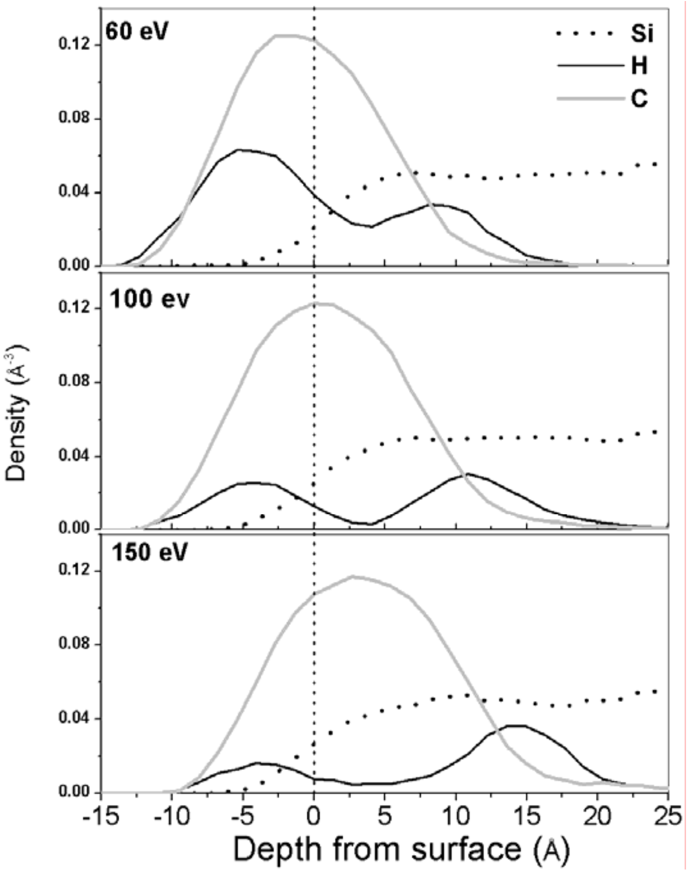

Figure 2: Atomic density as a function of substrate depth after exposure of Si(100) to the equivalent of 40 ML of CH_3 with incident energies of 60, 100 and 150 eV.

their initial position. At the top of the adlayer, the C/H ratio is approximately 1. For 100 eV, the amounts of C and H atoms above and below the initial surface are almost equivalent. For 150 eV, most C and H atoms are located beneath the initial surface.

From figure 2 we note the position of the lower peak always coincides with the interface between the bulk silicon lattice and the mixed Si/C interfacial layer. The upper H peak is located at the outer surface region of the growing adlayer. The double peak structure suggests that, as the deposition progresses, hydrogen atoms are depleted from the adlayer bulk.The previous figures demonstrate that C and H atoms penetrate the Si structure. These atoms may react with Si to form Si-C and Si-H bonds. The distributions of these bonds will influence the properties of the film. Figure 3 shows the densities of Si-C and Si-H bonds as a function of the depth from the initial surface. From figure 3(a), it is seen that most Si-C bonds are concentrated beneath the initial surface. These bonds do not show a strong energy dependence. With increasing incident energy, the density maximum shifts deeper, the distribution becomes broader and the density of the Si-C bonds increases. From figure 3(b), we note that practically all Si-H bonds are located beneath the initial surface. With increasing incident energy, the density maximum shifts deeper into the bulk. At 150 eV, the density maximum is located at ~15 Å beneath the initial surface. Combining this figure with figure 3, the second peak in the H atom profile can be attributed to Si-H bonds. Unlike the Si-C distribution, the width of the Si-H distribution does not change significantly with increasing incident energy. Instead, broad

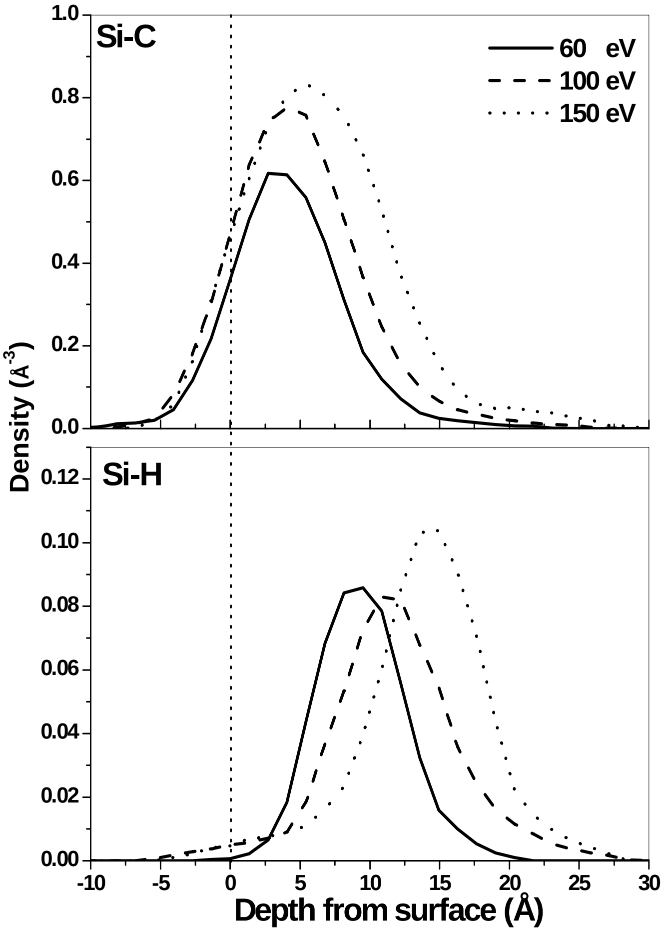

Figure 3: Bond density profiles of Si-C and Si-H as a function of substrate depth after exposure of Si(100) to the equivalent of 40 ML of CH_3 with incident energies of 60, 100

wings develop on either side of a sharp central distribution. Figure 4(a) shows the density of C*sp1*-C*sp1*, C*sp2*-C*sp2* and C*sp3*-C*sp3* bonds as a function of the depth for 60, 100 and 150 eV after 30 ML exposure. C*sp3* bonds are an indication of diamond-like carbon, while C*sp2* bonds are indicative of graphitic carbon. C*sp1* bonds are more molecular in nature and indicate a more porous, amorphous structure. From the figure, we note that most of C*sp1*-C*sp1* and C*sp2*-C*sp2* bonds are concentrated above the initial surface. At 60 eV, no C*sp1*-C*sp1* bonds are found. For 100 and 150 eV, both C*sp1*-C*sp1* and C*sp2*-C*sp2* bonds are present. With increasing incident energy, the total density of C*sp3*-C*sp3* bonds decreases, while C*sp2*-C*sp2* bonds increase. Hence, the deposition shifts from a predominantly diamond-like structure toward a more graphitic structure. Figure 4(b) shows the density of H-C*sp1*, H-C*sp2* and H-C*sp3* as a function of the depth from surface for 60, 100 and 150 eV. From the figure, it is seen that most H-C bonds are concentrated above the initial surface, contributed to the outer peak of H atoms in figure 3. In the films, the amount of H-C*sp1* is the smallest, while H-C*sp3* is dominant. With increasing the incident energy, the density of these bonds decreases. This decrease coupled with the weak adsorption of hydrogen evident from figure 1(b) suggests that

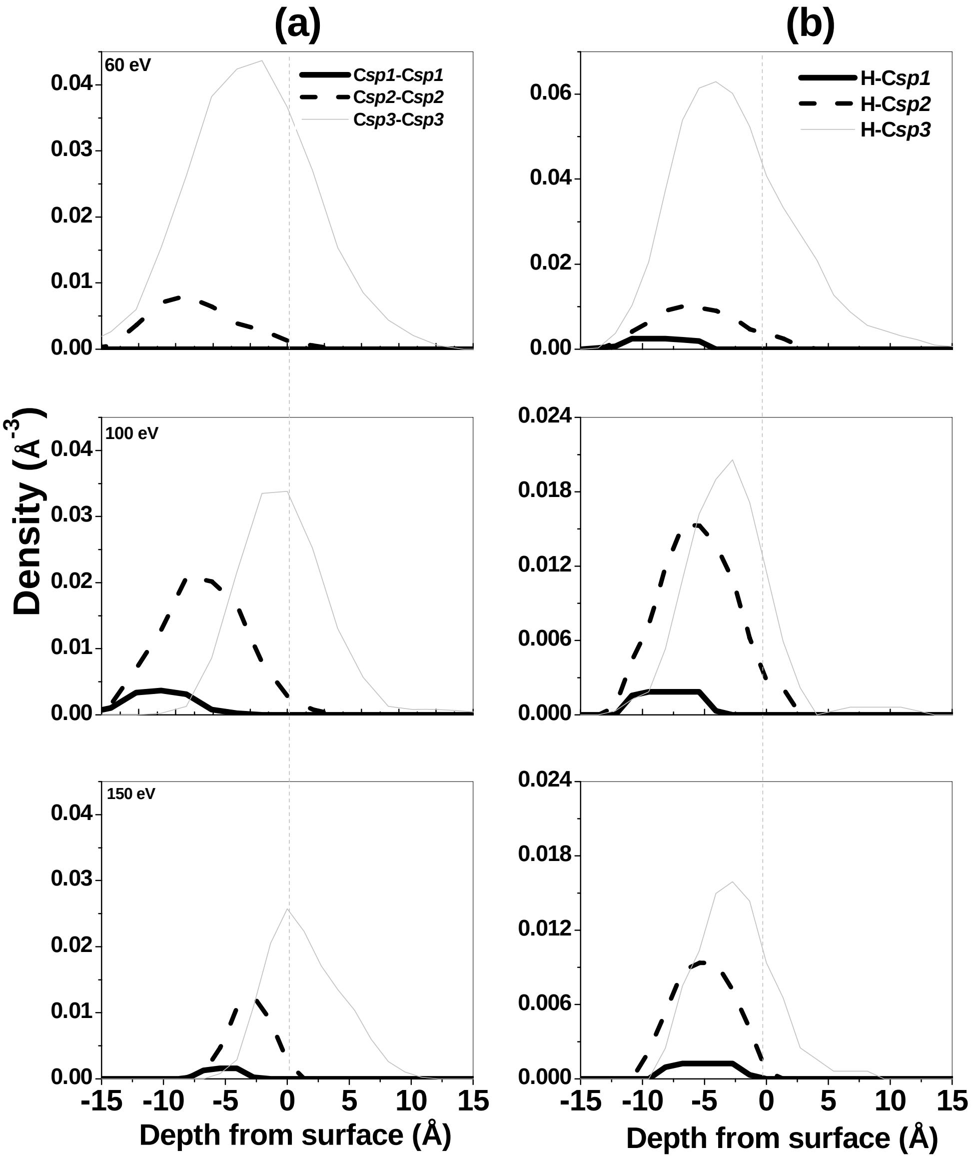

Figure 4: (a) Bond density profiles of *sp1-, sp2-* and *sp3*-hybridized C-C bonds as a function of substrate depth after exposure of Si(100) to the equivalent of 40 ML of CH_3 with incident energies of 60, 100 and 150 eV. **(b)** Density of H-C*sp1*, H-C*sp2* and H-C*sp3* as a function of the depth from surface for 60, 100 and 150 eV.

most C-H species arise from molecular-adsorption rather than from H reaction with pre-adsorbed C.

Figure 5(a) shows the relative fractions of CH_x on the modified surface (x=1-4). From the figure, we note that in the films, CH species are dominant. For 60 eV, all 4 species are present, while for 100 and 150 eV, no CH_3 and CH_4 species are evident. This can be attributed to enhanced collision-induced dissociation. With increasing incident energy, the CH_2 fraction decreases. From 60 eV to 100 eV, this fraction decreases sharply, while from 100 eV to 150 eV, the decrease is comparatively small. Figure 5(b) shows the corresponding relative fraction of SiH_x (x=1-4) on the surface. The relative fraction of SiH_x species is not very sensitive to

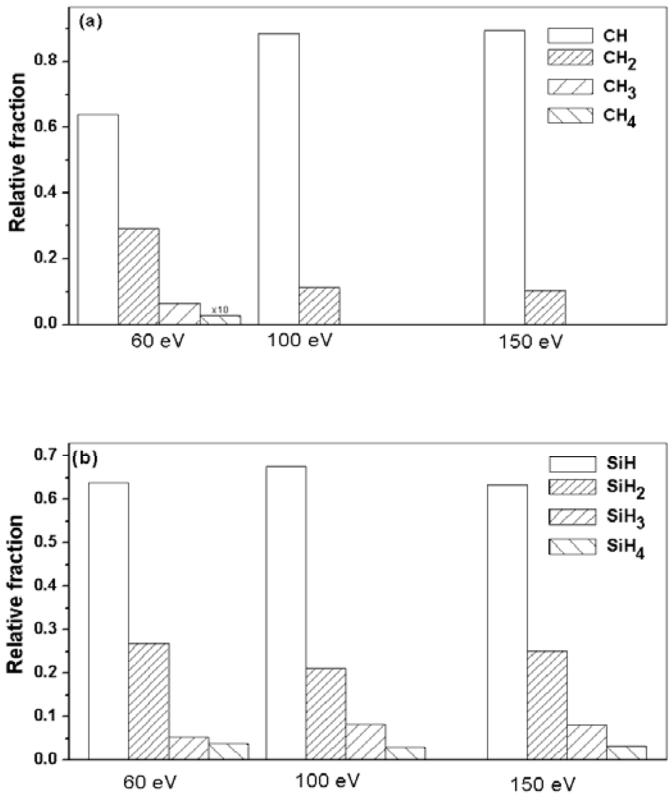

Figure 5: Relative fractions of **(a)** CH_x and **(b)** SiH_x on the surface after exposure of Si(100) to the equivalent of 40 ML of CH_3 with an incident energy of 100 eV.

the incident energy. Combined with figure 1(b) and figure 2, the results suggest that there is a finite amount of H that will react with Si atoms, which is independent of the incident energy. In contrast, the steady-state uptake of H is mainly due to CH_x adsorption.

7.4 Conclusions

The hydrogen distributions observed in the current simulations can be attributed to two independent processes. The first is reaction of H with Si. The hydrogen atoms are provided by dissociation of the incident CH_3. This process occurs during the early stages of exposure and is not very energy independent. The weak-energy dependent changes that are observed can be attributed to enhanced penetration and roughening as the energy is increased. As the total exposure increases, the initial Si-H layer is covered by a mixed Si/C/H adlayer. Thus, the SiH forms an interface layer between the Si bulk and the growing adlayer.

The second process is molecular adsorption of CH_x species. This is strongly energy dependent, since enhanced dissociation at higher energies will lead to less hydrogen on the surface. However, hydrogen atoms are depleted from the bulk of the hydrocarbon adlayer, most probably as a result of sputtering/etching of hydrogen atoms. At all incident energies, the bulk of the adlayer was composed of diamond-like carbon, while the surface was graphitic in nature. The relative amounts of diamond-like and graphitic carbon were energy dependent, with a more graphitic surface being formed at higher energies.

References

[1] A. von Keudell, W. Jacob, W. Fukarek, Appl. Phys. Lett. 66 (1995) 1322.
[2] A. von Keudell, W. Jacob, Prog. Surf. Sci. 76 (2004) 21.
[3] J. Roth, Phys Scripta T124 (2006) 37.
[4] I. I. Arkhipov, V. L. Bukhovets, A. K. Buryak, G. Federici, A. E. Gorodetsky, C. Ibbott, D. A. Komarov, A. N. Makhankov, A. Markin, I. V. Mazul, R. Tivey, I. G. Varshavskay, S. P. Vnukov, A. P. Zakharov, A. V. Ulianov, R. K. Zalavutdinov, J. Nucl. Mater. 313 (2003) 342.
[5] A. J. M. Buuron, J. J. Beulens, P. Groot, J. Bakker, D. C. Schram, Thin Solid Films 212 (1992) 282.
[6] W. Jacob, Thin Solid Films 326 (1998) 1.
[7] C. Hopf, A. von Keudell, W. Jacob, J. Appl. Phys. 93 (2003) 3352.
[8] C. Hopf, A. von Keudell, W. Jacob, J. Appl. Phys. 94 (2003) 2373.
[9] W. Moller, W. Fukarek, K. Lange, A. vonkeudell, W. Jacob, Jpn. J. Appl. Phys.1 34 (1995) 2163.
[10] H. Plank, W. Wang, W. Eckstein, R. Schworer, H. J. Steffen, J. Roth, J. Appl. Phys. 78 (1995) 5366.
[11] W. M. Wang, W. Eckstein, R. Schwörer, H. Plank, J. Roth, J. Nucl. Mater. 222 (1995) 1033.
[12] W. M. Wang, J. Roth, W. Eckstein, R. Schwöerer, H. Plank, M. H. Du, Nucl. Instrum. Meth. B 129 (1997) 210.
[13] E. Neyts, A. Bogaerts, R. Gijbels, J. Benedikt, M. C. M. van de Sanden, Nucl. Instrum. Meth. B 228 (2005) 315.
[14] E. Neyts, A. Bogaerts, R. Gijbels, J. Benedikt, M. C. M. van de Sanden, Diam. Relat. Mater. 13 (2004) 1873.
[15] B. J. Garrison, P. B. S. Kodali, D. Srivastava, Chem. Rev. 96 (1996) 1327.
[16] S. Ramalingam, D. Maroudas, E. S. Aydil, J. Appl. Phys. 86 (1999) 2872.
[17] S. Ramalingam, P. Mahalingam, E. S. Aydil, D. Maroudas, J. Appl. Phys. 86 (1999) 5497.
[18] J. Tersoff, Phys. Rev. B 39 (1989) 5566.
[19] J. Tersoff, Phys. Rev. B 37 (1988) 6991.
[20] J. Tersoff, Phys. Rev. B 38 (1988) 9902.
[21] J. Tersoff, Phys. Rev. Lett. 61 (1988) 2879.
[22] J. Tersoff, Phys. Rev. Lett. 56 (1986) 632.
[23] D. W. Brenner, Physical Review B 42 (1990) 9458.
[24] C. F. Abrams, D. B. Graves, J. Vac. Sci. Technol. A 16 (1998) 3006.
[25] L. Verlet, Phys. Rev. 159 (1967) 98.
[26] H. J. C. Berendsen, J. P. M. Postma, W. F. v. Gunsteren, A. DiNola, J. R. Haak, J. Chem. Phys. 81 (1984) 3684.

Chapter 8

General discussion

In previous chapters, we have investigated energetic particles (Ar, CF_x and CH_3) interacting with surfaces. That work focused on how parameters such as the energy and angle of incidence influence the simulation results. In this chapter, we will detail the interatomic potential (used in chapters 6-8). Some important simulation parameters (e.g. heat bath, relaxation time and cell size) and the effect of surface temperature on etching of Si by fluorocarbon will be investigated.

In MD simulations, one of the most critical considerations is the selection of the inter-atomic potential. For MD simulations involving silicon, the choice is typically made between the Stillinger-Weber and the Tersoff-Brenner potentials. Due to several inherent advantages, the Tersoff-Brenner potential was selected to describe the inter-atomic potentials in this thesis. This chapter mainly deals with the influences of the Berendsen heat bath (rising time, application time), relaxation of the sample (during and post-etching), the sample size, the time-step and total integration time of molecular trajectories. MD simulations on the effect of the substrate temperature on etching are presented. The results demonstrate that the efficiency of Si etching is promoted with increasing substrate temperature.

8.1 Introduction

Fluorocarbon plasma etching is widely used in the fabrication of integrated circuits in the semiconductor industry [1-8]. However, the complex coupling between plasma and surface makes it experimentally difficult to fully understand the etching mechanisms [9-11]. In order to gain a better insight into these mechanisms, molecular dynamics (MD) simulations have been extensively used in recent years to investigate the microscopic processes of plasmas interacting with surfaces [12-24]. Although much progress has been achieved using *ab initio* MD simulations on the atomic-scale, such methods are still difficult to apply to complex, large-scale systems. As a consequence many classical MD simulations, based on a variety of empirical inter-atomic potentials developed from density functional theory (DFT) calculations, have been performed over the last decade [12; 13; 17; 19; 25-28].

Diamond-like lattice structures (such as silicon), where each atom has four nearest-neighbors in a tetrahedral arrangement, cannot be correctly described by a simple two-body potential. Due to this and other shortcomings, potentials incorporating many-atom effects have been developed in order to provide a more realistic description of such systems. One such empirical potential, constructed by Stillinger and Weber (SW) [28-31], includes two- and three-body interaction terms. In this potential, the two-body interaction is used to describe bond stretching and the three-body interaction is used to describe the bond angle and to maintain an enforced tetrahedral lattice structure. The SW potential has been widely used in molecular-dynamics (MD) studies of F, Cl and CF_x (x=1-3) etching of Si and SiO_2 [28-38]. Using the SW potential, Barone and Graves have investigated chemical and physical sputtering of Si by F [17; 39]. Their results indicate that a F-containing reaction layer plays an important role during etching and that this layer is very sensitive to the incident energy. Smirnov et al. simulated CF_x (x=1-3) bombarding SiO_2 substrates using the SW potential [27]. Their results show that the Si and O etch yields increase with ion energy and exhibited a nonlinear dependence on the angle of impact. However, SW does not allow deviations from a tetrahedral structure. In order to maintain such a structure the bond lengths and bond angles are fixed, resulting in fixed bond strengths. Consequently it is unable to predict non-tetrahedral poly-types that are found under some conditions.

A more realistic model requires potentials that take into account the local environment and vary the bond strengths accordingly. One such set of potentials was developed by Tersoff [40-44]. In these potentials, the attractive term depends on the local environment of a specific atomic pair that effectively includes many-body interactions. A cutoff function is added to limit the range of the potential, thus reducing computation time. The main difference between the Tersoff and SW potentials is that the Tersoff potential can predict a non-tetrahedral geometry. Hence, it can be applied to a much broader range of materials than the SW potential. In addition, the Tersoff potential has been fitted to a range of different bulk phases of Si and is considered to be somewhat more transferable than the SW potential. Brenner developed this type of potential to describe systems containing hydrocarbons [18; 45]. Abrams and Graves further extended the Tersoff-Brenner potential to a C-F-Si system and used it to investigate CF_x (x=1-3) etching of silicon [12; 14-16]. They demonstrated that a $Si_xC_yF_z$ interfacial layer was formed and that the thickness of the reactive layer increased with the incident energy. The results of deposition on Si by CF^+ and CF_2^+ demonstrated that the transition from net deposition to net etching was related to the number of energetic F atoms in the incident species [12]. They made comparisons between the Tersoff-Brenner and SW potentials for incidence energies greater than 50 eV and reported that the two potentials led to quantitatively different results [15], however they pointed out the differences did not influence the qualitative nature of the results obtained.

In order to further optimize the Si-F-C system of Tersoff-Brenner potentials, Humbird and Graves re-parameterized the Si-F potentials using DFT [21]. With these improved potentials, they correctly predicted spontaneously etching of Si atoms, something that neither the SW potential nor the *un-optimized* Tersoff-Brenner potential is capable of [21; 46-56]. They simulated Si etching by F and Cl radicals in the presence of inert ion bombardment. The etch-reaction probabilities, surface coverages and etch product distributions calculated were consistent with experimental results [9]. In order to ensure the most correct description of Si chemistry, the new potentials were used for the work in this thesis simulating CF and CF_3 etching of silicon surfaces (chapters 4-7).

8.2 Molecular Dynamics Method

When running simulations many factors (such as the parameters within the potential, the integration method, the cell size, the heat bath (i.e. the energy balance mechanism), the time step, etc.) may alter the microscopic dynamics and ultimately influence the final results. Some factors will only slightly affect the results, while others may significantly alter the outcome. Our goal in this section is to illustrate the effects of some important factors on the simulation. This will serve both to introduce the simulation method and to provide an indication of the reliability of the generated results.

8.2.1 Expressions of the molecular dynamics

In MD simulations, one of the key points is the selection of the inter-atomic potentials. The potential functions used should be able to reproduce the binding energies, valences for covalent bonding and structural proprieties of the materials in question with good accuracy. As outlined above, to model systems containing Si, C and F, we have adopted the Tersoff-Brenner form of the potential functions as parameterized by Abrams and Graves and improved by Humbird et al [14; 21; 57]. The system potentials have the form:

$$E_b = V_R(r_{ij}) - \overline{b_{ij}} V_A(r_{ij}) \qquad \textbf{(1)}$$

where E_b is the binding energy and r_{ij} is the distance between atoms *i* and *j*. $\overline{b_{ij}}$ is a many-body empirical bond-order term (detailed below). V_R is used to describe the inter-atomic core–core repulsive interactions, and V_A is to model the attractive interactions due to the valence electrons. These terms have the following forms:

$$V_R(r_{ij}) = f_{ij}(r_{ij}) A_{ij} \exp(-\lambda_{ij} r_{ij}) \qquad \textbf{(2)}$$

and

$$V_A(r_{ij}) = f_{ij}(r_{ij}) B_{ij} \exp(-\mu_{ij} r_{ij}) \qquad \textbf{(3)}$$

where, A_{ij}, B_{ij}, λ_{ij} and μ_{ij} are fitting parameters and f_{ij} is a smooth cutoff function. Given by

$$f_{ij}(r_{ij}) = \begin{cases} 1 \quad if \;\; r_{ij} < R_{ij}^{(1)} \\ \frac{1}{2} - \frac{9}{16}\sin(\pi \frac{r_{ij} - (R_{ij}^{(2)} + R_{ij}^{(1)})/2}{R_{ij}^{(2)} - R_{ij}^{(1)}} - \frac{1}{16}\sin(3\pi \frac{r_{ij} - (R_{ij}^{(2)} + R_{ij}^{(1)})/2}{R_{ij}^{(2)} - R_{ij}^{(1)}}) \qquad if \;\; R_{ij}^{(1)} < r_{ij} < R_{ij}^{(2)} \\ 0 \quad if \;\; r_{ij} > R_{ij}^{(2)} \end{cases} \qquad \textbf{(4)}$$

This function, with two sinusoidal terms, gives a smoother termination of the potential because at the cutoff points it possesses a continuous third derivative. This leads to better energy and momentum conservation at minimal computational expense, since at any given time the fraction of atom pairs within the cutoff region is quite low.

The many-body empirical bond-order term $\overline{b_{ij}}$ in equation **(1)** modulates the valence electron densities and depends on atomic coordination and the bond angles. It has the form:

$$\overline{b_{ij}} = \frac{1}{2}[b_{ij} + b_{ji} + F_{CC}(N_{ij}^{(t)}, N_{ji}^{(t)}, N_{ij}^{(conj)})] \qquad \textbf{(5)}$$

Where F_{CC} is the Brenner-type correction function for a C-C bond. b_{ij} is the contribution of atoms adjacent to atom **i** to the bond order of the **ij** bond:

$$b_{ij} = \{1 + [\zeta_{ij} + H_{ij}(N_{ij}^{(F)}, N_{ij}^{(C)} + N_{ij}^{(Si)}]^{\eta_i}\}^{-\delta i} \qquad \textbf{(6)}$$

Here, H_{ij} is the correction function. $N_{ij}^{(F)}$ and $N_{ij}^{(Si)}$ are coordination numbers. ζ_{ij} is a bond competition function, modeling the bond lengths and bond angles:

$$\zeta_{ij} = \sum_{k \neq j} f_{ik}(r_{ik}) g_i(\theta_{ijk}) \exp\{\alpha_i [(r_{ij} - R_{ij}^{(e)}) - (r_{ij} - R_{ik}^{(e)})]_i^{\beta}\} \quad \textbf{(7)}$$

$R_{ij}^{(e)}$ is the equilibrium dimer bond length of atoms i and j. θ_{ijk} is the angle between the bonds ij and ik. $g_i(\theta_{ijk})$ is the potential energy penalty of a bond angle:

$$g_i(\theta_{ijk}) = a\left(1 + \frac{c^2}{d^2} - \frac{c^2}{d^2 + (h - \cos\theta)^2}\right) \qquad \text{if } i \in \mathrm{C} \qquad \textbf{(8)}$$

and

$$g_{Si,F}(\theta) = c + d[h - \cos\theta]^2 \qquad \text{if } i \in \mathrm{Si, F} \qquad \textbf{(9)}$$

The potential and its parameters are chosen to fit theoretical and experimental data obtained for realistic and hypothetical silicon configurations, namely the cohesive energy of several high-symmetry bulk structures, the lattice constant and bulk modulus of the silicon lattice in the diamond configuration.

TABLE 1: Two-body parameters in the Si–C–F potential.

Parameter	C–C[a]	C–Si[b]	C–F[c]	Si–Si[d]	Si–F[e]	F–F[e]
A(eV)	2605.8416	1597.311	909.20	1830.800	1046.953	6379.15
B(eV)	1397.0730	395.145	219.779	471.1800	155.9846	2813.818
λ(Å^{-1})	3.2803	2.9839	3.7128	2.4799	3.2447	4.6407
μ(Å^{-1})	2.6888	1.9721	2.1763	1.7322	1.6223	3.9462
$R^{(e)}$ (Å)	1.315	1.85	1.2718	2.35	1.6008	1.4119
$R^{(1)}$ (Å)	1.7	2.20454	1.7	2.7	1.83922	1.7
$R^{(2)}$ (Å)	2.0	2.50998	2.0	3.0	2.13922	2.0

[a]Ref.18. [b]Ref.42. [c]Ref.57. [d]Ref.35. [e]Ref.51.

TABLE 2: Parameter values for the bond angle functions, *g*

	^{C}Brenner[a]	^{Si}Tersoff[c]	^{F}Graves[e]
α	3.0 Å^{-1}	5.197495 Å^{-3}	4.0 Å^{-3}
β	1	3	3
a	2.0813x10^{-4}	...	...
c	330.0	0.0	0.0216
d	3.5	0.16	0.27
h	-1.0	-0.59826	-0.47
ŋ	1.0	0.78734	1.0
δ	0.5	0.635050	0.80469

The parameters used are listed in tables 1 and 2. The bonding between atoms is determined by the local environment through the bond-order function. This potential is extremely useful for predicting bond breaking and formation. Figure 1 shows the potential energy as a function of the distance between Si and F atoms for different bond order values. From the figure, we note that with decreasing b_{ij}, a transition from a net attractive potential to a net repulsive potential occurs.

8.2.2 Sample preparation

In order to perform etching simulations, an unreconstructed Si(100) crystal is created. The simulation cell has periodic boundary conditions in the x- and y-directions. The bottom two layers are fixed in order to maintain the structure. To obtain a *well-ordered* 2x1-reconstructed surface, atoms of the unreconstructed surface are displaced and dimerized and the resulting crystal is equilibrated using MD at the appropriate surface temperature (usually 300 K), yielding a relaxed Si(100)-(2x1) surface.

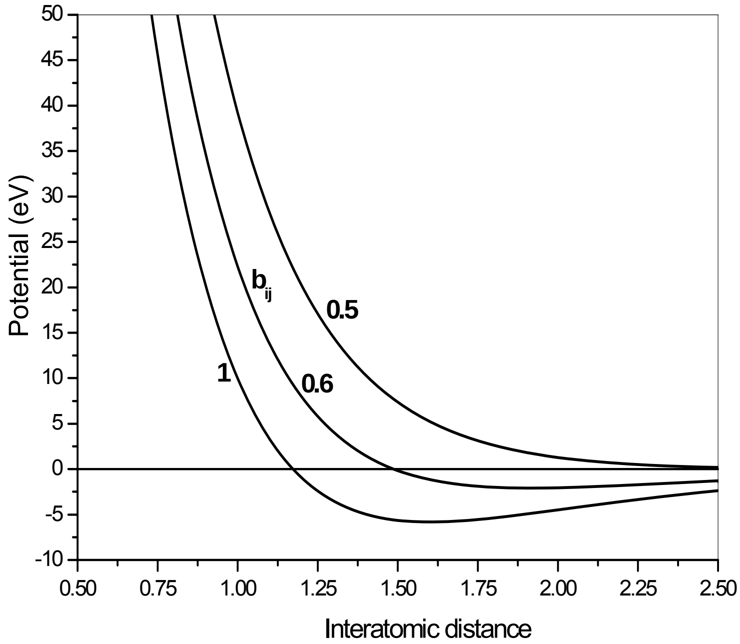

Figure 1: The potential energy as function of the distance between Si and F atoms for b_{ij}= 1, 0.6 and 0.5

At the beginning of each trajectory, CF_3 was placed at a randomly chosen location above the target. The initial orientation of CF_3 molecules was also selected randomly. For the simulations outlined in this chapter, the incident angle was always normal to the surface and the incident energy was always 100 eV. The trajectory of each incident molecule was integrated individually and after each integration atoms and molecules that were deemed to be not bonded to the surface were removed from the configuration before a new CF_3 molecule was directed at the surface.

Exposures are expressed in units of monolayer (ML), obtained by dividing the total number of the CF_3 molecules that have struck the surface by the number of Si atoms in the outermost layer of the original surface. The adsorbed coverage is based on the number of a particular species that stick to the surface and is also expressed in units of ML. Physical quantities such as etch rates are determined only after a steady-state has been established. The etch yield is also expressed in units of ML. In the current work, when no additional details are provided, the simulations were performed with conditions as outlined in chapters 3-7 and in [19; 58; 59].

8.2.3 Temperature control

When an energetic CF_3 molecule impacts with a surface some of its translational energy is lost. The magnitude of the energy loss depends on the incident energy. In scattering calculations, it was found that most of the translational energy lost is transferred to surface atoms (the remainder going to internal energy of the molecule) [see chapter 3]. The energy gained in this manner cannot escape naturally from the “substrate”, since periodic boundary conditions are adopted. In a real system, the energy deposited in a small region near the surface is dissipated by phonon propagation and thermal conduction. Because the periodic boundaries prevent the heat from dissipating out of the system, dedicated cooling processes are necessary during MD simulations to prevent unrealistically over-heating. In order to remove the energy added to the cell from the simulation, various schemes have been

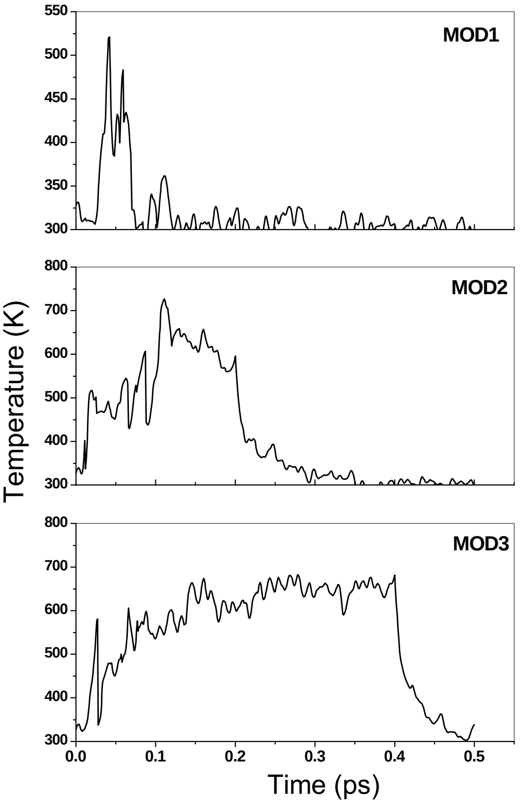

Figure 2: Instantaneous temperature of the sample as a function of time for three different heat bath application times.

developed. Examples include the Andersen thermostat[60], the Nose-Hoover thermostat [61-63] and the Berendsen thermostat [64]. In this thesis, the Berendsen heat bath is utilized.

8.2.3.1 Berendsen heat bath

The Berendsen scheme is widely used in plasma surface interaction (PSI) simulations [13; 50]. It maintains the sample temperature by coupling the simulated system to an external heat bath that is fixed at a desired temperature. The heat bath acts to supply or remove heat to/from the system as appropriate. The basic mechanism is to rescale velocities in order to achieve a mean kinetic energy consistent with the target bath temperature at each time step. The rescaling is done by a factor, λ:

$$\lambda = [1 + \frac{\delta t}{\tau_T}(\frac{T_{set}}{T} - 1)]^{1/2} \qquad (8)$$

Here, δt is the time step, T_{set} is the set-point temperature, and T is the macroscopic measured temperature. τ_T is the rising time of the heat bath. A small τ_T corresponds to a stronger heat bath relative to a large τ_T.

This algorithm is especially suitable for non-equilibrium molecular dynamics since local disturbances are kept to a minimum while preserving global gradients [65]. The method has been widely used in MD simulations of energetic particles interacting with surfaces. Barone and Graves investigated the effect of the heat removal on chemical and physical sputtering [39]. From their simulation results, they conclude that physical sputtering appeared more sensitive to heat removal than chemical sputtering.

8.2.3.2 Application time

During simulation the heat bath can be applied either over the entire impact integration time or only for some latter portion of it. In the current simulations, we test three modes of applying the Berendsen heat bath. The first is to apply the heat bath during the entire trajectory, referred to as MOD1. The second is to switch on the heat bath after each trajectory had run for 0.2 ps, referred to as MOD2 and the third is to switch on the heat bath after 0.4 ps, referred to as MOD3. The total integration time was 0.5 ps in all three cases. In order to illustrate the effect on the substrate temperature of the different models, three trajectories, one for each of the application times, were selected. Figure 2 shows the instantaneous temperature of the sample as a function of time for the three cases. It can be seen in the figure that for MOD1, after an initial rise due to the impact of the molecule, the temperature of the substrate quickly cools to about 300 K. The time during which the temperature of the substrate is more than 400 K is very short (about 0.05 ps). For MOD2, the impact results in a new equilibrium temperature being established between the point of impact and the time at which the heat bath is applied. After 0.2 ps, when the heat bath is switched on, the substrate temperature quickly cools down to the set-point value. For MOD3, the sample remains at ~600 K for about 0.3 ps before the heat bath is applied. In all three cases, application of the heat bath results in a rapid cooling of the sample. A long delay between the initial impact and the application of the heat bath results in the sample "equilibrating" at a higher temperature for a period of time.

Figures 3(a) and (b) show the coverages of C and F atoms on the sample as a function of exposure for the three models. For the F coverage, the difference between the models is small, while for the C coverage no significant difference is found between MOD1 and MOD2. However, the coverage of C atoms in MOD3 is somewhat higher than that of the other models. Figure 3(c) shows the Si etching yield as a function of the exposure. In this case, there is a difference between MOD1 and MOD2, while no significant difference is observed between MOD2 and MOD3. MOD 1 gives the lowest etch rate. Figure 4 shows the atomic densities of the sample as a function of the depth for MOD1, MOD2 and MOD3 after exposure to 20 ML CF_3. From the figure, we note that, by delaying the application of the heat bath, the peaks of C and F shift toward the bulk. This is a consequence of the higher etch rate of Si. Comparing MOD1 to MOD2, despite the difference in etch rates the atomic distributions in the reaction layer are quite similar. For MOD3, while the etch yield of Si atoms is similar to that of MOD2, the atomic distributions in the reaction layer are completely different. A long delay before application of the heat bath results in the sample temperature remaining un-physically high in MOD2 and MOD3. Hence it is important to ensure that the heat bath is applied sufficiently early in the integration process.

8.2.3.3 Rising time τ_T

In our simulations we typically use a rising time of 0.01 ps, consistent with work of [12; 14]. Figure 5(a) shows how the scaling factor λ varies as a function of the rising time τ_T. Here, we suppose that the instantaneous temperature, T, in equation (8) is 600 K, T_{set} is 300 K and δ_t is 0.001 ps. From the figure, we note that λ gets smaller with shorter rising time. This illustrates that if τ_T is small, coupling is stronger. Figure 5(b) shows the evolution of the sample temperature during impact by a single 100 eV CF_3 for rising times of 0.005 and 0.01 ps. With longer rising time the time during which the sample cools down to the set-point temperature increases. Figure 6(a) and (b) shows the coverage of C and F atoms as a function of exposure to 100 eV CF_3 for different rising times (0.05, 0.01 and 0.005 ps). In all three cases the heat bath is applied over the entire trajectory (MOD1). The data in the figure show no significant differences for the different times. Figure 6(c) shows the Si etch rate as a function of exposure to CF_3 with the different rising times. Again, no obvious differences are observed. Clearly,

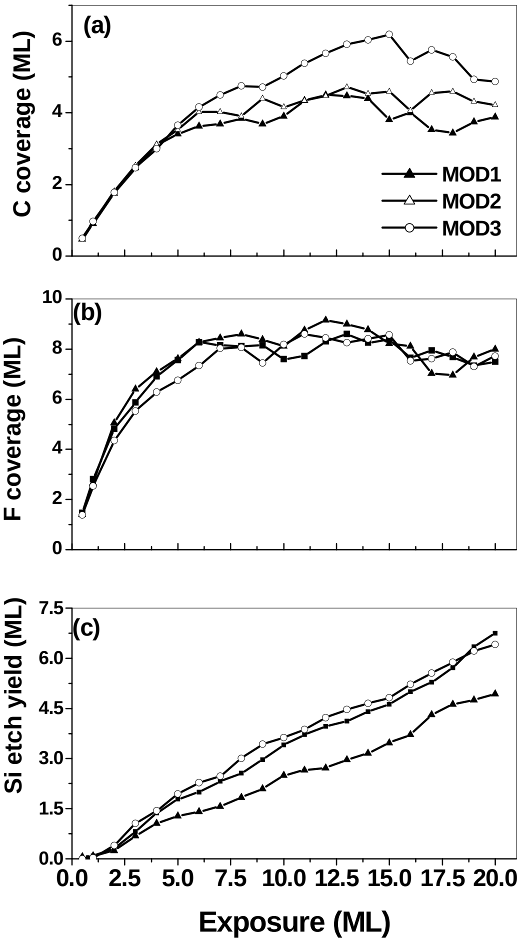

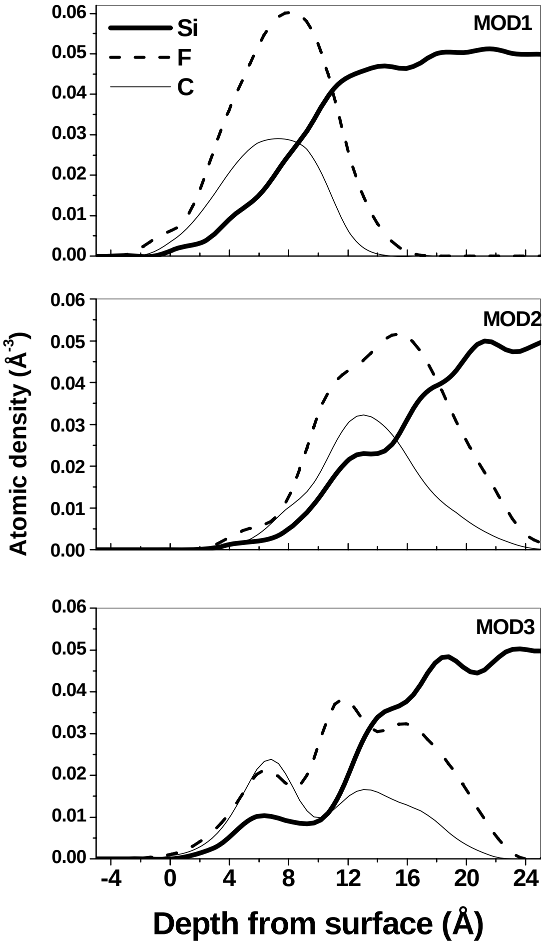

Figure 3 : Coverages of **(a)** C and **(b)** F atoms on the sample as a function of exposure for the three models; **(c)** Si etching yield as a function of the exposure.

Figure 4: Atomic densities of the sample as a function of the depth for MOD1, MOD2 and MOD3 after exposure to 20 ML CF_3.

these simulations are not very sensitive to rising times between 0.005-0.05 ps in the heat bath scheme if the heat bath is applied over the entire trajectory.

8.2.4 Relaxation

Bombardment of the sample is simulated by sequentially incident molecules. It is useful to establish if allowing a post-bombardment relaxation of the sample influences the final results. Changes may occur if the sample does not have time to fully equilibrate during the integration time of a single trajectory. Figure 7 shows that the atomic densities of the sample for an un-thermalizing sample and a sample thermalized for 20 ps at 300 K. From the figure, we note that some C atoms redistribution occurs. However, no major difference between the two surfaces is found. In addition, during thermalization no clusters were found to desorb from the surface, hence the overall composition did not change.

8.2.5 Time step and Integration time

In MD simulations the positions and velocities of atoms are obtained by integrating Newton's equations of motion. In this thesis, the velocity-Verlet scheme was used. This scheme computes the particle velocity v(t+dt) and position x(t+dt) at time t + dt as follows:

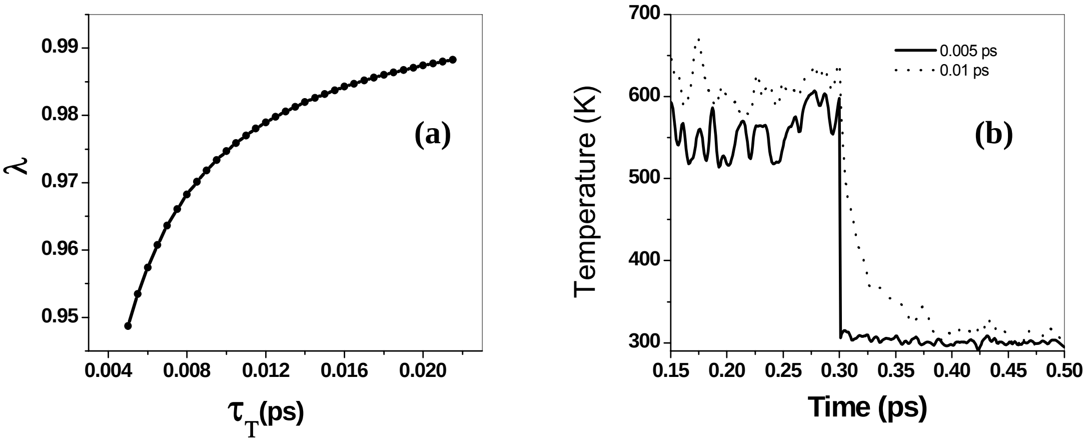

Figure 5: (a) Scaling factor λ variation as a function of the rising time τ_T. **(b)** Evolution of the sample temperature during impact by a single 100 eV CF_3 for rising times of 0.005 and 0.01 ps.

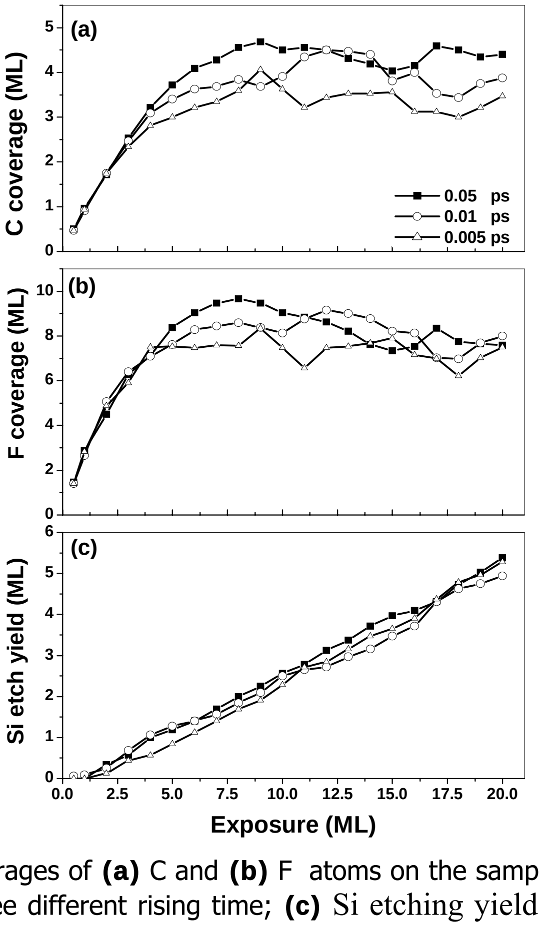

Figures 6: Coverages of **(a)** C and **(b)** F atoms on the sample as a function of exposure for three different rising time; **(c)** Si etching yield as a function of the exposure.

$$x(t+dt) = x(t) + v(t)dt + \frac{1}{2}dt^2\frac{f(t)}{m}$$
$$v(t+dt) = v(t) + \frac{f(t)+f(t+dt)}{2m}dt \qquad \textbf{(9)}$$

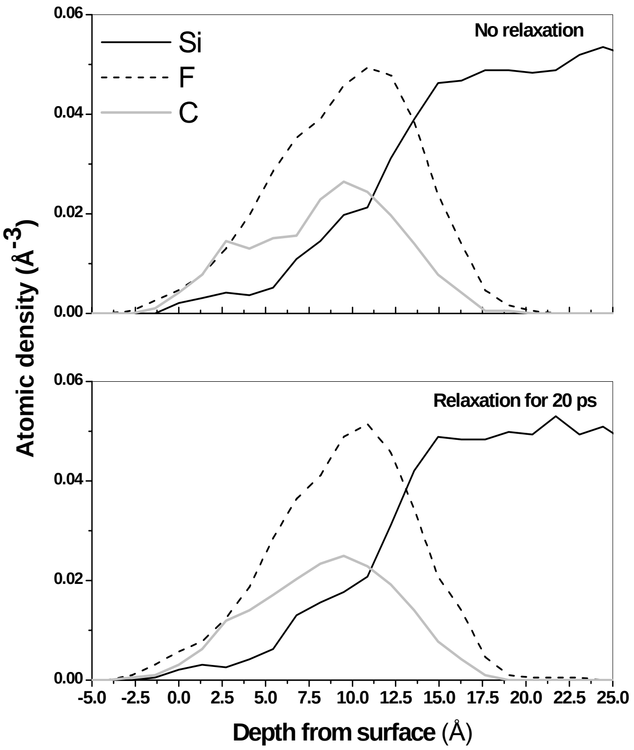

Figure 7: Atomic densities of the sample as a function of the depth for un-relaxed and relaxation of 20 ps after exposure to 20 ML CF_3.

where dt is the time step, m is the particle mass and f(t) is the total force acting on the particle at time t. Given the initial conditions x(0) and v(0), one can compute v(t) and x(t) simply by applying these two equations successively n times, with n=t/dt.

To test the influence of the time step on the uptake of C and F and on Si etching, values of 0.5, 0.75 and 1 fs were selected. In order to ensure a total energy drift during the collision of less than 0.1%, time steps greater than 1 fs could not be used. A shorter time step for a fixed overall integration time means a longer computation time. The calculations demonstrate that time steps ranging from 0.5 - 1 fs have little effect on the coverages of C and F or on the etching of Si (shown in figure 8(a-c)). Provided the overall energy of the system does not change significantly, the longest time step (1 fs) should be chosen in order to minimize the overall computation time.

During the integration period, the incident CF_3 may be adsorbed on the surface, scattered away or, in the case of collision-induced dissociation, some combination of sticking and scattering may occur. Removal of surface atoms may occur either by immediate sputtering or by chemical reaction to form molecules that are not strongly bound to the substrate. The total integration time of a single impact must be at least long enough to allow an incident molecule to complete its interaction (deposition of energy) with the surface. Once this criterion is satisfied, a longer integration time means, in effect, relaxation of the substrate for a longer interval between impacts (as opposed to the final relaxation outlined above). Figure 9(a), (b) and (c) shows that the coverage of C and F atoms and Si etch yield, respectively, as a function of exposure to CF_3 with integration times of 0.25, 0.5 and 1.0 ps per single impact. From the figure, we note that the simulation is not very sensitive to the integration time for the range studied. A significant difference should only occur if the integration time used is too short.

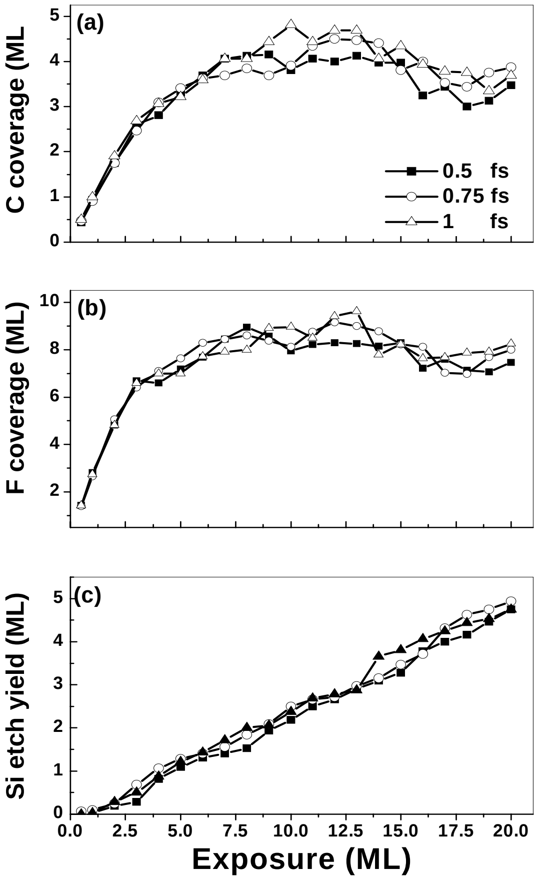

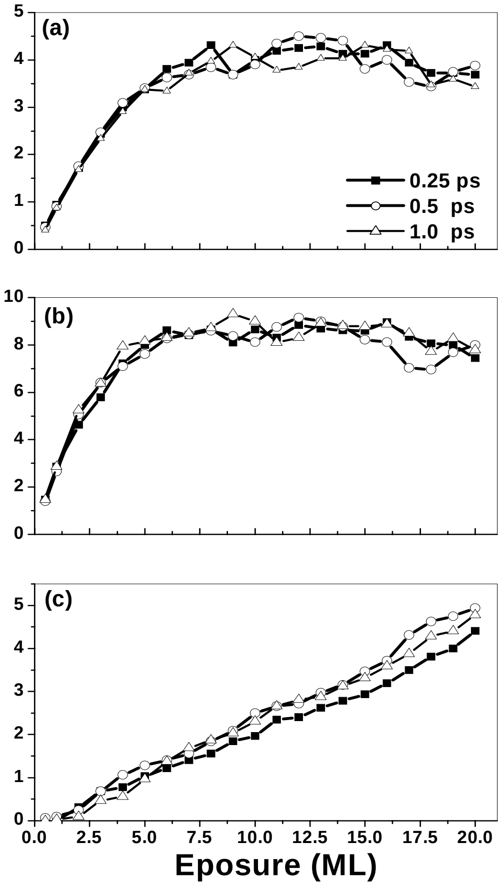

Figures 8: Coverages of C **(a)** and F **(b)** atoms on the sample as a function of exposure for three different integration time steps; **(c)** Si etching yield as a function of the exposure.

Figures 9: Coverages of C **(a)** and F **(b)** atoms on the sample as a function of exposure for three different total integration times; **(c)** Si etching yield as a function of the exposure.

8.2.6 Cell size effect

It is important to establish that the initial size of the simulated cell does not unduly influence the final results. Here we selected three initial configurations of 3x3x4, 4x4x6 and 5x 5x10 unit cell Si (100)-2x1 crystal consisted of 288, 768 and 2000 Si atoms with surface areas of ~200, ~500 and ~730 Å^2, corresponding to surface layer containing 18, 32 and 50 atoms, respectively. The corresponding sample depths are ~20, ~35 and ~55 Å. Figures 10(a) and (b) show the coverage of C and F atoms as a function of exposure. The difference in F coverage on the three samples is small over the course of the simulation. For the C coverage, during the early stages of deposition no difference is found between the different sample sizes. After ~5 ML, the curves begin to diverge. However, at higher exposure the curves reconverge. Figure 10(c) shows the etch yield of Si atoms as a function of exposure. The etch yield of Si atoms increases with increasing sample size. From the figure, the steady-state etch rates are ~0.16, ~0.26 and ~0.31 respectively.

In order to explain etching, three mechanisms have been proposed. One mechanism is chemically enhanced physical sputter, proposed by Mauer et al [66]. It is suggested that the formation of the volatile products (e.g. SiF_X) that are weakly bound to the surface enhances the physical sputtering of Si atoms. A second mechanism proposed by Tu et al is called chemical sputtering [67]. It suggests that ion bombardment induces a chemical reaction that produces weakly bound molecules that spontaneously desorbs from the surface. The third mechanism, which was originally suggested by Coburn et al. and later expanded upon by Flamm and Donnelly, is characterized as a damage-induced chemical reaction [9; 68]. It

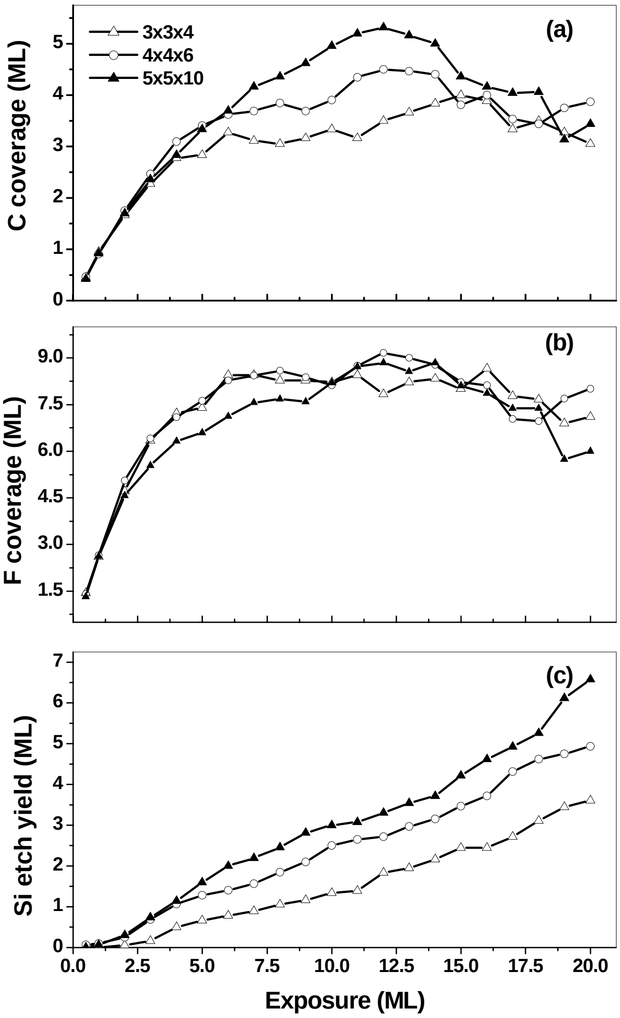

Figures 10: Coverages of **(a)** C and **(b)** F atoms on the sample as a function of exposure for the three sample sizes; **(c)** Si etching yield as a function of the exposure.

proposes that the lattice damage caused by ion bombardment results in enhancement of a chemical reaction on the surface. In practice, surfaces are damaged as a result of bombardment by energetic CF_3 and vacancies and holes are formed. During etching processes, these vacancies and holes allow incident CF_3 molecules to deposit kinetic energy deeper in the sample. In addition, more F atoms can be transported into the substrate and may react with Si to form weakly bound SiF_x species. These SiF_x species can desorb from the sample via the same vacancies through which the CF_3 entered. In MD simulations the application of periodic boundaries prohibits the formation of roughness on length scales larger than the cell size. With increasing cell size, the length-scale of surface roughness can increase and may play a role in enhancing the etching. Hence, the increasing etch rate with cell size shown in figure 10(c) can be attributed to the different length-scale roughness that may be generated.

8.3 Surface temperature effect

During collision of CF_3 with the surface, surface atoms (C, F and Si) may be sputtered as a direct result of momentum transfer (pure physical sputtering). In reaction ion etching (RIE), this mechanism plays a minor role. In addition, following dissociation some F atoms can react with Si or C atoms on the surface to form volatile products (such as CF_x or SiF_x species). These weakly bound products may subsequently gain energy from the collision cascade and be desorbed (chemically-enhanced physical sputtering) [66]. This mechanism suggests that the main role of energetic ions is to remove products during the collision cascade that follows ion impact and that reactive C and F atoms play an role in weakening the bonding prior to sputtering. This process competes with spontaneous desorption of weakly bound products (chemical sputtering [67]). In the current MD simulations a simple first-order thermal desorption model is used to predict when weakly bound species desorb spontaneously. When a cluster's binding energy with surface is smaller than a threshold energy computed from first-order thermal desorption theory [14], the cluster is considered to have desorbed from the surface. In the simulations, species matching this criterion are removed from the simulation after each trajectory. The threshold energy can be obtained from [14]:

$$E_b = k_b T \ln(\tau.A) \qquad \textbf{(10)}$$

where k_b is the Boltzmann constant, T is the surface temperature, τ is a time constant which is smaller than the real time that elapses before a subsequent molecule impacts and A is a constant. Any molecule that is bound to the surface by less than this value is regarded as a desorbing species. Following Abrams' model, in our simulations, we adopted $\tau=1$ μs and $A=10^{12}$ s^{-1}. From equation (10), the desorption energy limit increases with increasing the surface temperature. This means that at higher surface temperatures, weakly bound species are more readily desorbed from the surface. If a species is found with a binding energy to the surface that is less than E_b, it is defined as desorbing as a result of chemical sputtering. In order to characterize the effect of sample temperature on etching (physical and chemical), simulations were performed with surface temperatures of 100, 300, 600 and 800 K.

Figures 11(a) and (b) show the coverage of C and F atoms as a function of temperature for exposure to 100 eV CF_3. From figure 11(a), we note that the coverage of C atoms is most sensitive to the surface temperature. With increasing surface temperature, C atoms retention by the surface increases. In contrast, it is found that the coverage of F atoms is not very sensitive to the surface temperature. Figure 11(c) shows the etch yield of Si atoms as a function of exposure with different surface temperature. With increasing surface temperature, the etch yield increases. The steady-state etch rates are 0.199, 0.251, 0.275 and 0.373 for 100, 300, 600 and 800 K, respectively.

Figure 12 shows a breakdown of the chemical and physical etching yields as a function of temperature. It can be seen that the physical etching yield is greater than the chemical etching yield. With increasing temperature, both the chemical and physical yields increase. The chemical etching yield increases in a linear fashion by a factor of about 2. The physical etching yield increases sharply from 100 to 300 K. Above 300 K, the increase is more gradual.

Figure 13 shows the atomic densities in the sample as a function of depth at 300 and 800 K exposure to 40 ML of 100 eV CF_3. It can be seen that with increasing substrate temperature, the peaks of C and F shift toward the bulk. This arises as a result of the increasing etch rate with increasing temperature. Compared with the 300 K sample, the reaction layer at 800 K is broader. Both the C and F distribution are broader at higher surface temperature.

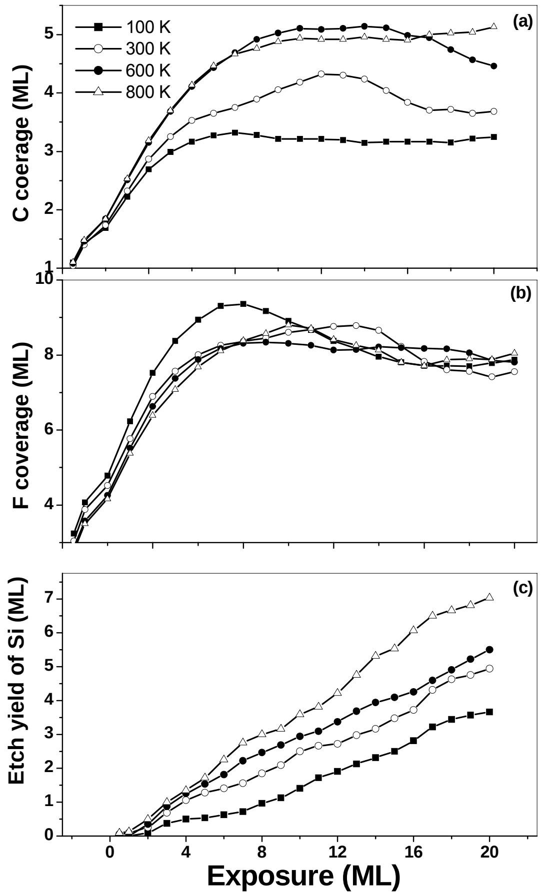

Figures 11: Coverages of **(a)** C and **(b)** F atoms on the sample as a function of exposure for different sample temperatures; **(c)** Si etching yield as a function of the exposure.

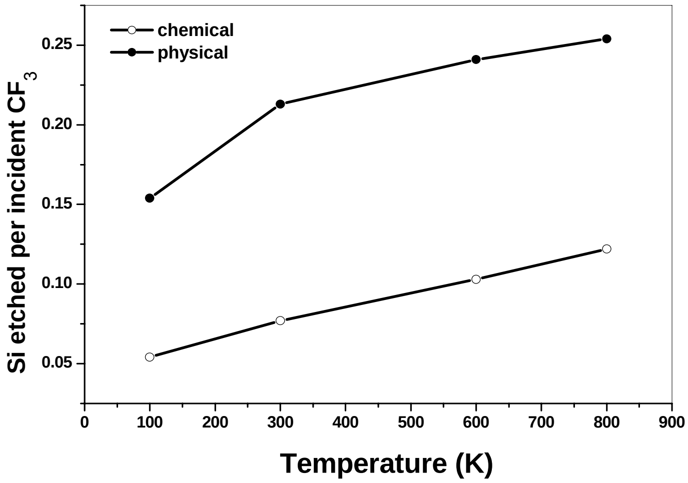

Figure 12: A breakdown of the chemical and physical etching yields as a function of temperature.

Figure 14 shows the yield of the different etch products as a function of temperature. From the figure, we note that the yields of SiF_2 and SiF_3 are strongly dependent on the surface

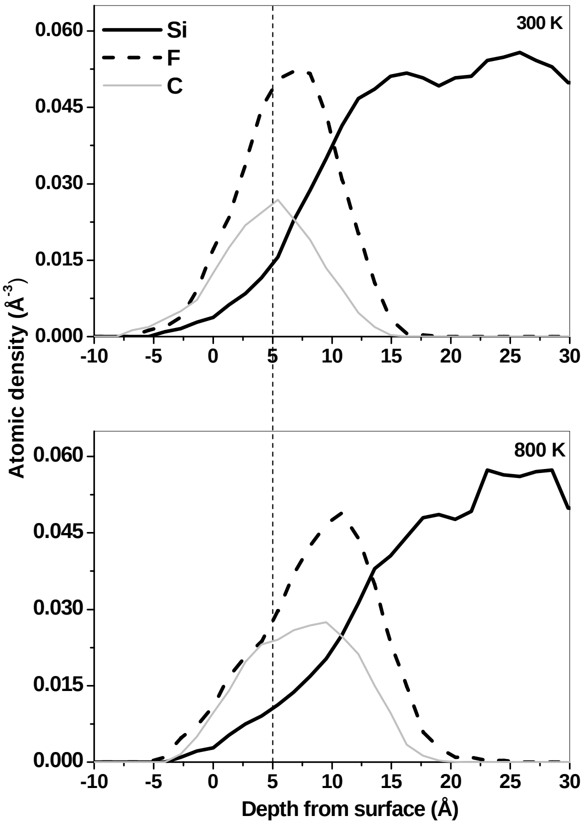

Figure 13: Atomic densities in the sample as a function of depth at 300 and 800 K after 40 ML exposure to 100 eV CF_3.

temperature, while SiF_4 is relatively insensitive. With increasing temperature, the yields of both SiF_2 and SiF_3 increase, while the yield of SiF_4 remains effectively constant. At low temperature, the yield of SiF_4 is greater than that of SiF_2 or SiF_3, while the yield of SiF_2 is the smallest. As the temperature increases, SiF_3 becomes the dominant etch product. At 800 K, the yield of SiF_2 is close to that of SiF_4, while the yield of SiF_3 is almost twice that of SiF_2. Figure 15 shows the yields of all ejected products, including those arising from the incident molecules (scattering). From the figure, we note that with increasing temperature, the yields of C_x (x=1-3) and F increase; the yield of CF remains almost constant; the yields of CF_2 and CF_3 decrease. The yields of larger molecules C_xF_y (x>1, y>0) and $Si_xC_yF_z$ (x,y, z >0) are effectively constant with temperature.

Figure 16 shows the desorbing yield of CF and CF_2 clusters as a function of exposure at 300 K. It can be seen that the yields of CF and CF_2 are almost identical prior to a steady state being established. However, at the steady state the yield of CF_2 is greater than that of CF. Figure 17 shows the yield of SiF_2, SiF_3 and SiF_4 etch products as a function of exposure at 300 and 600K. During the initial stages, the yield of SiF_2 increases sharply, reaches a maximum and then decreases toward a steady state. For SiF_3 and SiF_4, the yields increase more gradually as the simulation processes and then reach steady-states. These species have very weak or no maxima in their yield as a function of exposure. At low exposures (less than12 ML) the yield of SiF_2 is greater than that of SiF_3. After ~12 ML exposure, the yield of SiF_3 becomes the largest. Over the course of the simulations at 300 and 600 K, the yield of SiF_4 always remains the smallest. At 300 K, it is observed that when the yield of SiF_2 reaches

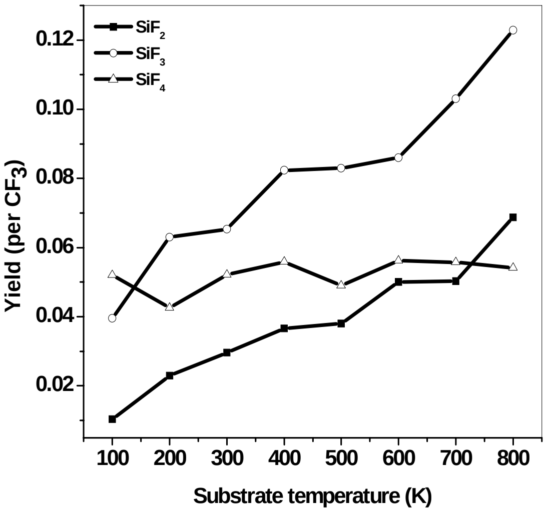

Figure 14: Yield of the different etch products as a function of temperature.

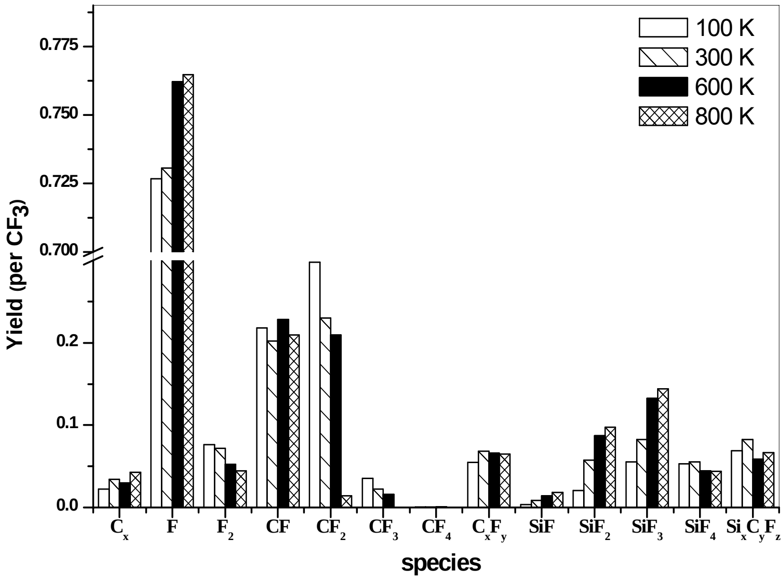

Figure 15: Yield of all ejected products, including those arising form the incident molecules

its maximum, SiF_3 and SiF_4 molecules start to appear, while at 600 K, SiF_2 and SiF_3 are produced simultaneously. After 2.5 ML exposure, SiF_4 molecules start to emerge.

8.4 Discussion

MD simulations were performed to investigate the effect of substrate temperature on etching. With increasing temperature, the uptake of F atoms is not sensitive to the substrate temperature, while the Si etching yield increases. Hence elevating the substrate temperature

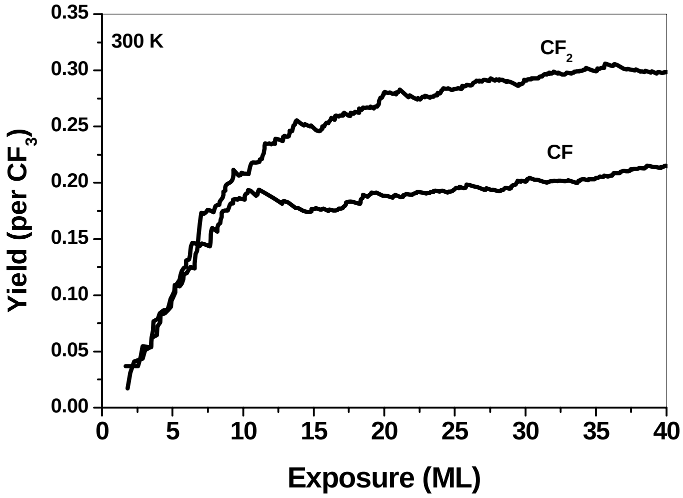

Figure 16: Desorbing yield of CF and CF$_2$ clusters as a function of exposure at 300 K.

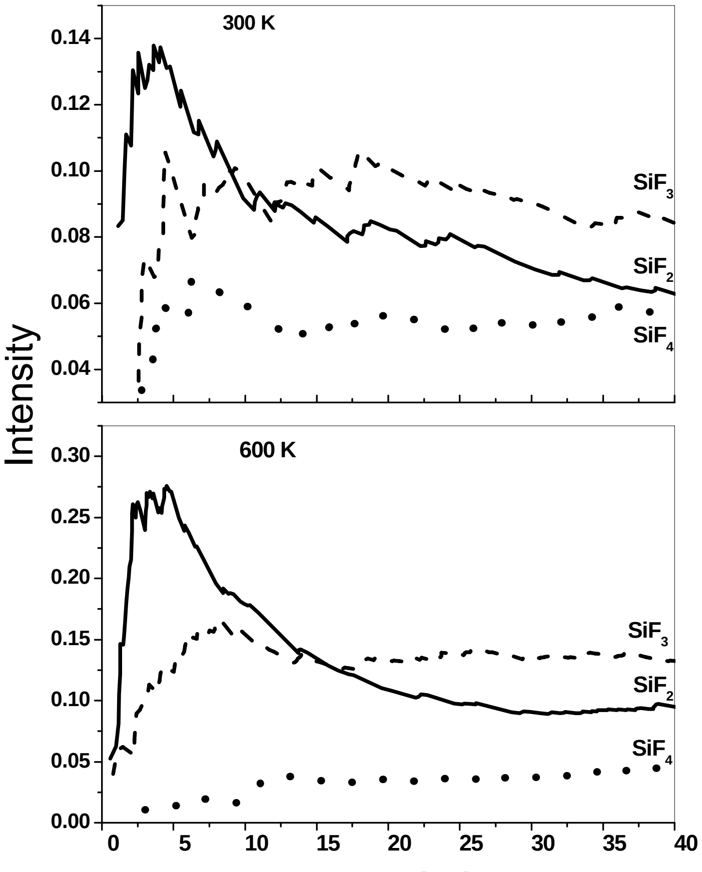

Figure 17: Yield of SiF$_2$, SiF$_3$ and SiF$_4$ etch products as a function of exposure at 300 and 600K.

enhances the etch efficiency, or conversely, at higher temperatures fewer F atoms are required to achieve the same etch rates.

In the simulations, with increasing substrate temperature the etch yields of SiF$_3$ and SiF$_2$ increase, while the saturated SiF$_4$ species is almost independent of the substrate temperature. The increased Si etch yield is mainly contributed by increased desorption of the unsaturated SiF_2 and SiF_3 species. This behavior was experimentally observed by Winters and Coburn using mass spectrometry during Si etching with XeF_2 [9]. In their experiments they observed that when the substrate temperature was increased from room temperature to 600 K, Si etching was enhanced and unsaturated SiF_2 species were desorbed. Sebel et al. performed Ar^+-assisted Si etching by XeF_2 in the temperature range T = 150-800 K [69]. They also reported that the etch rate was enhanced with increasing substrate temperature. In our simulations, the etching rate increases from 0.199 to 0.373 when the temperature is increased from 100 K to 800 K. A number of studies have demonstrated that the substrate temperature affects the desorbing species during etching [9; 70]. Humbird et al. performed MD simulations of spontaneous etching of silicon by F atoms and also observed that same behavior [47; 48]. These authors propose that at higher temperatures the SiF_x layer begins to spontaneously decompose to produce SiF_2 species that may desorb from the surface. Humbird et al. also pointed out that, since MD simulation only can capture events on picoseconds timescales, the simulations will tend to under-estimate the production of SiF_2 species relative to experiments. This under-estimation is also observed in our simulations for 100 eV CF_3 bombardment, since SiF_2 species are not the main product. This is because in the simulation, we shoot 100 eV CF_3 rapidly one after another with no interval time between two sequential impacts. In reality, the interval time on such a sample area is roughly a millisecond. In addition, for the simulation at higher energies the total integration time is shorter. Therefore, spontaneous decomposition of SiF_x species is limited resulting in SiF_3 species being dominant (SiF_2 less than SiF_3).

Toyoda et al. investigated energy-controlled and mass-selected CF_3 ions interacting with Si surfaces [71]. They measured the time evolution of neutral radicals desorbed from the surface by appearance mass spectrometry. The yield of CF_2 increased monotonically with exposure to CF_3 until a steady state was reached. They found that the SiF_2 desorption reached its maximum at about 3 ML exposure. Subsequently, the SiF_2 desorption decreased and reached a steady state after about 40 ML exposure.

Both physical and chemical erosion mechanisms are increased by elevating the sample temperature, with the chemical process showing the greatest enhancement in relative terms. Barone and Graves used MD simulations to investigate characteristics of chemical and physical sputtering of fluorinated silicon [39]. In their simulations, fluorinated reaction layers with varying F/Si ratios were fabricated by bombarding the silicon surface with F. These layers were then subjected to energetic Ar^+ bombarding. They concluded that at low F/Si ratio ($F/Si < 0.5$) only enhanced physical sputtering was observed. However, at ratios of $F/Si > 0.5$ in the fluorinated layer a chemical sputtering mechanism appeared to be dominant. Humbird and Graves performed MD simulations to study argon-ion-assisted etching of silicon by F radical. They concluded that two mechanisms (chemically enhanced physical sputtering and chemical sputtering) play an important role in etching [47]. In our cases, for 100 eV CF_3 interacting silicon surfaces F atoms plays two roles. During the collision cascade, F atom reacts with Si atoms to weaken the bonds. Simultaneously, F and C atoms transfer some their momentum to the surface atoms and induce physical sputtering. It is calculated that the energy deposition of CF_3 incident molecules in the layer was concentrated near surface region [39]. The deposited energy may be used to redistribute F atoms on the surface to deeper layers to react with Si atoms and subsequently to transport the resulting SiF_x to the surface. Compared to the thermal desorption energy, at 100 eV the deposited energy around the impacting site is much larger. Therefore, at 100 eV pure chemical sputtering is limited and the chemically enhanced physical sputtering mechanism is dominant.

8.5 Conclusion

MD simulations have been performed to investigate CF_3 molecules interacting with Si (100) surfaces. The Tersoff-Brenner potential was selected. We mainly discussed effects of the temperature control (the application time of the heat bath, the rising time), the relaxation time of the postbombarded sample, the cell size, the time step and the integration time on the etching. The simulation results show that the application time and the cell size have effects on etching. The other factors have no major influence on etching. Finally, the effects of the substrate temperate on etching have been investigated. With increasing the substrate temperature, the etching rate increases, which is in good agreement with the available experiments. The increased etch yield with increasing temperature is mainly due to the increased desorption of etch products SiF_2 and SiF_3 species. It was also found that the SiF_3 is the dominant etching species.

References

[1] J. A. Bondur, Journal of Vacuum Science and Technology 13 (1976) 1023.
[2] L. A. Brussaard, A. Fasolino, T. Janssen, Phys. Rev. B 63 (2001) 214302.
[3] J. P. Chang, J. W. Coburn, J. Vac. Sci. Technol. A 21 (2003) S145.
[4] T. P. Chow, A. J. Steckl, J. Electrochem. Soc. 131 (1984) 2325.
[5] J. W. Coburn, Vacuum 38 (1988) 947.
[6] V. M. Donnelly, D. L. Flamm, D. E. Ibbotson, J. Vac. Sci. Technol. A 1 (1983) 626.
[7] H. W. Lehmann, J. Vac. Sci. Technol. B 6 (1988) 1881.
[8] R. G. Poulsen, Journal of Vacuum Science and Technology 14 (1977) 266.
[9] H. F. Winters, J. W. Coburn, Surf. Sci. Rep. 14 (1992) 161.
[10] G. S. Oehrlein, M. F. Doemling, B. E. E. Kastenmeier, P. J. Matsuo, N. R. Rueger, M. Schaepkens, T. E. F. M. Standaert, Ibm. J. Res. Dev. 43 (1999) 181.
[11] E. S. Aydil, R. A. Gottscho, Y. J. Chabal, Pure & Appl. Chem (1994) 34.
[12] C. F. Abrams, D. B. Graves, J. Vac. Sci. Technol. A 19 (2001) 175.
[13] C. F. Abrams, D. B. Graves, J. Vac. Sci. Technol. A 16 (1998) 3006.
[14] C. F. Abrams, D. B. Graves, J. Appl. Phys. 86 (1999) 5938.
[15] C. F. Abrams, D. B. Graves, J. Appl. Phys. 88 (2000) 3734.
[16] C. F. Abrams, D. B. Graves, J. Vac. Sci. Technol. A 18 (2000) 411.
[17] M. E. Barone, D. B. Graves, J. Appl. Phys. 78 (1995) 6604.
[18] D. W. Brenner, Phys. Rev. B 42 (1990) 9458.
[19] F. Gou, M. A. Gleeson, A. W. Kleyn, PCCP 8 (2006) 5522.
[20] B. A. Helmer, D. B. Graves, J. Vac. Sci. Technol. A 15 (1997) 2252.
[21] D. Humbird, D. B. Graves, J. Chem. Phys. 120 (2004) 2405.
[22] I. K. Jang, S. B. Sinnott, J. Phys. Chem. B 108 (2004) 18993.
[23] L. W. Keri, I. B. Carmen, R. F. Ellen, J. Vac. Sci. Technol. A 21 (2003) 1688.
[24] M. G. Luca, H. L. Jan, A. Fasolino, M. Evert Jan, Phys. Rev. B 72 (2005) 214103.
[25] C. T. Reeves, B. A. Ferguson, C. B. Mullins, G. O. Sitz, B. A. Helmer, D. B. Graves, J. Chem. Phys. 111 (1999) 7567.
[26] T. A. Schoolcraft, A. M. Diehl, A. B. Steel, B. J. Garrison, J. Vac. Sci. Technol. A 13 (1995) 1861.
[27] V. V. Smirnov, A. V. Stengach, K. G. Gaynullin, V. A. Pavlovsky, S. Rauf, P. J. Stout, P. L. G. Ventzek, J. Appl. Phys. 97 (2005).

[28] F. H. Stillinger, T. A. Weber, Phys. Rev. Lett. 62 (1989) 2144.
[29] F. H. Stillinger, T. A. Weber, J. Chem. Phys. 88 (1988) 5123.
[30] T. A. Weber, F. H. Stillinger, J. Chem. Phys. 92 (1990) 6239.
[31] T. A. Weber, F. H. Stillinger, J. Chem. Phys. 95 (1991) 3614.
[32] K. C. Fang, C. I. Weng, Nanotechnology 16 (2005) 250.
[33] M. Han, T. Li, X. Z. Yang, Chem J Chinese U 26 (2005) 960.
[34] N. Jakse, Y. Kadiri, J. L. Bretonnet, Phys Rev B 61 (2000) 14287.
[35] Y. R. Jeng, P. C. Tsai, T. H. Fang, Nanotechnology 15 (2004) 1737.
[36] H. Ohta, S. Hamaguchi, J. Chem. Phys. 115 (2001) 6679.
[37] Y. Sano, J. Koga, F. Yonezawa, J Optoelectron Adv M 7 (2005) 1915.
[38] B. Weber, K. Gartner, Nucl. Instrum. Methods Phys. Res., Sect. B 175 (2001) 119.
[39] M. E. Barone, D. B. Graves, J. Appl. Phys. 77 (1995) 1263.
[40] J. Tersoff, Phys. Rev. Lett. 61 (1988) 2879.
[41] J. Tersoff, Phys. Rev. B 38 (1988) 9902.
[42] J. Tersoff, Phys. Rev. B 39 (1989) 5566.
[43] J. Tersoff, Phys. Rev. B 37 (1988) 6991.
[44] J. Tersoff, Phys. Rev. Lett. 56 (1986) 632.
[45] D. W. Brenner, O. A. Shenderova, J. A. Harrison, S. J. Stuart, B. Ni, S. B. Sinnott, Journal of Physics-Condensed Matter 14 (2002) 783.
[46] B. A. H. Huisman, A. Fasolino, Phys. Rev. E 72 (2005) 016107.
[47] D. Humbird, D. B. Graves, J. Vac. Sci. Technol. A 23 (2005) 31.
[48] D. Humbird, D. B. Graves, J. Appl. Phys. 96 (2004) 791.
[49] D. Humbird, D. B. Graves, Plasma Sources Sci. Technol. 11 (2002) A191.
[50] D. Humbird, D. B. Graves, J. Appl. Phys. 96 (2004) 65.
[51] D. Humbird, D. B. Graves, J. Chem. Phys. 120 (2004) 2405.
[52] D. Humbird, D. B. Graves, Pure Appl. Chem. 74 (2002) 419.
[53] D. Humbird, D. B. Graves, J. Appl. Phys. 96 (2004) 2466.
[54] D. Humbird, D. B. Graves, Ieee. T. Plasma. Sci. 33 (2005) 226.
[55] D. Humbird, D. B. Graves, Plasma Sources Sci. Technol. 13 (2004) 548.
[56] D. Humbird, D. B. Graves, X. F. Hua, G. S. Oehrlein, Appl. Phys. Lett. 84 (2004) 1073.
[57] J. Tanaka, C. F. Abrams, D. B. Graves, J. Vac. Sci. Technol. A 18 (2000) 938.
[58] F. Gou, M. A. Gleeson, A. W. Kleyn, Surf. Sci.601 (2007) 76.
[59] F. Gou, M. A. Gleeson, J. Villette, A. W. Kleyn, Nucl. Instrum. Methods Phys. Res., Sect. B 247 (2006) 244.
[60] H. C. Andersen, J. Chem. Phys. 72 (1980) 2384.
[61] S. Nose, M. L. Klein, Phys. Rev. B 33 (1986) 339.
[62] S. Nose, M. L. Klein, Phys. Rev. Lett. 53 (1984) 818.
[63] S. Nose, J. Chem. Phys. 81 (1984) 511.
[64] H. J. C. Berendsen, J. P. M. Postma, W. F. v. Gunsteren, A. DiNola, J. R. Haak, J Chem Phys 81 (1984) 3684.
[65] D. B. Graves, D. Humbird, Appl. Surf. Sci. 192 (2002) 72.
[66] J. L. Mauer, J. S. Logan, L. B. Zielinski, G. C. Schwartz, J. Vac. Sci. Technol. 15 (1978) 1734.
[67] Y.-Y. Tu, T. J. Chuang, H. F. Winters, Phys. Rev. B 23 (1981) 823.
[68] D. L. Flamm, V. M. Donnelly, D. E. Ibbotson, J. Vac. Sci. Technol. B 1 (1983) 23.
[69] P. G. M. Sebel, L. J. F. Hermans, H. C. W. Beijerinck, J. Vac. Sci. Technol. A 18 (2000) 2759.
[70] K. L. Williams, E. R. Fisher, J. Vac. Sci. Technol. A 21 (2003) 1024.
[71] H. Toyoda, H. Morishima, R. Fukute, Y. Hori, I. Murakami, H. Sugai, J. Appl. Phys. 95 (2004) 5172.

Summary

Over the past thirty years, plasma has become a very useful means of depositing or removing small quantities of material at a variety of substrates quickly and efficiently. Plasma etching processes have been used in many highly sensitive integrated circuit packaging and optoelectronic applications to precisely remove specific materials from sample surfaces. Because of the complexity of the plasma itself and the strong coupling between surface and plasma, most conventional surface analytical techniques can not be utilized in a plasma environment. The majority of experimental measurements have involved either directed beam studies so as to be representative of a reactive gas plasma environment or ex-situ characterization of plasma-exposed surfaces vacuum that are transferred from the plasma environment to conventional surface analytical instrumentation. In order to fully understand the etching mechanism, it is essential to develop new techniques to characterize in-situ and real-time interactions between plasma and surfaces. In the past decade, with the remarkable improvement of the computational performance of supercomputers, large scale molecular dynamics (MD) simulations have become a valuable tool for understanding microscopic dynamics at the atomic level that are particularly difficult to observe experimentally. In this thesis, we introduce a low energy ion grazing scattering technique for characterization real-time and in-situ of interactions between plasma and surfaces. MD simulations are undertaken to understand the dynamics of low energy ion grazing scattering from surfaces (smooth and rough), as well as deposition and etching occurring at surfaces during plasma etching processes.

At grazing angles, incident particles can travel a long distance parallel to the surface, while not penetrating very deep into the sample. The projectile trajectories are highly sensitive to both short- and long-range lateral surface structure. Consequently, grazing incident scattering is potentially a good technique for monitoring the modification of surfaces in real-time. We have built a new TOF instrument to study plasma-treated surfaces in real-time and in-situ by means of grazing incidence ion scattering and seek to understand the dynamics of plasma-surface interactions. The instrument uses a mass-selected and velocity-selected ion beam at grazing incidence as a surface probe. Real-space and real-time profiles of

scattered particles are derived from the output of a position sensitive detector. From these 2D profiles, energy and angular distributions of scattered ions and neutrals are obtained. Changes in the energy and angular distribution as a function of time can be used to monitor real-time and in-situ the interaction between plasma and surfaces. The results for Ar^+ scattering from Si (100) surfaces subject to different pre-treatments demonstrate that the technique is suitable for use as a surface analytical tool in a plasma environment.

MD simulations of grazing scattering of Ar from Si (100) surfaces show that the binary collision approximation model is not entirely suited to describing the interaction between particles and surface atoms under grazing scattering. This is due to the scattering process in many cases involving a number of simultaneous collisions between projectile and target atoms. Surface channeling shown in chapter 3 and 4 is strongly sensitive to the incidence angle. With increasing incidence angle with respect to the surface plane the scattering mechanism changes from planar- to hyper- to sub-surface channeling. The energy loss and angular distributions are sensitive to the impact points and rainbow scattering under surface channeling can be observed Compared with the energy loss experienced in experiments with the same scattering geometry, the energy loss excluding the electron stopping is negligible. Experimentally, the bulk of energy lost during scattering at grazing incidence is a result of inelastic energy loss processes. An electron-stopping model is included in the simulations to account for such inelastic processes.

During plasma processing, defects are created. Under grazing incidence, the projectile should be sensitive to the defects existing on the surface. MD simulations of Ar scattering from point-defected Si(100) surfaces at grazing incidence demonstrate that the angular and energy distributions of the scattered particles are extremely sensitive to small adatom coverages.

Under grazing conditions, molecules with a large total energy can have normal energies of less than 10 eV. Such energies are typical for the activation of chemical reactions at surfaces. MD simulations show that results obtained for grazing incidence (e.g. internal energy uptake and dissociation rate as a function of normal energy) are qualitatively applicable to less grazing geometries. This is highly advantageous when seeking to study the interaction of low energy (1-50 eV) particles with surfaces due to a relative lack of adequate beam sources and efficient detectors. For surviving molecules, after impact with the surface, only a small fraction of the energy lost is transferred to internal energy. At the classical turning point, the internal energy of the molecule is mainly in form of rotational energy. The strong rotational excitation results in additional molecule-surfaces interactions during the latter half of the collision. These additional collisions permit some molecules that initially gain internal energy exceeding the bond strength to ultimately survive the collision process via rotational de-excitation. The rotational motion exhibited by surviving molecules is determined by the combination of the molecular axis orientation and the local surface structure during the collision process. The rotation planes of the surviving molecules are preferentially aligned with the surface normal (cartwheel-like and propeller-like motions). The stereodynamics of the surviving molecules are consistent with propeller-like and cartwheel-like motions The majority of surviving molecules exhibit a cartwheel-like motion. However, molecules that gain a propeller-like rotation exhibit a much better alignment of their planes of the rotation compared with molecules exhibiting cartwheel-like motion. Therefore, molecular ion scattering at grazing incidence can be sued to study interactions of components of etch plasma and solid surfaces.

In plasma etching, ions play an important role. A number of theoretical studies have indicated that nearly all incident ions will be neutralized within a few atomic radii of the surface as a result of Auger emission process. Thus, the majority of the particle actually striking surfaces in contact with a plasma are neutral species. Studies show that in fluorocarbon plasma etching CF_3 molecules play a role in etching while CF molecules play a role in deposition. In order to fully understand plasma etching processes, a fundamental knowledge of CF interacting with Si surfaces is need. MD simulations of the CF interaction show that C atoms, arising from dissociation, preferentially react with Si to form Si-C bonds. A $Si_xC_yF_z$ interfacial layer is formed, but no etching is observed. The interfacial layer thickness increases with increasing incident energy, mainly through enhanced penetration of the silicon lattice. Silicon carbide and fluorosilyl species are formed at 50 eV, which is in good agreement with available experimental data.

Hydrocarbon thin films deposited by plasma-enhanced chemical vapor deposition (PECVD) are important for many applications. The diamond-like films produced are widely used as wear-resistant coatings. In ITER, the chemical erosion of graphite (used as wall material) will result in the redeposition of hydrocarbon on the wall. Therefore, investigating hydrocarbon interaction with surfaces is timely and significant. The MD simulations in chapter 7 shows that below 100 eV incident energies the H/C ratio obtained from the simulations is strongly sensitive to the energy and while above 100 eV, the ratio is not sensitive to the incident energy, which is in good agreement with available experimental data. After CH_3 dissociation and adsorption, H atoms preferentially react with Si. In the interfacial layer, SiH is the dominant form of SiH_x generated. The amount of hydrogen that reacts with silicon is essentially energy-independent.

In conclusion, the grazing scattering technique is a viable tool for in-situ monitoring of surface processes occurring during plasma treatment. MD simulations provide an atomic level picture to aid the interpretation of experimental data and to gain insight into the interaction mechanism between ions and surfaces.

Samenvatting

In de afgelopen dertig jaar is plasma een goed medium geworden om kleine hoeveelheden materiaal te deponeren of weg te etsen van verschillende typen oppervlakken. De methode is snel en efficiënt. Plasma etsen wordtgebruikt in vele complexe processen in de vervaardiging van geïntegreerde schakelingen en opto-elektronische componenten. Specifieke materialen kunnen selectief worden verwijderd. Vanwege de complexiteit van het plasma zelf en de sterke wisselwerking tussen oppervlak en plasma kunnen de meeste gebruikelijke methoden voor analyse van oppervlakken niet worden gebruikt in de aanwezigheid van plasma. De meeste metingen, die zijn uitgevoerd, betreffen onderzoek met gerichte plasma bundels om zo het normaal gebruikte plasma na te bootsen of betreffen metingen die ex-situ met conventionele methoden worden uitgevoerd. Om het ets mechanisme goed te begrijpen is het nodig om nieuwe methoden te ontwikkelen, die in-situ en tijdens bedrijf ('real time') werken.

In het afgelopen decennium is de rekenkracht van supercomputers enorm toegenomen. Daardoor is het mogelijk geworden om grootschalige moleculaire dynamica (MD) berekeningen aan plasma etsreacties uit te voeren. Op die manier kan inzicht worden verkregen in de atomaire dynamica, die zeer moeilijk experimenteel is waar te nemen. In dit proefschrift wordt lage energie ionen verstrooiing geïntroduceerd om de wisselwerking tussen plasma en oppervlakken tijdens bedrijf te karakteriseren. MD-berekeningen zijn uitgevoerd om de verstrooiing van ionen aan (vlakke en ruwe) oppervlakken te begrijpen. Daarnaast is de dynamica van depositie en etsreacties gedurende een plasma behandeling bestudeerd. Bij scherende inval kunnen deeltjes lange afstanden langs het oppervlak afleggen zonder in de vaste stof te penetreren. De deeltjesbanen zijn zeer gevoelig voor de structuur van het oppervlak. Daarom is verstrooiing bij scherende inval een goede methode om veranderingen van het oppervlak te detecteren. Wij hebben een nieuw apparaat ontwikkeld om veranderingen van oppervlakken als functie van de tijd te bestuderen, en om de wisselwerking tussen plasma en het oppervlak te begrijpen. Het apparaat gebruikt een massa- en snelheidsgeselecteerde ionenbundel, die scherend invalt, als sonde van het oppervlak. De verstrooiingsprofielen van de deeltjes worden bepaalt met een plaats- en tijdgevoelige detector. Veranderingen in de profielen worden gebruikt om de wisselwerking van plasma en oppervlak te bepalen. De resultaten voor Ar^+ verstrooiing aan Si (100), dat op verschillende manieren behandeld is, laten zien dat de techniek aan de gestelde eisen kan voldoen.

MD simulaties van verstrooiing van scherend invallend Ar (of Ar^+) laten zien dat de veel gebruikte binaire botsingsbenadering met geschikt is om de verstrooiing te beschrijven. Dit komt, omdat simultane botsingen optreden in de baan van het Ar langs het oppervlak. Verstrooiing in kanalen langs het oppervlak, zoals besproken in de hoofdstukken 3 en 4, is zeer gevoelig voor de hoek van inval. Met toenemende hoek verandert het karakter van planaire verstrooiing naar verstrooiing van dieper gelegen banen. He energieverlies en de hoekverdelingen zijn gevoelig voor waar het oppervlak wordt geraakt en regenboog verstrooiing kan worden waargenomen. Vergeleken met de experimentele waarden is het energieverlies in de MD-berekeningen zeer klein. Dit komt omdat afremming door het elektronengas in de berekeningen niet wordt meegenomen. In het experiment bepaalt dit proces voornamelijk het energieverlies. Het kan in de berekeningen worden meegenomen en in dat geval wordt goede overeenstemming met de metingen worden verkregen.

Tijdens de blootstelling van et oppervlak aan het plasma kunnen defecten in het oppervlak worden gecreëerd. MD-simulaties van Ar verstrooid aan puntdefecten op een Si(100) oppervlak laten zien, dat de hoek- en energieverdelingen van de verstrooide Ar zeer gevoelig zijn voor de aanwezigheid van ad-atomen in kleine concentratie.

Bij scherende inval kunnen moleculen met hoge totale translatie-energie een zogenaamde loodrechte energie hebben, die kleiner is dan 10 eV. Dit soort energie is typisch benodigd om chemische reacties aan het oppervlak te activeren. De MD-simulaties laten zien dat resultaten behaald voor scherende inval (bijvoorbeeld de opname van interne energie en dissociatie als functie van de loodrechte energie) kwalitatief ook kunnen worden gebruikt bij de interpretatie van interacties bij minder scherende inval maar met dezelfde loodrechte energie. Dit is zeer gunstig omdat interacties bij loodrechte energieën van 10-50 eV zeer moeilijk bij loodrechte inval bestudeerd kunnen worden, omdat de vereiste bronnen en detectoren niet voorhanden zijn. Voor moleculen, die de botsing met het oppervlak zonder te dissociëren overleven, is maar een heel klein gedeelte van de totale translatie-energie omgezet in interne energie. Op het klassieke omkeerpunt in de baan is de meeste interne energie in het molecuul aanwezig als rotatie-energie. Deze sterke rotatie-excitatie resulteert in extra molecuul-oppervlakte interacties gedurende de tweede helft van de botsing. Deze interacties maken het mogelijk om moleculen, die aanvankelijk een interne energie gekregen hebben, die groter is dan de dissociatie-energie, deze excitatie kwijt te laten raken en de botsing als molecuul te laten overleven. De rotatiebeweging van deze moleculen wordt bepaald door de oriëntatie van de moleculaire as voor de botsing en de lokale structuur van het oppervlak bij de botsing. De vlakken van rotatie van deze moleculen zijn bij voorkeur langs de oppervlaktenormaal georiënteerd, met zogenaamde wagenwiel of propeller beweging. De stereo-dynamica van de overlevende moleculen (besproken in hoofdstuk 5) is consistent met het optreden van deze wagenwiel of propeller beweging. Echter, moleculen met een propeller excitatie laten een veel betere oplijning van het rotatievector zien dan moleculen met een wagenwiel rotatie. Doordat de interactie in zoveel detail met MD kan worden bestudeerd is de verstrooiing van moleculaire ionen bij scherende inval een goede methode om de interacties van moleculen in etsplasma en oppervlakken te bepalen.

Bij plasma-etsen spelen ionen een belangrijke rol. Een aantal theoretische studies heeft laten zien dat bijna alle ionen op afstanden van een fractie van een nanometer geneutraliseerd worden in een Auger-proces. Daarom raken de meeste deeltjes uit het plasma het oppervlak als neutrale deeltjes, Onderzoek heeft laten zien, dat CF_3 moleculen een belangrijke rol spelen in etsreacties, terwijl CF moleculen van belang zijn voor depositie. Om plasma-etsen goed te begrijpen is fundamentele kennis van deze moleculaire interacties nodig. MD-simulaties van de interactie van CF moleculen in hoofdstuk 6 en 8 laten zien, dat C-atomen, afkomstig van moleculaire dissociatie, preferentieel met Si reageren om Si-C bindingen te vormen. Ook wordt de vorming van een $Si_xC_yF_z$ bufferlaag waargenomen, maar etsen treedt niet op. De dikte van de gevormde bufferlaag neemt toe met de botsingsenergie van het CF, voornamelijk wegens toegenomen penetratie van het oppervlak. Silicium carbide en en fluorosilyl verbindingen worden gevormd bij een primaire energie van 50 eV. Dit laatste is in goede overeenstemming met experimentele resultaten.

Films van koolwaterstoffen gedeponeerd met plasma-versterkte chemische damp depositie zijn relevant voor vele toepassingen. Diamantachtige films worden veel gebruikt als slijtvaste beschermingslaag. In de fusie reactor ITER is de chemische erosie van grafiet (gebruikt als wandmateriaal) resulteert in depositie van koolwaterstoffen op de wanden. Daarom is het bestuderen van de wisselwerking van koolwaterstoffen en oppervlakken van belang. De MD-simulaties in hoofdstuk 7 laten zien dat bij een ionenenergie van minder dan 100 eV de H/C verhouding in de simulaties sterk afhangt van de energie. Boven de 100 eV verdwijnt deze afhankelijkheid, wat ook in experimenten is waargenomen. Na CH_3 dissociatie and adsorptie, Reageren de gevormde H-atomen voornamelijk met Si. In de gevormde laag is SiH de meest voorkomende vorm van SiHx. De hoeveelheid waterstof, die met Si in het oppervlak reageert, is onafhankelijk van de energie.

Samenvattend is verstrooiing bij scherende inval een waardevolle techniek om ter plekke de processen aan het oppervlak te bestuderen, terwijl het etsplasma actief is. MD-simulaties geven een beeld op atomaire schaal wat het mogelijk maakt de experimentele resultaten in detail te analyseren en zo meer begrip te krijgen van het mechanisme van de wisselwerking tussen oppervlakken en ionen afkomstig uit plasma.

List of publications

This thesis is based on the following publications

Chapter 2

F. Gou, M. A. Gleeson, J. Villette, and A. W. Kleyn,
A new time-of-flight instrument capable of in situ and real-time studies of plasma-treated surfaces
Vacuum, 81, 2006, P196-201

Chapter 3

F. Gou, M. A. Gleeson, J. Villette, and A. W. Kleyn,
3 keV Ar scattering from unreconstructed Si(100) at grazing incidence: Molecular dynamics simulation
Nuclear Instruments and Methods in Physics Research B, 247, 2006, P244-253

Chapter 4

F. Gou, M. A. Gleeson, A. W. Kleyn,
MD simulation of Ar scattering from defected Si (100) at grazing incidence
Accepted by *NIMB*

Chapter 5

F. Gou, M. A. Gleeson, A. W. Kleyn,
Theoretical modeling of energy redistribution and stereodynamics in CF scattering from Si (100) under grazing incidence
Physical Chemistry Chemical Physics, 8, 2006, P5522 – 5534.

Chapter 6

F. Gou, M.A. Gleeson and A.W. Kleyn,
CF interaction with Si (100)-(2×1): Molecular dynamics simulation
Surface Science, 601 (2007) P76--86

Chapter 7

F. Gou, M. A. Gleeson, A. W. Kleyn,
Molecular dynamics simulation of CH_3 interaction with Si (100) surface
Accepted by *Surface Science*

Chapter 8

Part of the contents of this chapter will be published as
F. Gou, M. A. Gleeson, A. W. Kleyn,
Effects of Temperature on CF_3 interacting Si (100)-(2x1): Molecular Dynamics Simulation. In prepation

In addition, the following papers are not included as a part of the thesis

F. Gou , M. A. Gleeson , J. Villette , S. E. F. Kleyn and A. W. Kleyn
The surface of 1-euro coins studied by X-ray photoelectron spectroscopy
Applied Surface Science, 225, 2004, P 47-53

F. Gou, M. A. Gleeson, A. W. Kleyn,
CF_3 interaction with Si (100)-(2x1): Molecular Dynamics Simulation.
Accepted by *surface Science*

F. Gou, M. A. Gleeson, A. W. Kleyn,
CF_3 interaction with fluorinated silicon surface: Molecular Dynamics Simulation.
In preparation

Acknowledgements

There are so many people who have affected me during my stay in the Netherland that it is impossible to acknowledge every one of them. Please forgive me if forgot to mention somebody personally, I am thankful to you all.

I wish to first and most importantly, thank my advisors, Gleesson and Jerome, for guiding me during the ups and downs of research. In particular, under Jerome's guidance, I know about the building of UHV setup and data acquisition systems. I miss very much our exciting discussions of our simulation results. From these discussions, my simulations were gradually improved and were deeply understood. You have helped me to think critically and have provided excellent research help.

I would like to thank Rob van Schie, John Bakker and Peter Schakel for their technical help. I greatly appreciate the guidance of Dr Roar A. Olsen and Dr. Franco Buda. During my thesis, who taught me how to use the DFT method to construct the empirical potentials.

I am very grateful to all my colleagues: Aart, Misha, Ellen, Ludo, Mihail, Slyvie, Emile in Leiden University. My thanks to Niek, Goedheer, Gerard, Kopper, Bart, Victor Land, Shumack, Dagmar, Hans in PSI department in the institute. Many Thanks also to Fred, Robert , Eric and other members in nSI department. Many thanks to I.H. Vörös, who help me find many useful research papers. Many thanks to Renate for her great help.

I have also met my wife here. Thanks you for all of your support. And I thank my parents for prodding me along to finish my work here.

Curriculum Vitae

Fujun Gou was born in 1969 in Chengdu, China. In 1989, he was admitted to the Department of material science and technology of Lanzhou University and got his bachelor degree. In 1993, he joined Sichuan University as a master student for ions interacting with materials. During his study, he investigated the properties of composite MoS_2 thin films fabricated by the ion-beam-assisted-deposition (IBAD) method. After obtaining his master degree, he joined the Department of material science and technology in University of Electron Science and Technology. A project was started on the fabrication and characterization of a microwave phase shifter device. This device is very interesting for application in telecommunication. In 2001, he joined the surface science research group at Leiden University in the group led by Prof. Dr. Aart. W. Kleyn. During this time, time was spent on fabricating a new time of flight instrumentation for characterizing in-situ and real-time plasma-surface interactions. He also performed molecular dynamics simulations of low energy ion scattering and the dynamics of plasma-surface interactions.